Phonon engineering in thin tin films for tuning photon-nuclei interaction

Dissertation

zur Erlangung des Doktorgrades
an der Fakultät für Mathematik, Informatik und Naturwissenschaften
Fachbereich Physik
der Universität Hamburg

vorgelegt von

Sven Velten

Hamburg

2021

Gutachter der Dissertation:	Prof. Dr. Ralf Röhlsberger Prof. Dr. Michael Rübhausen
Zusammensetzung der Prüfungskommission:	Prof. Dr. Michael Potthoff Prof. Dr. Ralf Röhlsberger Prof. Dr. Michael Rübhausen PD Dr. Guido Meier Dr. Hans-Christian Wille
Vorsitzender der Prüfungskommission:	Prof. Dr. Michael Potthoff
Datum der Disputation:	29. November 2021
Vorsitzender Fach-Promotionsausschusses PHYSIK:	Prof. Dr. Wolfgang Hansen
Leiter des Fachbereichs PHYSIK:	Prof. Dr. Günter H. W. Sigl
Dekan der Fakultät MIN:	Prof. Dr. Heinrich Graener

Abstract

When materials are fabricated at the nanoscale, properties such as thermodynamic quantities can drastically deviate from bulk properties. Thereby, the embedding environment has a strong impact on the behavior of the nanostructured material and thus provides a handle to engineer the properties as desired. In this work, the vibrational behavior of embedded thin tin films is probed and engineered in order to tune the photon-nuclei interaction in nuclear resonance scattering.

The fabrication of tin films is typically affected by tin clustering. Here, they are prepared by combining magnetron sputter deposition with vacuum quenching resulting in β-Sn films with roughnesses of below one nanometer. By employing nuclear resonance scattering at the 23.88 keV resonance of ^{119}Sn, not only a deviating tin hyperfine structure is found at the interface to the embedding material, but also indications for a strong distortion of thermodynamic properties in the interface region. Thus, nuclear inelastic scattering is performed to access the phonon density of states of the tin films. A shift of the phonon modes to higher energy is measured reflecting an increase of the rigidness of the tin atoms. This results in an enhancement by up to a factor of eight of the Lamb-Mössbauer factor, a quantity describing the probability of an elastic nuclear resonant scattering process. In addition to tin films, also embedded thin films of stannic oxide are investigated for nuclear quantum optics. Embedded in magnesium oxide, the stannic oxide films exhibit a nearly ideal two-level quantum system independent of the layer thickness. Collective quantum optics effects such as the collective Lamb shift and superradiance are measured as a function of the tin dioxide layer thickness.

The obtained results pave the way for applying thin tin films to probe spin structures in paramagnetic materials and to extend nuclear quantum optics to the resonance energy of ^{119}Sn by employing stannic oxide films with their nearly unperturbed hyperfine structure.

Zusammenfassung

Wenn Materialien auf der Nanometerskala hergestellt werden, können Materialeigenschaften wie zum Beispiel thermodynamische Größen sich drastisch ändern. Dabei hat die einbettende Umgebung einen großen Einfluss auf das Verhalten des nanostrukturierten Materials und ist damit ein Stellhebel, um die Materialeigenschaften gezielt zu verändern. In dieser Arbeit wird das gezielte Ändern der Schwingungseigenschaften von eingebetteten Zinndünnfilmen untersucht, um die Photon-Kern Wechselwirkung in Kernresonanzstreuprozessen zu manipulieren.

Die Herstellung von Zinndünnfilmen ist typischerweise beeinträchtigt durch Bildung von Zinn-Clustern. Hier werden die Dünnfilme durch einen Magnetron Sputterprozess auf gekühlten Substraten hergestellt, was zu β-Sn Filmen mit Rauigkeiten von unter einem Nanometer führt. Durch die Anwendung von Kernresonanzstreuung an der 23.88 keV Resonanz von ^{119}Sn kann nicht nur eine Veränderung der Hyperfeinstruktur von Zinn an der Grenzfläche zum umgebenden Material festgestellt werden, sondern auch eine Verformung der thermodynamischen Eigenschaften in der Grenzflächenregion. Daher wird mittels unelastischer Kernstreuung die Phononenzustandsdichte in den Zinndünnfilmen vermessen. Die Messungen ergeben eine Verschiebung der Phononenzustände zu höheren Energien, was einer erhöhten Starrheit der Zinnatome entspricht. Dies resultiert in eine Erhöhung des Lamb-Mössbauer Faktors bis zum achtfachen, welcher die Wahrscheinlichkeit eines elastischen Kernstreuprozesses beschreibt. Zusätzlich zu den Zinndünnfilmen werden eingebettete Zinndioxidfilme für die Nutzung in der Kernquantenoptik untersucht. Wenn Zinndioxid eingebettet wird in Magnesiumoxid, weisen die Filme ein nahezu ideales Zwei-Level Quantensystem unabhängig von der Schichtdicke auf. Kollektive quantenoptische Effekte wie die kollektive Lamb Verschiebung und die Superradianz werden vermessen als Funktion der Schichtdicke.

Die Ergebnisse ebnen einen Weg um mittels Zinndünnfilmen Spinstrukturen in paramagnetischen Materialien auflösen zu können und um Kernquantenoptik mittels der nahezu ungestörten Hyperfeinstruktur von Zinndioxidfilmen durch die Resonanzenergie von ^{119}Sn erweitern zu können.

Contents

1. Introduction

Vibrational properties of metals are drastically modified on the nanoscale. The spatial confinement breaks the symmetries of the metallic crystal structures. This affects nearly all important material properties, such as the electrical, vibrational, optical and magnetic properties. Phonons, defined as quanta of the collective vibrational excitations in crystals, are especially affected by the crystal symmetry. Therefore, control over phonons is achieved by breaking the crystal symmetries on purpose, i.e. by nanostructuring the material. Since the confinement is on the nanometer scale, mainly phonons with short wavelengths, $\lambda \sim 10^{-9}\,\mathrm{m}$, are affected. Engineering of phonons aims to control the thermal properties, such as heat transfer. For example, nanostructures are designed to drastically reduce the thermal conductivity in thermoelectric materials [Bis12] or to transfer the heat along a designed pathway, so called heat waveguides [Mal13]. Although considerable progress has been made, the exact behavior of phonons in nanostructures is still poorly understood [Boz16].

Apart from technical applications of controlling the heat properties, phonons play an important role for X-ray scattering techniques. Due to thermal motions of the atoms, elastic X-ray scattering is attenuated in crystals. A special case occurs in nuclear resonant scattering where characteristic scattering times are longer than the lifetime of phonons. An X-ray pulse excites a nuclear resonance and the coherent decay is measured in a temporally resolved manner. The energies of nuclear resonances are typically in the order of a few keV, however the nuclear resonance linewidth is only about $10^{-6}\,\mathrm{eV}$ to $10^{-9}\,\mathrm{eV}$. Thus, the requirement of momentum conservation in the nuclear absorption process leads to a recoil energy which is much bigger than the resonance linewidth in the case of an unbound atom. In crystals, the recoil energy can be either absorbed by the whole crystal in an approximately recoilless process or by the excitation of atomic vibrations, i.e. phonons. Since only the recoilless process contributes to the elastically scattered signal, the increased likelihood of phonon excitations in soft materials lead to a strong

decrease of the coherent scattering intensity. The Lamb-Mössbauer factor quantifies the probability of recoilless absorption and therefore captures the thermodynamic material properties in the nuclear resonant scattering technique.

Most nuclear resonance scattering experiments are performed using the nuclear resonance at 14.41 keV of ^{57}Fe. Iron and most of its common intermetallic compounds have Lamb-Mössbauer factors of about 80%. Thus, even studies in nanostructures are feasible. For example, by embedding ultrathin layers of the resonant isotope inside a magnetic nanostructure, the internal magnetic spin structure can be unraveled [Röh02]. The same principle is applicable to resolve electric field gradients by measuring the interaction with the quadrupole moment of the nucleus, which was done with atomic resolution [PJ08]. Thin films in combination with nuclear resonant scattering also led to the emerging research field of hard X-ray quantum optics. The nuclear system with its extremely sharp resonance resembles a prototypical two-level quantum system. In thin films, the coupling strength of the nuclei with the X-rays can be tuned by the design of the layer system in which they are embedded [Röh10]. For example, thin film systems which act as a cavity for the X-rays render the measurement of the collective Lamb shift [Röh10], electromagnetically induced transparency [Röh10], subluminal X-ray propagation [Hee15] and Rabi oscillations between two nuclei ensembles [Hab17] possible.

For nuclear quantum optics, the nuclear system should resemble a two-level quantum state as close as possible. However, since metallic iron is ferromagnetic, the interaction of the magnetic moment of the nucleus with the magnetic field generated by the spin polarized electrons of the atomic shell leads to a level splitting of the nuclear hyperfine structure. Even if employing paramagnetic ultrathin iron films (thickness below one nanometer) or a paramagnetic compound such as stainless steel, a non-zero electric field gradient is often observed in thin films [Röh10; Sah11]. Thus, the interaction with the quadrupole moment of the nucleus leads to a splitting of the excited nuclear level. A thin film system with unsplit nuclear levels that can be considered as a perfect two-level system has yet to be found.

A promising candidate is tin with the 23.88 keV nuclear resonance of the isotope ^{119}Sn. Since tin in its metallic β-Sn form is paramagnetic, there is no net magnetic field at the nucleus. The presence of a weak electric field gradient results only in a hyperfine splitting of less than the resonance linewidth [Soa73]. Additionally, X-rays at the higher resonance energy are less affected by electronic scattering in the thin films which lead to higher

radiation intensities inside the film. Apart from applications for nuclear quantum optics, tin is more sensitive to probe magnetic nanostructures since the nuclear magnetic moment of ^{119}Sn is by a factor of ten bigger than the moment of ^{57}Fe [Rö04]. While the benefits of tin are obvious, the major disadvantage is the low Lamb-Mössbauer factor of only 0.04 in metallic tin. Therefore, nanostructure studies on tin can only be conducted at low temperatures, where the thermal vibrations are reduced [Hou17]. The low temperatures, however, are impractical for most nanostructure studies from an experimental point of view.

This work aims to probe and engineer the vibrational behavior of thin tin films in order to tune the coupling of the Mössbauer isotope ^{119}Sn with X-rays. Thereby, the Lamb-Mössbauer factor of embedded thin tin films was found to be strongly affected by the thermal properties of the embedding material. This paves a way to change the vibrational behavior of tin films in order to render nuclear resonant scattering of tin effectively. Thus, thin film studies are feasible for nuclear quantum optics at higher X-ray energies and for probing magnetic nanostructures, e.g. spin polarizations and spin currents in paramagnets. Not only tin films are investigated, but also tin dioxide films, since the nearly unsplit hyperfine structure in combination with a Lamb-Mössbauer factor of 59% is promising for the investigation of relatively thick films ($\sim 10\,\mathrm{nm}$) for nuclear quantum optics.

The work is structured as follows. In chapter 2 the theoretical background is laid out, where common properties of tin and the isotope ^{119}Sn are described, as well as general features of the hyperfine interactions, Mössbauer spectroscopy and nuclear resonant scattering in the elastic and inelastic regime. The following chapter 3 focuses on the experimental methods used to prepare, characterize and measure the thin films properties. The results are presented in three chapters. Chapter 4 focuses on the structural properties of the deposited tin films, such as smoothness, crystal phase and crystal growth. Also, the hyperfine structure of tin films is addressed with a special focus on the magnetic properties. In chapter 5, the dynamical behavior of thin tin films are investigated in terms of the film thickness and the embedding material. Tuning capabilities are discussed. Chapter 6 deals with the properties of tin dioxide films and the application to nuclear quantum optics experiments. The collective Lamb shift in tin dioxide films is measured. Finally, chapter 7 concludes with the results and an outlook is given on possible future experiments, which become possible based on the results presented in this work.

2. Theoretical background

Nuclear resonant scattering of synchrotron radiation is based on the Mössbauer effect. Therefore, many similarities between the theoretical descriptions of conventional Mössbauer spectroscopy and nuclear resonance scattering of synchrotron radiation can be found. However, while the first technique probes the energy dependent absorption of the Mössbauer isotope, the latter investigates the time-dependent scattering intensity of the Mössbauer resonance. With both techniques, the hyperfine structure of the nuclei can be revealed. Additionally, nuclear resonance absorption at synchrotrons can be applied to perform inelastic scattering, which gives access to the thermodynamical properties of Mössbauer isotopes inside a crystal lattice.

In the following, this chapter will provide a brief theoretical overview whereby the focus is set on the Mössbauer isotope ^{119}Sn and the element tin. In the first section, general properties of tin and its isotope ^{119}Sn are given. Especially the nuclear level structure of ^{119}Sn with the important Mössbauer resonance at 23.88 keV is described in more detail. Then, the origin of the nuclear hyperfine structure is sketched out. It is followed by a description of the Mössbauer effect and the Lamb-Mössbauer factor. Conventional Mössbauer spectroscopy is briefly explained. The ensuing section provides details about nuclear resonance scattering of synchrotron radiation. The section is divided into coherent and incoherent scattering processes. They describe the nuclear resonance scattering (NRS) and nuclear inelastic scattering (NIS) techniques at synchrotrons, respectively.

2.1. Properties of tin and its isotope ^{119}Sn

Tin (Sn) is an element of the group IV of the periodic table, which includes for example carbon and silicon as well. It has the atomic number 50, which is a magic number for the protons in the nucleus, meaning it is especially stable. Tin occurs therefore in a variety of stable isotopes with mass numbers ranging from 114 to 120, with 118.71 in its natural

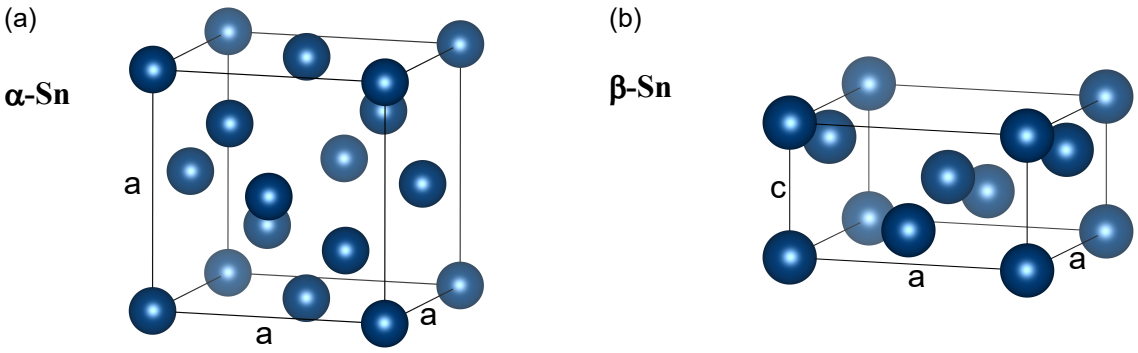

Figure 2.1.: (a) Cubic crystal lattice of α-Sn with $a = 6.4892(1)$ Å ([The54]) and (b) tetragonal crystal lattice of β-Sn with $a = 5.8308(2)$ Å and $c = 3.1810(2)$ Å ([Woł81]). For crystal visualizations, the software VESTA was used [Mom11].

composition. The electronic configuration of the valence electrons is $4d^{10}5s^25p^2$, whereby the exact occupation of the s and p orbital varies with the crystal structure.

One of the interesting physical properties of tin is its low melting point temperature of 231.93 °C, one of the lowest melting points of metals. Combined with its mechanical softness, tin is easy to work, and therefore it was historically an important metal. Pure tin exists in two allotropic crystalline modifications at atmospheric pressure, α-Sn (gray tin) and β-Sn (white tin) with a transition temperature of 13.2 °C. α-Sn is stable below the transition temperature, and has a diamond crystal structure, which is typical for group IV elements. It is shown in Fig. 2.1(a). The valence electrons are covalently bonded and it is non-conductive. With a band gap of 0.1 eV, α-Sn is a semiconductor with a diamagnetic behavior. On the opposite, β-Sn, the stable crystal phase at room temperature, has a tetragonal crystal structure, as shown in Fig. 2.1(b), where the valence electrons are delocalized over the crystal. It is a soft, paramagnetic metal.

Within the scope of this work, the oxide compounds of tin, namely SnO (stannous oxide) and SnO_2 (stannic oxide), play an important role. Stannic oxide is naturally formed and is a diamagnetic material with a white appearance in its amorphous powder form. Doped with other compounds, it becomes transparent and electrically conducting, which makes it valuable for optical devices, e.g. LCD technology. On the other hand, SnO is a black powder.

As previously discussed, tin has various stable isotopes. The most interesting for Mössbauer applications is ^{119}Sn, which has a natural abundance of 8.58%. The nuclear ground

state and the first excited state have total angular momenta of 1/2 and 3/2, respectively. They are separated by 23.8795(5) keV[1]. Both nuclear energy states have even parity. In these systems, the transition cannot be of electric dipole nature, since an electric dipole transition must involve a change of parity. Therefore, the nuclei can only couple via their magnetic dipole moment (M1) to the incident radiation or via their electrical quadrupole moment (E2). However, since the E2 contribution is smaller than 0.1% ([Boc68]), the ^{119}Sn nuclear resonance is treated as a pure M1 transition in the following. The excited state has a natural lifetime $\tau_0 = 26.0(1)$ ns, which corresponds to a natural linewidth Γ_0 of 25.3(1) neV via $\Gamma_0 = \hbar/\tau_0$ with $\hbar$ being the reduced Planck constant. With synchrotron radiation providing a high flux (7×10^4 photons/s/${\Gamma_0}^2$) of pulsed X-ray photons at the resonance energy and allowing time-resolved measurements up until 190 ns after excitation, the isotope is well suited for time-resolved nuclear resonant scattering experiments.

After excitation, the nucleus can undergo a non-radiative decay process, the internal conversion process, instead of a photon decay. In the internal conversion process, the energy is transmitted to an electron from the atomic shell, mostly to an *s*-electron since they have a non-zero probability to penetrate the nucleus and therefore can interact with the excited nuclear state. Subsequently, an electron is emitted due to the internal conversion process. The ratio of the emission of internal conversion electrons to a photon decay is given by the internal conversion factor α. For ^{119}Sn α is 5.22, which means after excitation the ratio of photon decay to internal conversion electrons is 1:5.22. Thus, the photon decay contributes only about $1/(1+\alpha) = 16\%$ to the total emission intensity. About 67%[3] of the internal conversion process leads to the emission of L-shell electrons at energies of about 19.8 keV. K-shell electrons cannot be emitted since their binding energy of 29.2 keV is higher than the nuclear resonance energy. The subsequent L-shell vacancy results in the emission of 3 keV Auger electrons ($\approx 93\%$ probability[4]) or L_α/L_β X-rays ($\approx 7\%$) at about 3.5 keV.

The next higher excited state of ^{119}Sn is the 11/2-state with an excitation energy of 89.53(1) keV. It decays solely into the 3/2-state with a natural lifetime of 423(1) days. The

[1] Transition energies, natural lifetimes and conversion factors are taken from the database provided by the Mössbauer Effect Data Center, [MED], and, if missing, by the Nuclear Data Service, [NDS].

[2] Flux and pulse separation are taken exemplary from beamline P01 at *PETRA III* in the timing mode

[3] The probability is given by $\alpha_L/(1+\alpha)$, describing how many L-shell electrons, α_L, are emitted due to internal conversion in relation to one photon decay and α internal conversion electrons. Here $\alpha_L = 4.09$ and $\alpha = 5.06$, both taken from the same source, [NDS]

[4] An estimated fluorescence yield of 0.07 was used ([CXR]).

decay is dominated by the internal conversion process with $\alpha = 5000$. This metastable state is also called ^{119m}Sn, and is important for conventional Mössbauer spectroscopy, since it is the radiation source in those experiments.

2.2. Probing the nuclear hyperfine structure

The nuclear transition energies can be shifted or split into multiple transitions due to electromagnetic interactions with the environment of the nucleus. The changes are in the sub-μeV scale, thus relatively small if compared to the transition energies which are in the order of keV. The exact level structure of the nucleus, resulting from the interaction with its environment, is called hyperfine structure. By detecting the nuclear hyperfine structure, it is possible to draw conclusions about the electronic and magnetic state of the nucleus and its environment. The exceptional small linewidth Γ_0 of a few neV of most of the nuclear transitions makes this detection possible.

Two major interactions are important: The electrostatic interaction of the atomic electron density with the electric quadrupole moment of the nucleus and the magnetostatic interaction of the nuclear magnetic moment with an external or internal magnetic field. The contributions and experimental techniques to probe them are explained in the following.

2.2.1. Hyperfine structure of the nucleus

The interaction, which governs the hyperfine structure, is of electromagnetic nature. The Hamiltonian of the system $\mathcal{H}$ is described by a electrostatic part $\mathcal{H}_{es}$ and a magnetostatic part $\mathcal{H}_{ms}$. Both can be expressed with a multipole expansion indexed by the order l by

$$\mathcal{H} = \mathcal{H}_{es} + \mathcal{H}_{ms} \tag{2.1}$$

$$= \sum_l \mathcal{H}_{es}^{(l)} + \sum_l \mathcal{H}_{ms}^{(l)} \tag{2.2}$$

$$= \frac{1}{4\pi\epsilon_0} \sum_l \sum_{m=-l}^{l} (-1)^m E_{-m}^{(l)} Q_m^{(l)} + \frac{\mu_0}{4\pi} \sum_i \sum_l \sum_{m=-l}^{l} (-1)^m B_{-m,i}^{(l)} M_{m,i}^{(l)}, \tag{2.3}$$

whereby ϵ_0 and μ_0 are the vacuum permittivity and permeability and i describes the spacial components x, y and z. $E^{(l)}$ and $B^{(l)}$ are tensor operators describing the electric

and magnetic fields generated by the electronic system at the site of the nucleus. The quantities $Q^{(l)}$ and $M^{(l)}$ are the operators of the electric and magnetic multipole moments of the nucleus. Since the nucleus has a well defined parity, inversion symmetry reasons can be used to exclude multipole moments with an odd parity from the Hamiltonian. Consequently, all electric (magnetic) multipole moments with an odd (even) order l must be zero. For example, this includes the electric dipole moment and the magnetic quadrupole moment. Therefore, the leading terms of the Hamiltonian, besides an electrostatic monopole term, which only gives a constant global energy shift, are the electrostatic quadrupole and the magnetostatic dipole interaction. The evaluation of the quadrupole term $\mathcal{H}_{es}^{(2)}$ leads to a contribution $\mathcal{H}_0^{(2)}$, which results in a measurable energy shift between nuclei in different chemical environments, the so called isomer shift. With this term explicitly written out, $\mathcal{H}_{es}^{(2)} = \mathcal{H}_0^{(2)} + \mathcal{H}_{qs}^{(2)}$, and neglecting all orders $l > 2$, the Hamiltonian now reads

$$\mathcal{H} = \mathcal{H}_0^{(2)} + \mathcal{H}_{qs}^{(2)} + \mathcal{H}_{ms}^{(1)}. \tag{2.4}$$

A brief description of each contribution is provided in the following.

Isomer shift

The isomer shift appears in the electrostatic quadrupole interaction term since the nucleus cannot be described by a point charge but as a spatially extended charge density. It eventually leads to a shift of the transition energy as shown in Fig. 2.2(a) of about 10^1 – 10^2 neV.

Since s-electrons have a finite probability to be at the position of the nucleus, the electrostatic coupling energy slightly changes when the spatially extended charge distribution of the nucleus is considered. The energy contribution is given by [Wer64]

$$E_0^{(2)} = \frac{2\pi}{5} Z e^2 \left|\psi_e(r=0)\right|^2 R^2, \tag{2.5}$$

where Z is the atomic number, $\psi_e(r)$ the electronic wave function in space representation and R the nucleus radius. Since the energy shift originates from the quadrupole interaction, the R^2 appears. When the nucleus is excited to a higher energy state, the charge distribution of the nucleus changes and thus its radius. Therefore, the transition energy

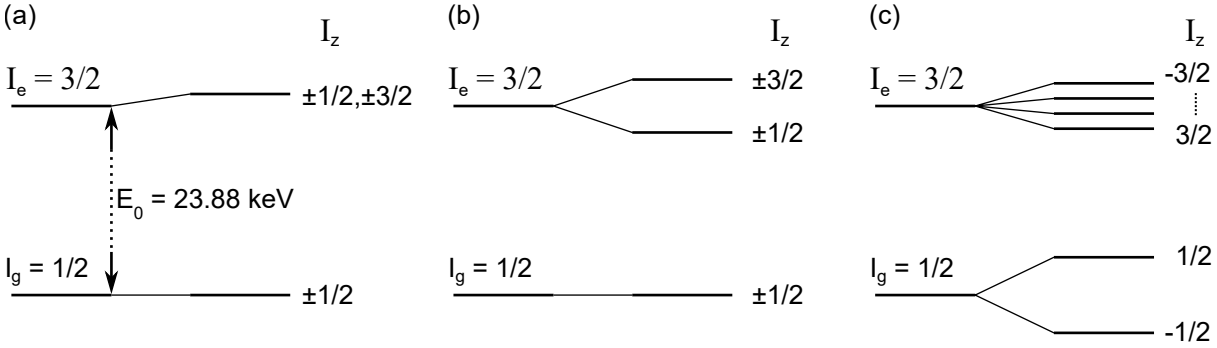

Figure 2.2.: Exemplary hyperfine structure for ^{119}Sn for three cases. (a) When no electric field gradient or magnetic hyperfine field is present, the transition E_0 is shifted by the constant $E_0^{(2)}$, which depends on the chemical state of the material. (b) In the presence of an electric field gradient, quadrupole interaction leads to a splitting of the excited state into two states in respect to I_z^2. (c) If a magnetic hyperfine field is present but no electric field gradient, the energy states are split into six states in respect to I_z.

is shifted by the energy shift ΔE_0

$$\Delta E_0 = E_{0,e}^{(2)} - E_{0,g}^{(2)} = \frac{2\pi}{5} Z e^2 \left|\psi_e(r=0)\right|^2 (R_{ex}^2 - R_g^2), \tag{2.6}$$

whereby the indices "e" and "g" label the excited and ground state. With $R_e^2 - R_g^2 = 2R(R_e - R_g)$ and the mean radius $R = \frac{R_e + R_g}{2}$, one gets

$$\Delta E_0 = \frac{4\pi}{5} Z e^2 R^2 \left|\psi_e(r=0)\right|^2 \left(\frac{\delta R}{R}\right), \tag{2.7}$$

with $\delta R = R_e - R_g$. For example, Mössbauer experiments showed that the nuclear radius of the 3/2-state of ^{119}Sn is $1{+}3.3 \times 10^{-4}$ larger than its ground state [Boc66].

Crucially, equation 2.7 shows that the energy shift depends also on the electronic state described by ψ_e, which means, that the shift is affected by its chemical environment. If two nuclei are present in different chemical environments, e.g. ^{119}SnO and ^{119}SnO$_2$ there is a difference between the energy shifts, $\Delta E_0(^{119}\mathrm{SnO}) - \Delta E_0(^{119}\mathrm{SnO_2})$. This difference is called the isomer shift. It is an important quantity to measure, since it can be used to identify the chemical state of a material.

Quadrupole interaction

The quadrupole interaction describes the interaction of the quadrupole moment of the nucleus Q with an electric field gradient at the position of the sample, $V_{ij} = -\partial_i E_j$, with E being the electric field at the nucleus and (i, j) describing spatial coordinates. Only nuclear states with a spin $> 1/2$ have a quadrupole moment. Thus, for ^{119}Sn, only the excited states with $I = 3/2$ can interact with the electric field gradient.

Analytical solutions of the eigenvalue problem for the nuclear Hamiltonian with quadrupole interaction and magnetic interaction exist only for a few special cases [Rö04]. A discussion about general solutions of this system is provided in [Mat62]. A simple analytical solution is found in the case of pure quadrupole interaction with an electric field gradient exhibiting axial symmetry. In this case, the electric field gradient can be described by a single quantity, V_{zz}, when the system coordinates are transformed into the electric field gradient system. A spin 3/2-state is shifted by [Rö04]

$$\Delta E_{qs} = \frac{eV_{zz}Q}{4}\left(I_z^2 - \frac{5}{4}\right), \tag{2.8}$$

in this scenario with I_z being the z-component of the nuclear spin I. The state is therefore split into two states with $I_z^2 = (\pm 1/2)^2$ and $I_z^2 = (\pm 3/2)^2$. A transition between a spin 1/2-state and a 3/2-state, as for ^{119}Sn, is therefore split into two possible transitions, as shown in Fig. 2.2(b). For ^{119}Sn with an exemplary total splitting of $eV_{zz}Q/2 = 50\,\text{neV}$ and an assumed quadrupole moment of 0.09 barn of the excited 3/2 ^{119}Sn state ([MED]), the magnitude of the electric field gradient is about $5 \times 10^{21}\,\text{V/m}^2$. Atomic electrical fields are extremely strong, which renders a tuning of the direction or strength of the electric field gradient impossible in an experiment. Thus, only the total quadrupole splitting is experimentally accessible if the quadrupole moment of the energy state is unknown.

For non-axial systems, the magnitude of the energy shift is altered, commonly parameterized by an asymmetry factor η. The splitting into two states, however, remains unchanged.

The electric field gradient is typically generated by crystal distortions, for example due to Jahn-Teller distortions in single crystals [Nak15], but also due to lattice mismatches at interfaces or crystal defects. In this work, films with thicknesses of less than 20 nm are investigated. These systems are often formed by nanometer small crystallites. Because

of a high amount of interfaces and grain boundaries, as well as imperfect crystal lattices, electric field gradients can be expected in such thin films, even though an absence is predicted for the bulk material. This is the case, for example, in stainless steel thin films, where no quadrupole interaction occurs in the bulk material, however, in nanometer thick films, a quadrupole splitting was measured [Sah11].

In thin films, the orientation of the electric field gradient is mostly not defined, since the orientation of the crystallites is random. In the case of single atomic layers, however, which are epitaxially grown on a specific substrate, a directed orientation of the field gradient was found ([PJ08]).

Magnetic dipole interaction

If an external magnetic field is present or the atomic electron system generates a magnetic field at the nucleus, the nucleus interacts with the field due to its magnetic moment μ_n. If no electrical quadrupole interaction is present, and the quantization direction of the nuclear spin I is parallel to the magnetic field direction, the magnetic dipole interaction leads to an energy shift ΔE_{md} of the nuclear energy state defined by the spin I and its z-component I_z. The energy shift is given by [Rö04]

$$\Delta E_{md} = -I_z \mu_n B_{hf} / I, \tag{2.9}$$

with the magnetic hyperfine field B_{hf}, which is a summation of all internal and external fields. Subsequently, nuclear levels are split in respect to I_z. For example for ^{119}Sn, the ground state is split into two states with $I_z = \pm 1/2$ and the excited state into four states with $I_z = \pm 3/2, \pm 1/2$ as shown in Fig. 2.2(c). Since the magnetic moments of the ground state and excited state of ^{119}Sn have opposite signs, the splitting order in respect to I_z is reversed.

The magnetic hyperfine field can be generated by internal or external sources. Internal fields are produced by the electron spin or the orbital moments of not completely filled atomic shells, or by spin-polarized s-electrons, which have a finite probability density of being inside the nucleus. The latter contribution dominates in magnetic materials and is called Fermi contact interaction. It can lead to strong magnetic fields at the nucleus. In Fe, for example, it generates a magnetic hyperfine field of about 33 T. The s-electrons are polarized by an intra-atomic interaction with the spin-polarized valence d-electrons.

Not only for magnetic materials, the Fermi contact interaction is important, but also for paramagnets, where an external magnetic field leads to a magnetization of the material. The subsequent polarization of inner s-electrons leads to a magnetic field at the position of the nucleus in addition to the external field. The energy shift of the nuclear levels due to the additional magnetic field is called Knight shift. A comprehensive review about magnetic hyperfine field contributions can be found, e.g. in [Fre65] or [Por65].

2.2.2. Conventional Mössbauer spectroscopy

Mössbauer spectroscopy aims to probe the hyperfine structure of materials containing isotopes with suitable nuclear resonances. The technique is based on re-absorption of γ-rays emitted from a radioactive isotope. For example, the eventual γ-decay of the metastable state ^{119m}Sn leads to the emission of a 23.88 keV photon, which subsequently can be absorbed by another ^{119}Sn nucleus. This principle, however, should be forbidden for nuclear transitions. Due to the extreme narrow linewidth of the nuclear resonances in the neV-regime, momentum and energy conservation of the photon emission and absorption process play an important role. For a photon emission/absorption process, an unbound nucleus has to absorb a recoil energy E_R of

$$E_R = \frac{E_0^2}{2m_n c^2}, \tag{2.10}$$

with E_0 the transition energy, m_n the nuclear mass and c the speed of light. For ^{119}Sn, for example, the recoil energy is about 2.6 meV, which is much bigger than the natural linewidth ($\Gamma_o = 25$ neV) and any hyperfine splitting (about $10^1 - 10^2$ neV). The subsequent Doppler shift of the moving nucleus leads to a significant red-shift of the emitted photon. Therefore, the emission and re-absorption is not possible for an unbound nucleus.

If the nucleus is bound, however, for example in a crystal, the situation changes. In crystals, the recoil energy is transported by collective vibrations, i.e. phonons. Based on the theory developed by Lamb for resonant absorption of slow neutrons [LJ39], Rudolf Mössbauer proved theoretically and experimentally that there is a non-zero probability that no phonon is excited when the photon is emitted or absorbed [Mös58]. Instead, the whole crystal absorbs the recoil energy and the emitting/absorbing nucleus experiences no Doppler shift. This zero-phonon probability factor is called Lamb-Mössbauer factor

or recoilless fraction. Multiple subsequent theoretical work, e.g. conducted by [Sin60] and [Lip60], showed, that the Lamb-Mössbauer factor is given by the ratio of elastically to inelastically scattered photons in the *incoherent* scattering intensity. Additionally, the resonant photon absorption cross section is proportional to this recoilless fraction. With the knowledge of the phonon density of states $g(E)$ of the crystal, the Lamb-Mössbauer factor f_{LM} can be calculated by [Sin60]

$$f_{LM} = \exp\left(-2E_R \int_0^\infty \frac{g(E)}{E}\left(\frac{1}{2} + \langle n(E,T)\rangle\right) dE\right). \tag{2.11}$$

The average occupation number $\langle n(E,T)\rangle$ of the energy state E at temperature T is given by the Bose-Einstein statistic due to the bosonic character of phonons with $\langle n(E,T)\rangle = 1/(\exp(\beta E)-1)$, where $\beta = 1/(k_B T)$ with the Boltzmann constant $k_B = 1.381 \times 10^{-23}\,\mathrm{J/K}$. Missing in the equation 2.11 is the momentum transfer of the scattering event due to the incoherent nature. This is the major difference to the Debye-Waller factor known from typical X-ray scattering experiments.

Equation 2.11 shows that the Lamb-Mössbauer factor depends on the recoil energy E_R and consequently on the transition energy E_0. Therefore, for increasing transition energies, the Lamb-Mössbauer factor decreases, and Mössbauer experiments becoming less effective. Moreover, equation 2.11 relates the Lamb-Mössbauer factor with crystal properties. With setting the temperature to zero kelvin, thus $\langle n(E,T)\rangle \simeq 0$, the exponential is equal to $-2E_R/(\hbar\omega_{av})$ with an average vibrational energy of the crystal $\hbar\omega_{av}$, which is given by $1/\hbar\omega_{av} = \int dE\, g(E)/E$ ([Lip60]). Soft materials with a low average vibrational energy have therefore a small Lamb-Mössbauer factor. For example, ^{119}Sn nuclei in the soft β-Sn crystal phase have a recoilless fraction of about 0.04. However, in the oxide compound $^{119}SnO_2$, where atoms are stronger bound in the crystal, the Lamb-Mössbauer factor is about 0.6. This comparison points out that the Lamb-Mössbauer factor is not only determined by the nuclear isotope, but also by the crystal properties of the material. Additionally, the assumption, which was implicitly taken in the discussion above, of an isotropic Lamb-Mössbauer factor is only valid for a cubic crystal. In general, the recoilless fraction depends on the crystal direction, and thus, is anisotropic. For example, in a single crystal of β-Sn, which has a tetragonal crystal lattice, the Lamb-Mössbauer factors differs along its two major crystal directions by a factor of ≈ 1.5 at room temperature [Sha64]. In polycrystalline materials, the Lamb-Mössbauer factor is averaged over all pos-

Table 2.1.: Isomer shift (relative to SnO_2), quadrupole splitting ($= eQV_{zz}/2$) and Lamb-Mössbauer factor at room temperature of typical tin crystal phases and tin oxide compounds. For energy conversion: $1\,\mathrm{mm/s} \mathrel{\widehat{=}} 79.6\,\mathrm{neV}$.

Material	Isomer shift (mm/s)	Quadrupole splitting (mm/s)	Lamb-Mössbauer factor
SnO_2	0.0	0.57[Sva97]	0.63[Stu99a]
α-Sn	2.02[Sva97]	0.0[Sva97]	0.16[Cue01]
β-Sn	2.54[Sva97]	0.23[Soa73]	0.04[Bar00]
SnO	2.64[Sva97]	1.33[Sva97]	0.32[Stu99a]

sible directions. The (average) Lamb-Mössbauer factor at room temperature of common tin crystal phases and tin oxide compounds are given in Tab. 2.1.

In Mössbauer spectroscopy, a radioactive source provides the γ radiation, which is used to excite the corresponding nuclei in a target material. Both, target and source, must have a significant high recoilless fraction in order to record a measurement. By moving the source, or target, the energy detuning between both of them can be adjusted. the Doppler velocity v corresponds to an energy detuning ΔE via the relation,

$$\frac{\Delta E}{E_0} = \frac{v}{c}. \tag{2.12}$$

The natural linewidth of the ^{119}Sn transition, $\Gamma_0 = 25.3\,\mathrm{neV}$, is equivalent to a Doppler shift of $0.318\,\mathrm{mm/s}$. In a typical Mössbauer experiment, the transmission of the γ radiation is measured while tuning the source velocity, e.g. by $\pm 5\,\mathrm{mm/s}$. Thus, the energetically detuned γ-rays probe the absorption spectrum, i.e. the hyperfine structure, of the target material. The resolution is given by the resonance linewidth of the source, which for an ideal source is equal to the natural linewidth of the nuclear transition. An example for ^{119}Sn is given in Fig. 2.3. The simulated transmission intensity of a $1\,\mu\mathrm{m}$ β-Sn foil enriched in the isotope ^{119}Sn is depicted as a function of the Doppler drive velocity or accordingly of the corresponding energy detuning. Three cases are shown. In Fig. 2.3(a), the target material has an isomer shift of $1\,\mathrm{mm/s}$ ($\approx 80\,\mathrm{neV}$) relative to the source. This means, the chemical states differ of the source and target. In Fig. 2.3(b), the hyperfine structure of the target material exhibits a quadrupole splitting. As discussed in the previous section, the presence of an electric field gradient leads to a splitting of the hyperfine structure and thus to two possible nuclear transitions, see Fig. 2.2(b). Therefore, the

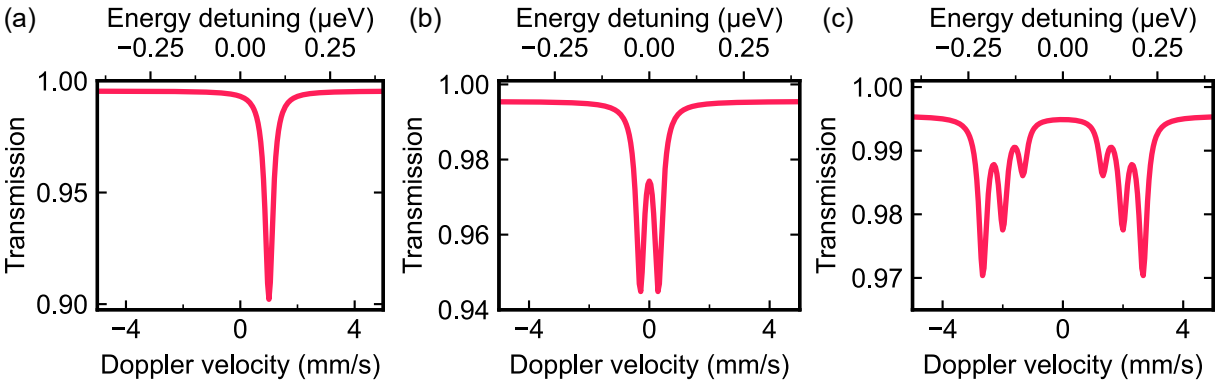

Figure 2.3.: Simulated transmission intensity of a Mössbauer spectroscopy experiment on a 1 µm β-^{119}Sn foil. The energy of the emitted photons from the source are detuned by a Doppler drive over a range of ±5 mm/s. The detuning in µeV is given by the upper x axis. Three cases are presented: (a) An isomer shift relative to the source by 1 mm/s (≈ 80 neV), (b) a pure quadrupole splitting of 0.6 mm/s (≈ 50 neV) and (c) a pure magnetic splitting with a magnetic hyperfine field of 4 T.

Mössbauer transmission spectrum has two dips. In the last case, shown in Fig. 2.3(c), a magnetic hyperfine field of 4 T is present. In a magnetic field, the nuclear ground state is split into two states and the excited state into four states, see Fig. 2.2(c). In theory, there should be eight possible transitions. However, since this is a magnetic dipole transition, the dipole transition rules apply which means that the z-component of the nuclear spin can only change by $M = \pm 1, 0$. Thus only six possible dipole transitions are allowed. Therefore, the transmission spectrum has six dips in Fig. 2.3(c). The dipole transition rules also lead to a varying weight of the six transition intensities. It depends on the orientation of the magnetic hyperfine field and the polarization of the incoming γ-rays [Rö04]. The relative weight of the transmission dips therefore reveals the orientation of the magnetic hyperfine field, if the incoming γ-rays are polarized. Also for unpolarized γ-rays a differentiation is possible between a magnetic field which is oriented parallel to the wave vector of the γ-rays and a field oriented perpendicular to the wavevector. The spectrum shown in Fig. 2.3(c) is calculated for unpolarized γ-rays and a random magnetization orientation.

In Mössbauer spectroscopy, the aim is to determine the hyperfine structure of the target material and thus reveal the chemical and magnetic states of the material. Parameters for common tin crystal phases and tin oxide compounds are given in Tab. 2.1.

Conventional Mössbauer transmission experiments are only of limited use for materials with a low amount of resonant material, e.g. for thin films, since the signal-to-background ratio is too low. In these cases, conversion electron Mössbauer spectroscopy (CEMS) is often employed. In this setup, the electrons generated from internal conversion after the γ-ray excitation are counted. The direct recording of nuclear decay products means that the resulting electron emission spectrum has a much lower background noise in comparison to conventional transmission measurements. This technique has a high surface sensitivity, since the electrons first need to escape the material and their mean free path is only a few nanometer long. Mössbauer studies on thin films are therefore often done with a CEMS setup.

2.2.3. Nuclear resonance scattering

Conventional Mössbauer spectroscopy focuses mainly on the resonant absorption of nuclear transitions with energy resolving methods. It is an incoherent measurement technique since the radioactive source provides only incoherent radiation. At synchrotron facilities, however, the coherent nature of resonant scattering processes is employed. Here, intense and highly polarized X-ray pulses are provided with a pulse duration below 1 ns. Thus, the temporal decay after the X-ray pulse excited the nuclei can be directly measured. The energetically broad X-ray pulse and the coherent nature of the nuclear excitation then lead to an interference pattern in the time domain, visible by a beat pattern in the temporal decay intensity. Since synchrotron X-ray pulses are also highly focused, nanostructured materials, such as thin films, can be measured within hours or even minutes. This leads to drastically reduced measurement times in comparison to conventional CEMS studies. Here, typical measurement times are days. In the following, a brief theoretical overview of the coherent nuclear excitation and its role in nuclear resonance scattering experiments is given.

The complex scattering amplitude in the energy domain $f(E)$ for a single bound nucleus, which is assumed to exhibit no hyperfine splittings, is given by a Lorentzian line shape [Smi99]

$$f(E) = \frac{k_0}{4\pi}\sigma_0 f_{LM}\frac{\Gamma_0/2}{E - E_0 - i\Gamma_0/2}, \tag{2.13}$$

with k_0 the wave vector at the resonance energy, the Lamb-Mössbauer factor f_{LM}, E_0 is

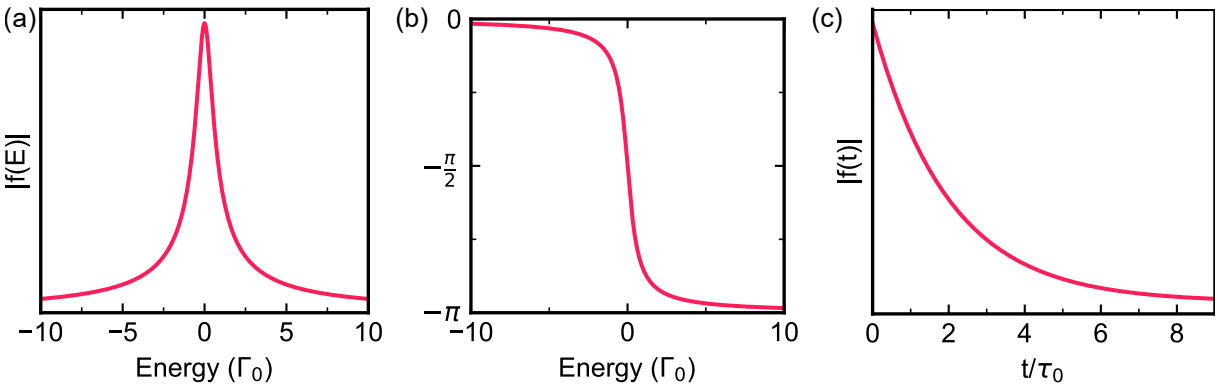

Figure 2.4.: The complex scattering amplitude of a single nucleus without hyperfine splittings is depicted by its absolute value (a) and its complex phase (b) in the energy domain, as well as its absolute value in the time domain (c). The energy is given in units of the natural linewidth Γ_0 around the resonant energy, $E - E_0$, and the time is normalized by the natural lifetime τ_0 of the nucleus.

the resonance energy and Γ_0 the natural linewidth. The maximal resonant cross-section σ_0 contains nuclei-specific parameters: The spin of the excited state I_e and ground state I_g and the internal conversion factor α. It is defined by

$$\sigma_0 = \frac{2\pi}{k_0^2} \frac{1}{1+\alpha} \frac{2I_e+1}{2I_g+1}. \tag{2.14}$$

To give an example, the resonant nuclear cross-section for ^{119}Sn is 1379.6 kbarn, which is more than 500 times bigger than the cross section for electronic scattering. The absolute value and the complex phase of the scattering factor are shown in Fig. 2.4(a) and (b), respectively. The phase of the incident X-ray wave package gets shifted by $-180°$ around the resonance, with the spectral component at the exact resonance experiences a phase shift of $-90°$. The weight variation of the spectral components around the resonance leads to a dephasing of the scattered intensity with time [Smi99]. This corresponds to the lifetime $\tau_0 = \hbar/\Gamma_0$ of the excited state. A broader resonance means a faster dephasing and thus a smaller lifetime. In Fig. 2.4(c) the absolute value of the scattering amplitude in the time domain is shown. The intensity follows an exponential decay $\propto \exp(-t/\tau_0)$.

In an ensemble of nuclei, the coherent character of the scattering becomes important. This is the case, when the ground state of the nuclear ensemble after the scattering process is unchanged. Changes, which lead to incoherent scattering, are, for example, excitations

of phonons, meaning a recoil process, rearrangement of the electronic shell due to internal conversion or a spin-flip in the ground state, e.g. from a previous $I_z = +1/2$ state to a $I_z = -1/2$ state [Rö04]. If no change of the ground state occurs, the nuclei within the ensemble are indistinguishable. Therefore, in the quantum mechanical picture, the single photon creates a *delocalized* intermediate excited state shared by several nuclei [Smi99]. This state is also named nuclear exciton. It can be interpreted as a coherent superposition of an excited state over all nuclei. The coherent state $|\psi_c\rangle$ is proportional to [Han89]

$$|\psi_c\rangle \propto \sum_a^N e^{i\vec{q}\vec{r}_a} |e_a\rangle |G_0(a)\rangle , \tag{2.15}$$

where q is the momentum transfer of the scattering event. Thus, the coherent state is a sum over N possibly excited nuclei: The excitation of nucleus a at position $\vec{r}_a$ from its ground state $|g_a\rangle$ to the state $|e_a\rangle$ is weighted by the spatial phase factor $\exp(i\vec{q}\vec{r}_a)$. $|G_0(a)\rangle$ describes all other nuclei, which are in their ground state $|G_0(a)\rangle = \prod_{a' \neq a} |g_{a'}\rangle$.

The spatial phase factor leads to diffraction properties. For example, if the nuclei are ordered, nuclear Bragg reflections occur. In the case of randomly placed nuclei, the sum over the spatial phase factor only provides a non-zero contribution in the forward direction, $\vec{q} = 0$. Therefore, in nuclear resonance experiments, the temporal decay is often recorded in a transmission setup, i.e. in the forward direction, for example if thin foils are measured. In layered materials, where reflections occur at each interface, two coherent channels are possible if the incident angle is much smaller than one, i.e. $\vec{q} \simeq 0$: transmission and reflection. Thin films are mostly measured under a grazing incidence angle, since it enhances the effective X-ray path through the material. The resonantly scattered intensity is then measured in the reflection channel.

In the case of the transmission through thin foils, whereby the thickness is characterized by the unit-less effective thickness, $T_{\text{eff}} = \sigma_0 f_{LM} \beta \rho_n d$ with β the isotope abundance of the resonant nucleus, ρ_n the number density and d the thickness of the resonant material, the delocalized excitation can be described by a macroscopic dipole moment [Smi99], radiating proportional to the number of nuclei N. Thus, the radiation intensity is proportional to N^2. In Fig. 2.5(a), the time integrated emitted intensity of the decaying nuclei in forward direction is shown as a function of the effective thickness. The double logarithmic plot shows the quadratic dependence for thin foils. For thicker foils, $T_{\text{eff}} \approx 1$, this changes into a linear relation. For very thick foils, $T_{\text{eff}} > 10$, the electronic absorption starts to

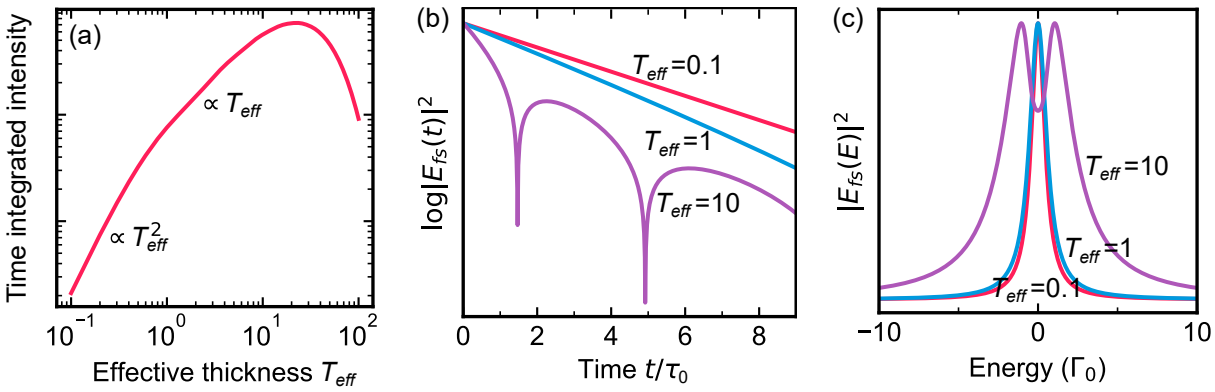

Figure 2.5.: (a) The time integrated intensity of the forward scattering signal is shown as a function of the effective thickness in a double logarithmic plot. In time domain (b), the forward scattering intensity is shown as a function of time over natural lifetime τ_0 for different effective thicknesses. In comparison, the intensity in the energy domain (c) is plotted versus the energy relative to the transition energy E_0 in units of the natural linewidth Γ_0. In (b) and (c) the intensities are normalized to their maximum values for a better comparison.

dominate and the intensity eventually decreases.

Due to energy conservation, the emission of N nuclei must be N-times shorter. Thus, the temporal decay is accelerated, the so called superradiant decay [Gro82]. The temporal evolution of the electric field intensity in the forward scattering direction, $\left|E_{fs}(t)\right|^2$, is shown in Fig. 2.5(b) for different effective thicknesses. For $T_{\text{eff}} = 0.1$ (red), the decay shows the same exponential decay as a single nucleus. This changes for an effective thickness of $T_{\text{eff}} = 1$ (blue) and even more for a thick layer with $T_{\text{eff}} = 10$ (violet). Besides a faster decay, the latter example shows an additional beat feature in the decay. While for $T_{\text{eff}} = 0.1$ the forward scattering signal can be described by a scattering event with a single nucleus, the decays for $T_{\text{eff}} = 1$ and especially for $T_{\text{eff}} = 10$ are impacted by the coherence nature of the nuclear exciton. In thicker foils, an excitation of nuclei at one point of the foil impacts the excitation probability of nuclei further along in the beam path. Thus, the nuclei along the beam path experience different radiation fields. An interplay between the nuclei ensemble and the radiation field inside the layer arises [Smi99]. It corresponds to multiple scattering of the photons with the resonant material. This interplay is visible as an aperiodic modulation of the temporal decay pattern, and is called dynamical beat. In Fig. 2.5, the dynamical beat is visible for the foil with $T_{\text{eff}} = 10$. The variation of the

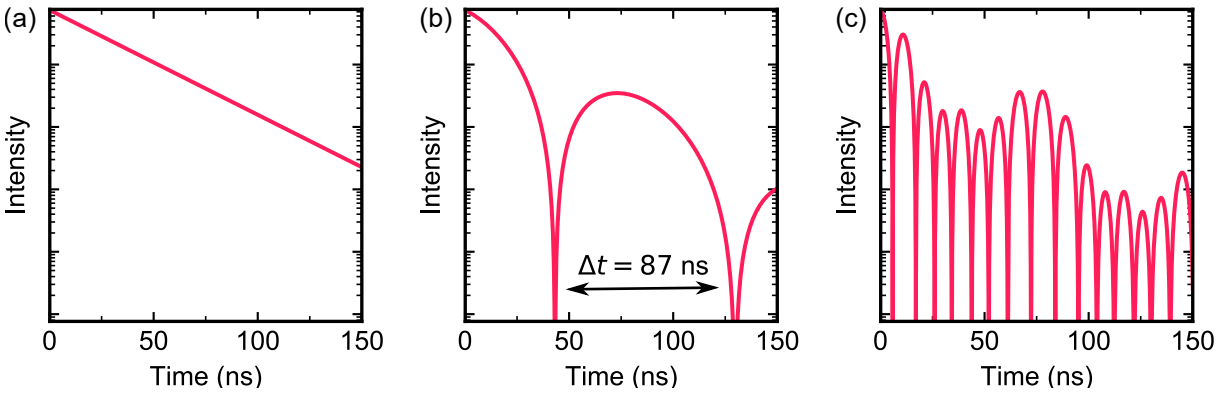

Figure 2.6.: Exemplary temporal decay pattern for ^{119}Sn for three cases: (a) no splitting, (b) a quadrupole splitting of 0.6 mm/s, which is equal to a beat period of about 87 ns, and (c) a magnetic splitting in a 4 T field. For both, (b) and (c), random orientation of the respective field was assumed.

excitation probability along the beam path is also reflected in the energy spectrum of the scattered electric field in forward direction, $E_{fs}(E)$. In Fig. 2.5(c), the intensity is shown as a function of energy in units of the natural linewidth, Γ_0, relative to the resonance energy, $E - E_0$. While the resonance linewidth for the foil with $T_{\text{eff}} = 0.1$ is equal to one Γ_0, the resonance of foil with $T_{\text{eff}} = 1$ is slightly broadened, which corresponds to the speed-up effect in the time domain. For the thick foil with $T_{\text{eff}} = 10$, however, a double peak feature emerges. The coherent excitation of different nuclei along the beam path leads to an eventual deconstructive interference at exact resonance, and thus to a dip at $E = E_0$ in the energy spectrum of the electric field in forward direction [Smi99].

The dynamical beat also appears in thin films in a grazing incidence setup. Here, the effective X-ray path through the material can be tuned via the internal reflections in the layered structure, and thus in some cases, the same dynamical effect can appear. The example of the dynamical beat shows that by tuning the material structure, e.g. the thickness in foils or the layer alignment in layered structures, the interaction between photons and nuclei can be tuned. This is an important tool in the field of nuclear quantum optics [Röh10].

So far, each nucleus is characterized by a single resonance without any hyperfine splittings. However, if an electric field gradient and/or a magnetic hyperfine field are present, the ground and excited state of each nucleus can be split. This means, that in Eq. 2.15 an additional sum is required which accounts for all possible ground and excited states of

nucleus a. Thus, the hyperfine structure is part of the coherent summation over all nuclei and therefore leads to additional interference patterns in the time domain. Three exemplary temporal decays at the resonance energy of ^{119}Sn are shown in Fig. 2.6 to illustrate the interference effects of quadrupole and magnetic splittings. The calculation was done for thin foils so that no dynamical effects occur. In the simplest case where no electric field gradient or magnetic hyperfine field is present, the temporal decay is exponential, see Fig. 2.6(a). The chemical state of the foil can therefore not be measured, in contrast to the always present isomer shift between source and target in Mössbauer spectroscopy. Only if two types of chemical states are present in the foil, for example, if the material is partially oxidized, the two energetically shifted transitions are visible by an interference beat in the time domain corresponding to the isomer shift between both chemical states. If an electric field gradient is present, the excited states is split and two transitions are possible. This quadrupole splitting is shown in Fig. 2.6(b) with a simulated splitting of the energy levels of 0.6 mm/s The two transition frequencies lead to a beat pattern in the temporal decay. The period of the beat is given by $T_{qs} = 2\pi\hbar/E_{qs} = 2\pi\hbar/(\Delta E_{qs,2} - \Delta E_{qs,1})$, where $\Delta E_{qs,1}$ and $\Delta E_{qs,2}$ are given by Eq. 2.8 for the transitions $\pm 1/2\,(I_{z,g}) \rightarrow \pm 1/2\,(I_{z,e})$ and $\pm 1/2\,(I_{z,g}) \rightarrow \pm 3/2\,(I_{z,e})$, respectively. Thus, for a quadrupole splitting of 0.6 mm/s, the beat period is about 87 ns long, as indicated in the plot. In case of the presence of a magnetic hyperfine field, ground state and excited state are both split up into multiple states. The possible six dipole transitions lead to more complicated beat pattern in the time domain as shown in Fig. 2.6(c). As in the Mössbauer transmission spectrum, the relative weight of the different dipole transitions are a function of the magnetic hyperfine field orientation and the polarization of the incident X-ray pulse. Since the synchrotron X-ray pulse is highly polarized, the orientation of the magnetic hyperfine field can often be precisely determined via the temporal decay. Nuclear resonance scattering at synchrotrons therefore allows to measure not only the magnetic field strengths but also the field orientation inside nanostructured materials at the position of the resonant nuclei relative to the wave vector of the incident photon.

Not only the orientation of the magnetic field, but also of the electric field gradient has an effect on the temporal decay pattern for polarized photons. Since a directed electric field gradient is typically only present in single crystals, this influence on the temporal decay does not play a role in this work. An overview over various polarization effects in the magnetic and electric field gradient cases is presented in [Rö04].

In summary, nuclear resonance scattering of synchrotron radiations allows to measure the hyperfine structure in the time domain. The coherent nature of the scattering leads to an incorporation of interference effects, i.e. phase relations between the possible transitions play an important role. In combination with the intense, highly polarized and focused X-ray pulse, the hyperfine structure can be precisely investigated even in nanostructured materials, such as thin films.

2.2.4. Nuclear inelastic scattering

The Mössbauer effect relies on the recoilless absorption and emission of γ-rays, or X-rays in the case of synchrotron radiation. If, however, an absorption event is not recoilless, the recoil energy is transferred to crystal vibrations, i.e. phonons are created. Thus, even though in typical Mössbauer experiments unwanted, the recoil process provides information about the vibrational properties of a material. To specifically investigate the recoil effect, the energy transfer from the incident radiation to the material must be controlled. For this purpose, the incident radiation is energetically detuned so that it can only resonantly interact with the nuclei, if a phonon with an energy equal to the detuning energy is created or annihilated. Therefore the energy detuning must be in the range of typical phonon energies, thus in the milli electronvolt regime. Essentially, the energy dependent nuclear incoherent absorption cross-section is measured, which gives access to the phonon density of states of the material [Sin60]. While the measurement can be performed by employing conventional Mössbauer spectroscopy, the low signal strengths lead to unrealistic long measurement times [Sin60]. Therefore, as the incoherent counterpart to nuclear resonant scattering, nuclear inelastic scattering can be performed at synchrotrons using the intense X-ray pulses. The X-rays get energetically detuned around the nuclear resonance and the resonantly incoherently delayed scattered intensity is detected in the time domain. The obtained incoherent spectrum gives direct access to the phonon density of states of the resonant material. The theoretical principles of this technique are briefly explained in the following.

Incoherent resonant scattering can occur via two effects: Nuclear fluorescence or internal conversion. If a nucleus decays via internal conversion, the decaying nucleus is “tagged”, which means that the nuclei are not indistinguishable anymore. The coherence is therefore destroyed. The direction of subsequent emission of decay products, such as Auger electrons

or atomic fluorescence radiation, must be therefore independent of the momentum transfer of the scattering event and is isotropic. The nuclear fluorescence occurs when the nucleus decays via the "normal" radiative channel, but the eventual ground state of the nuclear ensemble differs from the ground state before excitation, for example when the vibrational state of the crystal changes after a recoil process. Then, the nucleus is again "tagged" and the coherence is destroyed.

In general, the measurement of the incoherent intensity is preferred via atomic fluorescence following the internal conversion process, not only because the mechanism is inherently incoherent, but also since the internal conversion process is for most isotopes the dominant decay channel, i.e. $\alpha > 1$ with α being the internal conversion factor. However, for some Mössbauer isotopes, such as ^{119}Sn, this is not feasible. As described in section 2.1, the internal conversion process of a decaying ^{119}Sn nucleus leads to the emission of atomic fluorescence photons with energies $< 4\,\mathrm{keV}$, which is too low to be effectively detected. Therefore, the 23.88 keV nuclear fluorescence radiation is typically used for recording the incoherent scattered intensity.

To detect the nuclear fluorescence, the detector needs to be placed where coherent scattering is forbidden. For example, in thin film experiments, which are done in a grazing incidence setup, coherent scattering occurs along the reflection and transmission channel. Thus, the incoherent detector is typically placed above the sample. The measurement in the time domain is convenient since it allows an easy separation of the fast non-resonant ($< 1\,\mathrm{ns}$) and the slow resonant incoherent scattering. Also a possible coherent scattering with phonons, called coherent inelastic scattering, happens in the fast time regime since it is limited by the phonon lifetime, which is about $10^{-10}\,\mathrm{s}$ to $10^{-12}\,\mathrm{s}$ [Rö04].

The incoherently scattered intensity is proportional to the total absorption cross section of Mössbauer resonances [Stu99b]. Therefore, the theory developed for conventional Mössbauer spectroscopy can be applied for nuclear inelastic scattering. [Sin60] derived the absorption cross section σ_a from the neutron scattering theory, which results in

$$\sigma_a(E) = \frac{\pi\sigma_0\Gamma_0}{2} S(E), \tag{2.16}$$

with σ_0 the maximum resonant absorption cross section, as defined in Eq. 2.14, and the normalized energy dependent probability of absorption per unit energy S. In general, the probability S depends also on the direction of the incidence X-rays, $\vec{k}_0$, for anisotropic

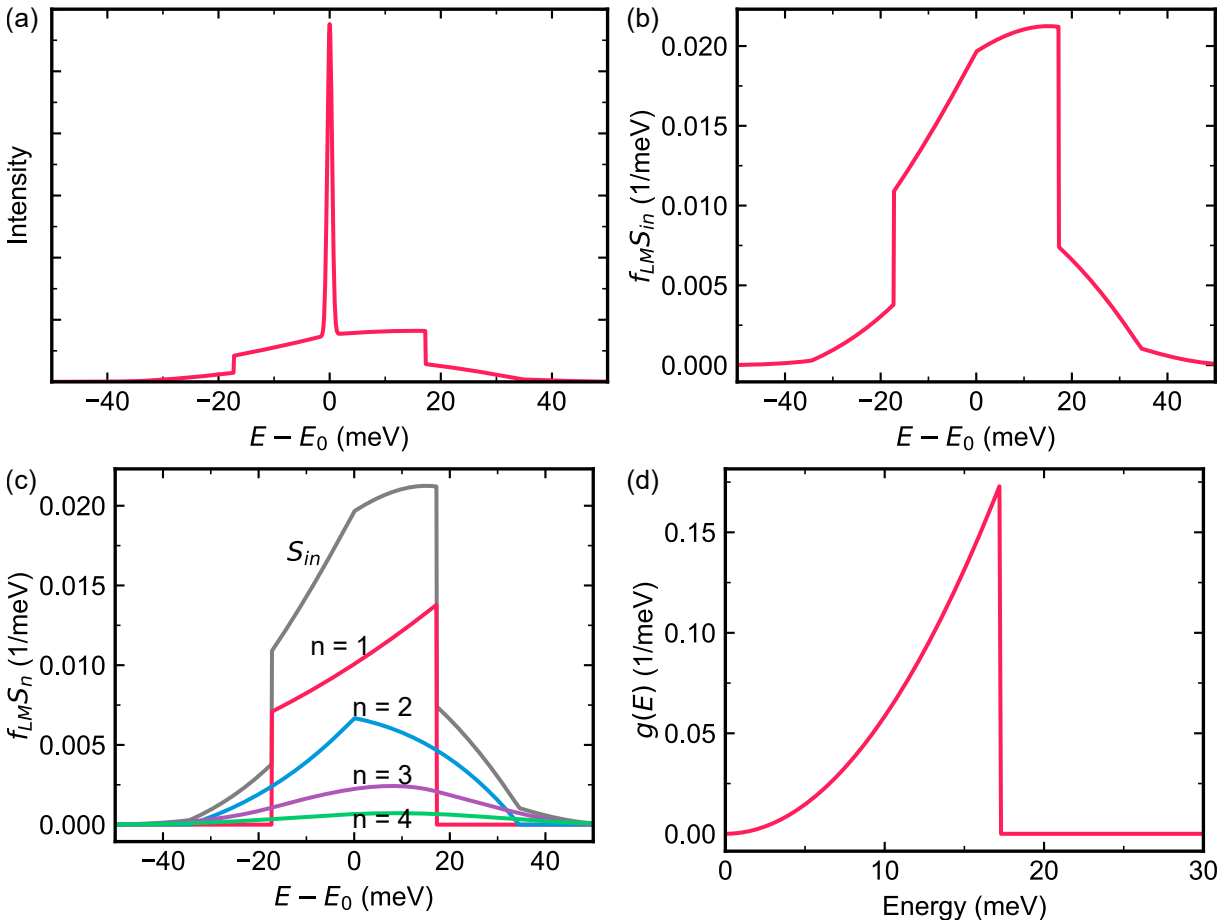

Figure 2.7.: Simulated nuclear inelastic scattering experiment for a material with a Debye vibrational behavior ($f_{LM} = 0.26$) at different analysis steps: (a) Incoherently scattered intensity as a function of the photon energy detuned around resonance, (b) the inelastic absorption probability per energy, $f_{LM}S_{in}$, after subtraction of the elastic peak, (c) extraction of the multi-phonon contributions, $f_{LM}S_n$, and (d) the phonon density of states.

crystals [Chu97].

In nuclear inelastic scattering experiments, the absorption cross-section, and thus the absorption probability, see Eq. 2.16, is directly measured by exciting the nuclei with an energetically detuned X-ray pulse. The energy detuning range is typical ±100 meV. The emitted photons which are incoherently scattered from the sample are counted and thus, an incoherent spectrum is obtained. A simulated spectrum is shown in Fig. 2.7(a) for a material with a Debye vibrational behavior and a phonon cut-off energy of 17 meV (corresponds to a Lamb-Mössbauer factor of 0.26). In the negative part of the spectrum, $E < E_0$,

the incoming photons have not enough energy to excite the nuclei directly. Therefore, the resonant scattering is accompanied by the annihilation of phonons. In the positive part, $E > E_0$, the interaction is connected with the creation of phonons. At exact resonance, $E = E_0$, the photons resonantly excite the nuclei without any energy transfer, meaning an elastic process. The "elastic peak" occurs in the incoherent spectrum through incoherent spin-flip processes of the ground state, for example.

From the incoherent spectrum, the absorption probability S can be calculated via Eq. 2.16. The absorption probability is a sum of the elastic contribution, which is of delta-function-like shape at $E = E_0$, and the inelastic contribution S_{in}, which carries the interesting vibrational information of the resonant material. It is [Rö04]

$$S(E) = f_{LM}\delta(E) + f_{LM}S_{in}. \tag{2.17}$$

The spectral weight of the elastic contribution is equal to the Lamb-Mössbauer factor, while the spectral weight of the inelastic contribution is equal to $1 - f_{LM}$ [Sin60].

The calculated inelastic absorption probability $f_{LM}S_{in}$ is shown in Fig. 2.7(b). The inelastic absorption probability shows distinct regions, which are perfectly sharp in the simulation due to the assumed Debye-like phonon behavior. The reason is that not only one phonon can be created or annihilated but also multiple phonon interactions can occur. The inelastic absorption probability is a sum over the different probabilities that n phonons take part in the scattering process, thus $S_{in} = \sum_n S_n$. The statistical weight of each multi-phonon contribution can be expressed with the Lamb-Mössbauer factor, $w_n = (-\ln f_{LM})^n/n!$ [Rö04]. Thus, for a high Lamb-Mössbauer factor like $f_{LM} = 0.8$, the one-phonon contribution outweighs higher multi-phonon contributions by $w_1/w_{n>1} \approx 8$. The opposite is the case for a small Lamb-Mössbauer factor of 0.04 as found in β-Sn. Here, multi-phonon processes dominate, $w_1/w_{n>1} \approx 0.15$. In Fig. 2.7(c), the multi-phonon contributions to the total inelastic absorption probability are shown up to the order of four.

Finally, the one-phonon contribution, S_1, gives access to the phonon density of states $g(E)$ of the resonant material, given by, [Sin60],

$$S_1(E) = \frac{E_R g(|E|)}{E(1 - e^{-\beta E})}, \tag{2.18}$$

with $\beta = 1/k_B T$, where k_B is the Boltzmann constant ($= 1.381 \times 10^{-23}\,\mathrm{J/K}$) and T the temperature in Kelvin. It is insightful to rewrite Eq. 2.18 explicitly for negative energies and for positive energies, which results in

$$S_1(E) = \begin{cases} \frac{E_R g(|E|)}{|E|} \frac{1}{e^{\beta|E|}-1} & \text{for } E < 0 \\ \frac{E_R g(|E|)}{E}(1 + \frac{1}{e^{\beta E}-1}) & \text{for } E > 0 \end{cases}. \tag{2.19}$$

The factor $1/(\exp\beta|E| - 1)$ is equal to the Boson-Einstein statistic. The negative part describes the probability to annihilate a phonon, whereas the positive part describes the probability for a phonon creation. The ratio of both parts is given by $S_1(E > 0)/S_1(E < 0) = \exp(\beta|E|)$. Thus, incident photons with energies above the resonance have a higher chance to scatter inelastically than photons with lesser energy. This asymmetry can be seen in the spectrum shown in Fig. 2.7(a).

In Fig. 2.7(d) the Debye phonon density of states is shown, which was used for the simulation. The Debye model is characterized by the cut-off energy $E_{\mathrm{cut}} = k_B T_D$, where T_D is the material dependent Debye temperature. The Debye temperature is connected with the Lamb-Mössbauer factor via Eq. 2.11. The Debye phonon density of states is given by

$$g(E) = \begin{cases} \frac{3E^2}{(k_B T_D)^3} & \text{for } E \leq k_B T_D \\ 0 & \text{for } E > k_B T_D \end{cases}. \tag{2.20}$$

The phonon density of states used for the above described simulation has a Debye temperature of 200 K, which corresponds to $f_{LM} = 0.26$. The subsequent cut-off energy is here at 17 meV.

The above described procedure is valid for isotropic crystals, such as cubic lattices, or for systems, where an average over all crystal directions is probed, as for example in polycrystalline samples. In anisotropic cases, phonons are weighted by their projections along the direction of the incidence wave vector, $\propto |\vec{p}\cdot\vec{k}_0|$, with the phonon polarization $\vec{p}$. Therefore, in general, the inelastic scattering intensity gives access to a projected phonon density of states.

The obtained knowledge of the phonon density of states is highly valuable, as it determines the thermodynamical properties of the material. Within the harmonic approximation, e.g. the vibrational contribution to the internal energy per atom U, the mean

force constant per atom F or the vibrational entropy per atom S_{Vib} can be calculated via [Chu99]

$$U = 3\int_0^\infty g(E)E\left(\frac{1}{2} + \langle n(E,T)\rangle\right)dE, \tag{2.21a}$$

$$F = \frac{M}{\hbar^2}\int_0^\infty g(E)E^2 dE \quad \text{and} \tag{2.21b}$$

$$S_{\mathrm{Vib}} = 3k_B\int_0^\infty g(E)\left(\beta E\left(\frac{1}{2} + \langle n(E,T)\rangle\right) - \ln\left(e^{\beta E/2} - e^{-\beta E/2}\right)\right)dE, \tag{2.21c}$$

with $\beta = 1/k_B T$, the Bose-Einstein statistic $\langle n(E,T)\rangle = 1/(\exp\beta E - 1)$ and the mass of the resonant nucleus M. Additionally, the Lamb-Mössbauer factor can be calculated via Eq. 2.11, as well as several other thermodynamic quantities, such as the heat capacity or the sound velocity [Chu99]. In temperature dependent studies, also anharmonic deviations can be investigated.

Since nuclear inelastic scattering is only sensitive to the resonant material, or more specific to the resonant isotope, the thermodynamic properties of a non-resonant material can be spatially resolved probed by measuring the phonons of the resonant material at the desired location inside the non-resonant material. This also works, if two different isotopes within the same material are used, e.g. ^{57}Fe inside of ^{56}Fe. In thin film experiments, for example, this spatially resolved method allows to investigate the vibrational behavior of single atomic layers [Sta07]. The same principle is applied to investigate the vibrational properties of tin films embedded in materials with very different vibrational properties, which will be later presented in this work.

3. Experimental methods

A variety of thin film samples with layer thicknesses ranging from 1 nm to 20 nm were fabricated to probe nanolayers of ^{119}Sn with synchrotron radiation. They were prepared by magnetron sputter deposition, whereby special care needs to be taken for tin films due to its low melting temperature. To check the smoothness and crystal structure of the layers, X-ray reflectometry and X-ray diffraction were employed. The synchrotron-based experiments were conducted at *PETRA III* in Hamburg (Germany) and at the *Advanced Photon Source* (APS) in Argonne (in Illinois, USA). In the following a description of the sample preparation and characterization techniques as well as of the methods used at the synchrotron facilities, namely nuclear resonance scattering and nuclear inelastic scattering is provided.

3.1. Thin film preparation with magnetron sputter deposition

Magnetron sputter deposition is a plasma-based physical vapor deposition technique. The desired atomic species to be deposited are sputtered from a target by ion bombardment. On a substrate close to the target, the vaporized atoms or clusters of atoms will condense and eventually form thin films. The desired thickness is controlled by the process time. A wide range of metals and also insulators can be used as target materials. The sputter process and important sputter parameters will be briefly explained in the following.

The sputter process is carried out in a high-vacuum environment, reducing the possibility of unwanted contamination in the films. A picture of a sputter chamber, which was used in this work, is shown in Fig. 3.1(a). A sketch of the process is shown in Fig. 3.1(b). In the plasma-based technique, the vacuum chamber is filled with a working gas of high purity, most commonly argon.

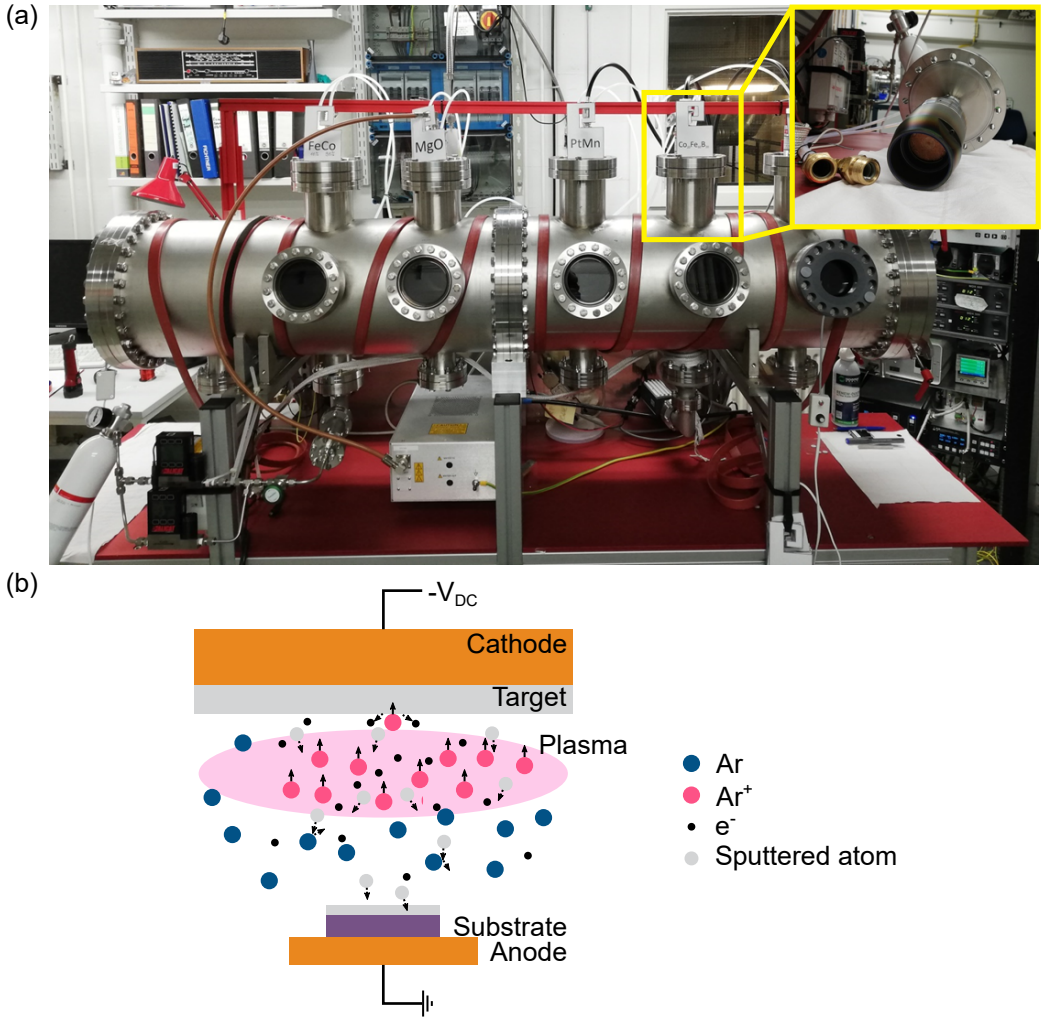

Figure 3.1.: (a) Picture of the high vacuum sputter chamber with up to five sputter guns. A standard 1.5 inch sputter gun is shown in the inset. (b) A sketch of the sputter process. The movement of the electrons towards the anode is not indicated for visual reasons.

To ignite a plasma, a negative DC voltage is applied on the target, also called source, whereby the rest of the chamber, including the substrate, is grounded. Positively charged argon atoms, which were ionized by cosmic rays for example, get accelerated towards the source, see Fig. 3.1(b). If the voltage is above a certain breakdown value, the ions can get fast enough to ionize more atoms. This results in an avalanche which produces ions and electrons and the plasma is ignited. An electrical current is now transported by the discharge. The argon ions eventually collide with the target material. The collision leads to an emission of atoms of the target material. The kinetic energy of the sputtered atoms

is a function of the kinetic energy of the argon ions prior to the collision, i.e. of the applied voltage.

In addition to the emission of target atoms, electrons are emitted as well. These secondary electrons are accelerated by the applied voltage away from the cathode and, after they collect enough energy, they can ionize even more argon atoms. The secondary electrons therefore "feed" the plasma with more argon ions. This is an important process, since it makes the plasma self-sustaining. In a magnetron setup, the secondary electrons are trapped by a magnetic field generated by an array of magnets placed behind the target. The field forces the electrons to gyrate in front of the target, thus, increasing the collision rate with argon atoms. In the magnetron configuration, the discharge becomes more efficient and therefore enhances the performance of the sputter process.

The radial distribution of the sputtered atoms is cosine-like, assuming that the ions hit the target under normal incidence. Therefore, the substrate is often placed straight under the target. Besides the deposition rate, the distance determines how homogeneous the substrate is coated. The atoms, once on the substrate, can form compact layers, islands or a mixture of both. This is affected by substrate temperature, energy of the incoming atoms and the type of materials chosen for substrate and target. The parameters have also an impact on the crystal growth of the layer, meaning if either a polycrystalline or an amorphous structure is preferred. It will be explained in more detail in the next section.

Sputtering with a DC voltage works for conducting target materials. However, for insulators, the deposited charge from the argon ions on the target surface cannot be transported. This leads to an undesired arching and eventually to a break-down of the plasma. To avoid that, a radio-frequency (RF, typically at 13.56 MHz) electrical potential is applied instead of a DC voltage. Thus, the target is positively charged during one half RF period, so that the now attracted electrons remove any positive charge which was built up on the target surface. Because the electrons are much lighter than the ions, more negative charge is net deposited on the target during the positive half of the RF period than positive charge during the negative half. Since charge neutrality at both electrodes needs to be fulfilled, the RF potential gets shifted to negative voltages so that the electrodes are longer negatively charged. This "bias" voltage builds up between the target and the plasma. Thus, even in the RF case, a net electric force accelerates the heavy argon ions towards the target, which allows a deposition of the insulating target material. In general, this effect occurs also at the other electrode, which is typically

the sputter chamber including the substrate. Since the chamber is much bigger than the target, however, the respective bias voltage at this electrode is much smaller. Nevertheless, this can lead to a sputtering off the substrate. For insulating targets, the bias voltage is especially high, since the target acts as an additional capacitor. Still, RF sputtering is also applicable to metal targets, although the deposition is not as effective as for DC sputtering. However, in some cases, the metal layer quality, such as smoothness or density, is improved when a RF voltage is used.

By adding other gases to argon, chemical reactions can be enforced, adding one more dimension to the sputter technique. This method is called "reactive" sputtering. A common used gas is oxygen to produce oxide layers. The oxygen reacts with the sputtered target atoms in scattering events or directly on the substrate or target. By tuning the ratio of argon to oxygen, different oxidation states of the deposited species can be reached. The eventual formation of oxide layers on the target surface, however, leads to a considerable low deposition rate, since oxide layers tend to have stronger binding energies than their metal counterpart. This "target poising effect" results in an unstable sputter condition, where small changes in the oxygen flow strongly affects the deposition rate. An overview can be found in [Dep10].

Many materials, especially metals, have known sputter parameters to produce films with the desired smoothness. However, some materials are more challenging, with one of those being tin. Since this work is based on tin films, the sputter deposition of metallic tin is explained in detail in the next section.

Besides metallic tin, also SnO_2 films were prepared. They are fabricated in the sputter chamber shown in Fig. 3.1(a) by reactive sputtering in a Ar-O atmosphere. The base pressure achievable here is about 2×10^{-7} mbar. Previous tin oxide studies, e.g. by Isidorsson *et al.* [Isi96; Isi98], suggest that the minimal oxygen partial pressure to fabricate tin dioxide films is in the range from 20% to 40% of the total Ar-O pressure. A lower oxygen partial pressure leads to a contamination of the tin dioxide film with tin monoxide. In this work, a partial oxygen pressure of 3.5×10^{-3} mbar is used at a total pressure of 1.3×10^{-2} mbar, thus, a 27% oxygen content. It is a balance between the highest possible oxygen pressure with a reasonable deposition rate.

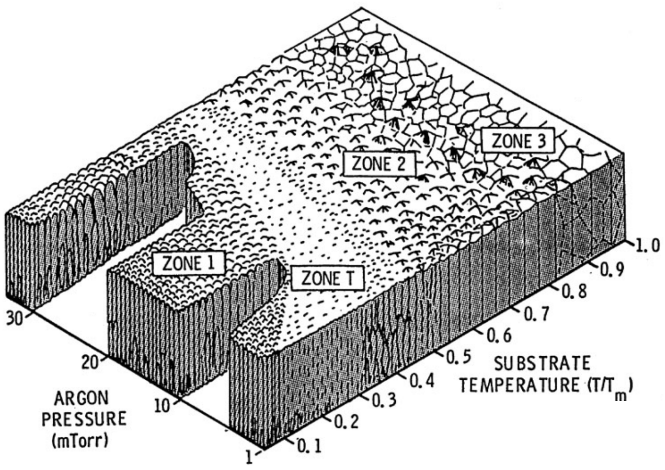

Figure 3.2.: The structure zone model initially proposed by Thornton ([Tho74]) provides a qualitative picture for the layer growth for magnetron sputtering in dependence of the substrate temperature, normalized by the materials melting Temperature T_m, and the working gas pressure (here Argon). Image taken from [Kus19].

3.2. Aspects of metallic tin thin film preparation

Metals with a low melting temperature, like tin, tend to form island structures instead of compact layers when they are deposited. Indeed, thin film studies on β-Sn were mostly focused on self-organized tin nanoislands [Hou17] or on films which were needed to be grown epitaxially [Hou20]. For this work, however, it is crucial to have films with a smooth interface. To understand the relation between substrate temperature and melting temperature, the "structure zone model" initially proposed by Thornton [Tho74], shown in Fig. 3.2, will be described in the following.

The zone model incorporates the interplay between the diffusion ability of adatoms on the substrate and the energy of the incoming sputtered atoms. Both properties are controllable by the substrate temperature and the pressure of the working gas. In the model, the structural film growth is divided into three zones with an additional "Zone T" existing for sputter deposition. In "Zone 1" at low substrate temperatures relative to the melting temperature, the adatoms have no energy to self-organize on the substrate. A fine porous column structure is created with an amorphous crystal structure. Higher working gas pressure enhances this effect since an increase in collisions between the sputtered atoms and the gas atoms leads to a decrease of the kinetic energy of the atoms (thermalization).

At lower pressure, however, collisions become more rare, and the sputter process results essentially in a particle bombardment on the substrate at an enhanced energy. Subsequently, the surface of the film gets flattened and the columns become wider. This region is called "Zone T". Still, the diffusion energy of the adatoms is too low to produce any crystallization, thus, the structure stays amorphous. This changes in "Zone 2". A higher substrate temperature leads to higher surface mobility of the adatoms. Crystallization takes place and the thin film properties become similar to their bulk counterpart. Due to the highly increased diffusion, the influence of the working gas pressure, or more specific, of the kinetic energy of the incoming atoms, is reduced. For sputter deposition, the film growth processes of "Zone T" or "Zone 2" are typically desired. They provide compact layers with flat surfaces and material properties similar to bulk. If the substrate is exposed to an even higher temperature, "Zone 3" will be reached. The diffusion energy becomes high enough to form macroscopically big crystallites which creates rough surfaces. For example, islands are assembled. In "Zone 3", the film surface gets typically so rough that material properties, e.g. the electrical resistance or optical properties, change.

The structure zone model is a qualitative description of the sputter process. However, an exact prediction of the zone borders requires to take into account additional effects, such as the mass of the sputtered atoms or the binding energies between adatoms.

Regarding the sputter process of tin, the low melting temperature of 232 °C leads to a ratio of substrate temperature to melting temperature of 0.59 at room temperature. Islands with lateral scales in the µm range and heights of several tens to hundreds of nanometers are formed, as shown e.g. by Houben *et al.* [Hou17]. The layer growth is therefore presumably in the region between zones two and three. Thus, to enforce a smooth film growth for low melting point materials, a cooling of the substrate is required. This technique is called vacuum-quenching and is often used with thermal evaporation. The substrate is cooled with liquid helium or nitrogen to diminish any diffusion energy of the adatoms. Accordingly, the layer growth is moved into "Zone 1". Buckel *et al.* [Buc52] employed this technique to investigate highly disordered tin films, which are typical for layers grown in "Zone 1".

In this work, vacuum-quenching was combined with magnetron sputter deposition. Therefore, not only "Zone 1", but also "Zone T" can be reached. The sputter chamber, in which the tin films are prepared, is shown in Fig. 3.3. In the chamber, the substrate is mounted on a small copper cone, which has two drilled holes, allowing a flow of liquid

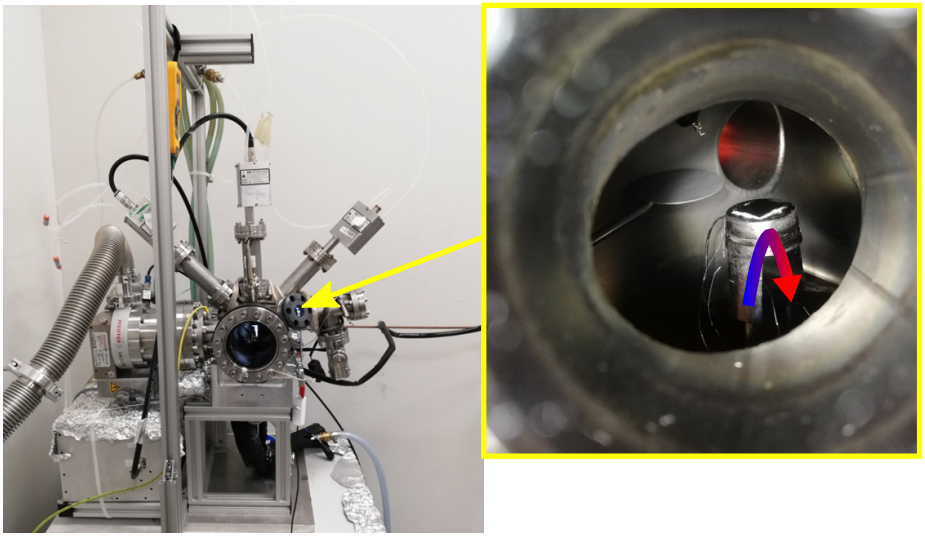

Figure 3.3.: A picture of the sputter chamber with an incorporated sample cooling system. The inset shows a view on the sample holder, with the liquid nitrogen flow indicated by the arrow.

nitrogen through the cone. The nitrogen flow is indicated by the arrow in the inset of Fig. 3.3. Since the sample holder is also a cold-trap for the residual gas, the substrate surface can be potentially contaminated during the cooling process. Therefore the chamber allows an ultra high vacuum base pressure of 4×10^{-8} mbar to 2×10^{-9} mbar. Once the necessary base pressure is reached, the copper cone is cooled down to 87 K within 10 min. Grease in between substrate and sample holder ensures that the substrate is as cold as the copper cone. With the cooled sample, the sputter process is started, whereby all materials, not just tin, are sputtered on the cooled substrate. The reason is to prevent any potential contamination on interfaces which might appear during the cooling process. The subsequent heating process to room temperature takes up to three hours.

The above described procedure leads to the ratio of substrate temperature to melting temperature of 0.17. The zone structure model predicts a film growth governed by "Zone T". Hence, a smooth and amorphous layer is expected. Due to the warming up process to room temperature, however, a recrystallization process is likely. Therefore a characterization of not only the layer thickness, but also layer roughness and crystal structure is required. The characterization methods are explained in the following.

3.3. X-ray thin film characterization

X-ray analysis methods are employed for controlling the quality of the prepared samples. The crystal structure is investigated by X-ray diffraction and the layer properties, such as thickness, roughness and density, is checked by X-ray reflectometry. For both methods, an X-ray tube is used which produces Cu-Kα X-rays at the wavelength of 1.54 Å (= 8.04 keV). A description of both methods is provided in the following.

3.3.1. X-ray reflectometry

In X-ray reflectometry, the specular reflection from a sample of an incoming X-ray beam is measured for different incidence angles. The reflected intensity is thereby modified by the sample structure due to internal refraction and reflection at interfaces. The measured angle dependency is a footprint of the electron density distribution in the sample and, thus, gives insight into thickness, density and roughness of the individual layers.

The photon propagation in a material is governed by its complex refractive index $\bar{n}$, which can be described by the scattering factors f_1 and f_2 by

$$\bar{n} = n + i\kappa \tag{3.1}$$

$$= 1 - \frac{\lambda^2}{2\pi}\rho_n r_e (f_1 + i f_2), \tag{3.2}$$

with n the (real) refractive index, κ the extinction coefficient, λ the X-ray wavelength, ρ_n the number density of the atom species and $r_e = 2.818 \times 10^{-15}$ m the classical electron radius. Away from any absorption edges, the real part, f_1 scales with the atomic number Z and the imaginary part is connected with the total photoabsorption σ_{ph} by $2\lambda r_e f_2 = \sigma_{\mathrm{ph}}$. The scattering factors can be looked up in databases such as of the CXRO [CXR].

If the complex refractive index is rewritten by $\bar{n} := 1 - \delta + i\gamma$, the quantities δ and γ are a measure of how close $\bar{n}$ is to 1, the refractive index of vacuum. In the hard X-ray regime (approximately 10 keV to 30 keV), δ ranges from 10^{-5} to 10^{-6} and γ ranges from 10^{-6} to 10^{-7}. Thus, the refractive index for materials are extremely close but smaller than one in the X-ray regime. Thus, refraction and reflection are weak in the X-ray regime. The fact, however, that the refractive index is smaller than one implies the strange conclusion that vacuum is the optically denser medium. The phase velocity of X-rays inside the material is

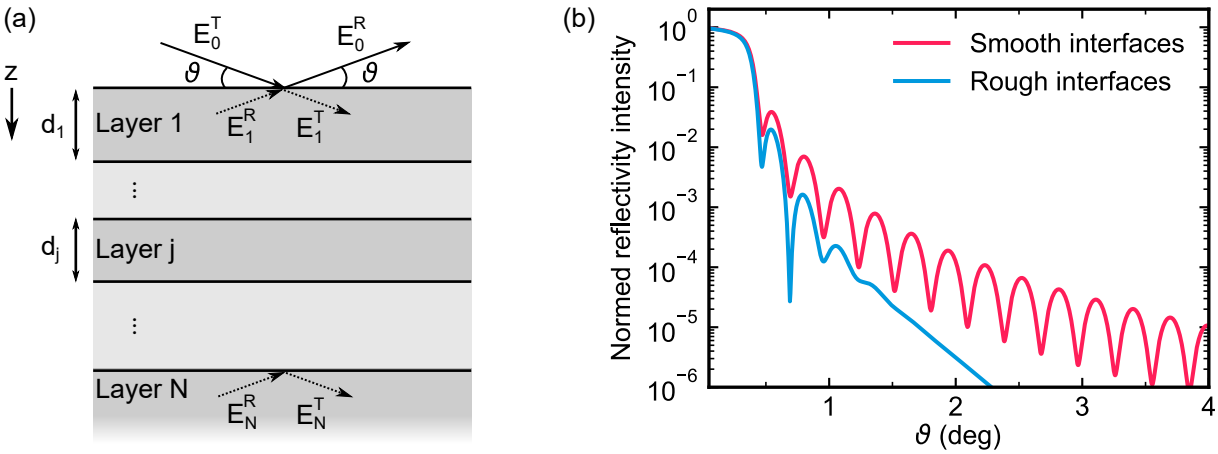

Figure 3.4.: (a) A sketch of a N-layer system with the electric fields in reflection and transmission direction indicated. (b) Simulated reflectivity of a 15 nm tin film on a silicon substrate without (red) and with roughness (blue). In the latter case, a roughness of 15 Å and 5 Å is assumed for the tin layer and silicon substrate, respectively.

therefore bigger than in vacuum. Accordingly, total reflection must occur below a certain critical angle ϑ_c. With Snell's law ($\cos\vartheta_c = \bar{n}$), and assuming that $\gamma \ll \delta$, it can be written for small angles as

$$\vartheta_c = \sqrt{\frac{\lambda^2 \rho_n r_e f_1}{\pi}}. \tag{3.3}$$

It follows that the critical angle scales with the density and atomic number Z of the materials. Typical values are in between 0.1°-0.5°. Below the critical angle, only an evanescent wave penetrates a few nanometer into the sample. When the incidence angle equals the critical value, a wave propagates along the surface which constructively interferes with the incoming wave forming a standing wave.

When the incidence angle is bigger than ϑ_c, the X-rays propagate through the sample. At each interface, the continuity of the tangential component of the electric field and the magnetic field has to be ensured. This is imposed by Maxwell's equations. Based on this, a recursive formula can be derived, known as Parratt's formalism, to calculate the total reflection coefficient [Par54]. Another method, but based on the same principle, is the transfer matrix method. In this formalism, each layer is described by a (2x2)-matrix. The matrix product of all layer matrices is the "transfer matrix", which connects the incident and reflected electric field above the sample, (E_0^T, E_0^R), with the transmitted and the potential incoming electric field from below the last layer, (E_N^T, E_N^R), as indicated for

an exemplary N-layer system in Fig. 3.4(a). Thus, it is,

$$\begin{pmatrix} E_N^T \\ E_N^R \end{pmatrix} = \mathbf{M} \begin{pmatrix} E_0^T \\ E_0^R \end{pmatrix}, \tag{3.4}$$

with $\mathbf{M}$ being the transfer matrix. With an incident electric field of $E_0^T = E_0$ and the assumption that there is no incoming electric field from the backside of the sample ($E_N^R = 0$), the reflectivity R, i.e. the intensity of the reflected electric field, is calculated via the matrix elements M_{ij} of $\mathbf{M}$ by

$$R = |r|^2 := \left| \frac{E_0^R}{E_0} \right|^2 = \left| -\frac{M_{21}}{M_{22}} \right|^2. \tag{3.5}$$

This method is also applicable for calculations of the electric field amplitude within the sample.

Since layers are never perfectly smooth, a roughness model has to be included in the transfer matrix method. Typically, the deviation from a perfect interface is assumed to be Gaussian-like. The roughness values given throughout this work are therefore the standard deviation σ of this Gaussian distribution.

The reflectivity R is measured in X-ray reflectometry experiments. A simulated reflectivity is shown in Fig. 3.4(b). The simulated sample consists of a 15 nm tin film on a silicon substrate. If no roughness is assumed the interferences within the sample are visible by a beat pattern. The length of the beat period reflects the layer thickness. When roughness is included, the reflection intensity decreases strongly with increasing angles and the beat pattern becomes washed out. In this work, the software GenX (`genx.sourceforge.io`) is used to fit the above described model to experimental reflectivity data. Layer thicknesses, roughnesses and densities are obtained.

3.3.2. X-ray diffraction

The X-ray reflectometry measurements are done at incident angles up to $\approx 5°$. At higher reflection angles, the X-rays can probe the crystal structure of the sample. If the reflection

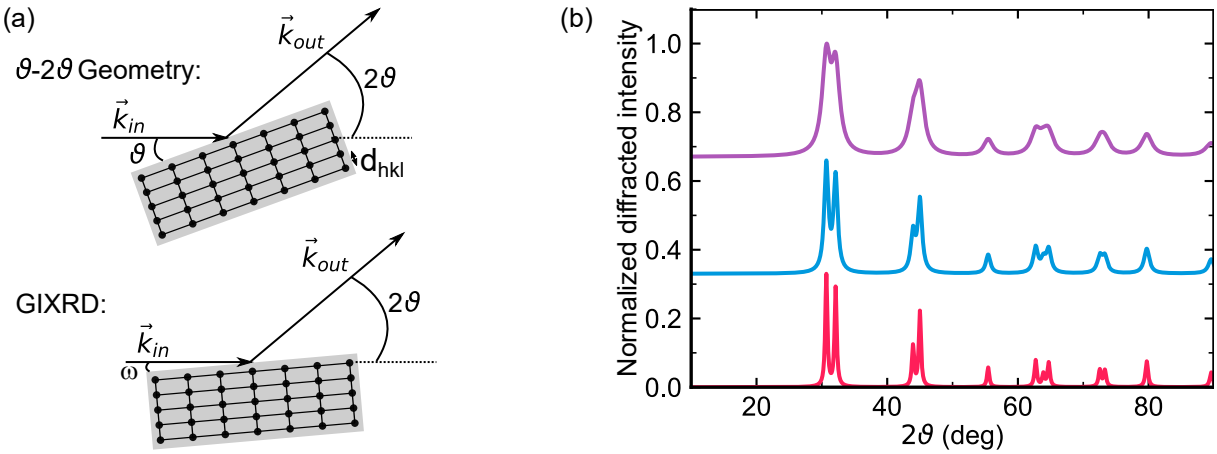

Figure 3.5.: (a) Sketch of two possible XRD geometries: The standard ϑ-2ϑ geometry, where incidence and reflection angle are equal, and the grazing incidence XRD (GIXRD) where the incidence angle is set to a small angle ω and only the reflection angle 2ϑ is scanned. Exemplary XRD spectra of a β-Sn film with randomly orientated crystallites of sizes 5 nm (purple), 10 nm (blue) and 20 nm (red) are depicted in (b). The spectra are normalized to 0.33 and the zero positions are offset for the middle and upper spectra by 0.33 and 0.67 for visual reasons.

angle fulfills the Bragg condition

$$i\lambda = 2d_{hkl}\sin\vartheta_B, \quad i = 1,2,3,\ldots \tag{3.6}$$

constructive interference from X-rays scattered at the crystal plane (defined by the Miller indices hkl) with the inter-plane distance d_{hkl} occurs. The angle is then called Bragg angle ϑ_B. The diffraction measurement, thus, probes the reciprocal crystal lattice of the sample. With that, not only crystalline phases of the thin films can be identified, but also crystallite size, microscopic strain and other crystal parameters.

There are multiple measurement geometries, two of them are depicted in Fig. 3.5(a). In the standard $\vartheta - 2\vartheta$ geometry, the incidence angle on the sample is ϑ and the detector is positioned at 2ϑ in respect to the incidence beam. The momentum transfer $\vec{q} = \vec{k}_{\text{out}} - \vec{k}_{\text{in}}$ is therefore normal to the sample surface. In this geometry, crystal planes, which are parallel to the surface, are probed. For thin films, however, this geometry is disadvantageous, since at high incidence angles, the effective X-ray path through the thin film is extremely short. That means, the signal strength is drastically reduced. Therefore for thin films,

the incidence angle is kept at a small angle ω, typically between 0.5° and 3°, and only the detector angle 2ϑ is scanned. This is called grazing incidence X-ray diffraction (GIXRD). However, while only scanning the detector angle, the momentum transfer direction is changing as well, i.e. q is a function of 2ϑ. The probed crystal planes are therefore not parallel to the sample surface anymore. Typically in thin films, the crystallites and therefore the crystal planes within the film are randomly oriented, so that the momentum transfer orientation does not play a role. Thus, both measurement geometries obtain the same result. This changes, when the crystallites have a preferred orientation or in the extreme case of single crystals.

In addition to the crystal identification, the XRD pattern provides information, for example, about internal strain and crystallite sizes. Both influence the width of the Bragg peak, where a high strain and/or small crystallite size lead to a broadening of the Bragg peak. The Scherrer equation relates the crystallite size L to the peak width $\Delta\vartheta_B$ of a Bragg peak at the incidence angle ϑ_B by [Smi09]

$$L = \frac{K\lambda}{\Delta\vartheta_B \cdot \cos\vartheta_B}, \tag{3.7}$$

where λ is the wavelength of the X-rays. The peak width $\Delta\vartheta_B$ is equal to the full width at half maximum (FWHM) of the Bragg peak. The Scherrer constant K reflects the assumed geometry of the crystallite and its crystal structure and it ranges from $0.8 - 1.0$. As a good approximation, especially for cubic or platelet shapes, a value of $K \approx 0.9$ is typically assumed [Lan78; Smi09], which is why this value is used in this work. In Fig. 3.5(b), a simulated XRD pattern for a tin film in the β crystal phase is shown for the crystallite sizes 5 nm (purple), 10 nm (blue) and 20 nm (red). As the crystallites get smaller, double peaks merge together and become harder to identify. In near-amorphous films with crystallite sizes of below 1 nm, only very broad peaks can be measured.

For this work, GIXRD was extensively used to pre-characterize tin films in their growth behavior.

3.4. Thin film cavity design

The electric field inside a layered structure is strongly impacted by the refraction and reflection at each interface, as described in section 3.3.1. By properly adjusting each layer

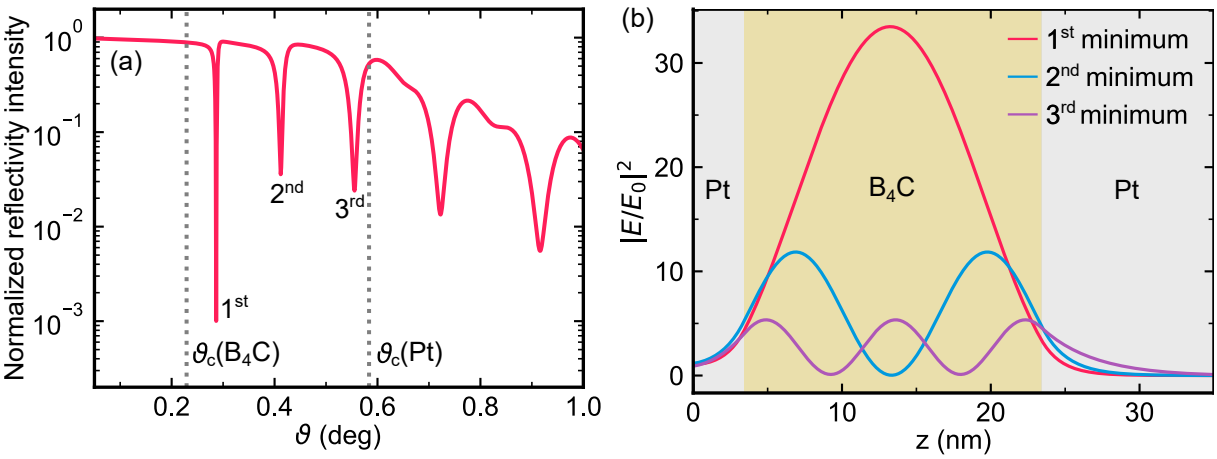

Figure 3.6.: (a) Reflectivity of 20 nm B_4C layer sandwiched between 15 nm (below) and 3.4 nm (above) Pt on a silicon substrate. The critical angles of B_4C and Pt are indicated. Due to a coupling of the evanescent wave into the B_4C layer, standing waves are formed inside the minima labeled in (a). The electric field inside the layer, (b), is highly enhanced inside the modes.

thickness and choosing the proper materials, the reflections at each interface can lead to a constructive interference of the electric field inside the layered structure, and thus to a field enhancement. This field enhancement is an essential criterion for the design of thin film cavities.

By sandwiching an optically thin layer (low Z and/or low density) in between two optically dense layers (high Z and/or high density), a cavity structure can be build. The critical angle of the low density layer, also called guiding layer, is lower than of the high density layers, called mirror layers. That means, there exists an angular range, where the mirror layers are totally reflecting, but the guiding layer allows wave propagation. If the thicknesses of the top mirror layer and the guiding layer are adjusted properly, the evanescent wave travels through the mirror layer, and forms a standing wave in the guiding layer. In an ideal thin film cavity, the field is "trapped" in between the mirror layers until the field finally couples out at the lateral borders of the sample. This "waveguide" mode is therefore visible as a sharp and deep minimum in the reflectivity. An exemplary reflectivity is shown in Fig. 3.6(a) for a 20 nm boron carbide layer ($\rho(B_4C) = 2.3\,g/cm^3$) sandwiched between a 3.4 nm thick Pt layer on top and a 15 nm thick Pt layer below ($\rho(Pt) = 21.45\,g/cm^3$). The boron carbide layer is thick enough to allow also higher order standing waves at higher angles. The depth dependence of the electric field intensity

inside the sample is shown in Fig. 3.6(b). The field intensities at the maxima of the standing waves are highly enhanced, in the first minimum by more than a factor of 30.

The field enhancement of the thin film cavity allows the generation of a strong electric field at a specific position inside the guiding layer. In the case of nuclear resonance scattering, for example, it provides a useful tool to tune the interaction between the X-ray pulse and the nuclei, which is important for nuclear quantum optics, e.g. [Röh10; Hab17]. Additionally, the increased field results in an increased interaction probability, if the material of interest is placed at the position of the electric field maximum. Thus, a higher signal strength is expected.

3.5. Synchrotron based experiments: NRS / NIS

The main experimental part of this work was conducted at synchrotron facilities. Instead of accelerating particles as in synchrotrons for high energy physics, these synchrotrons are designed to store as many particles as possible at a certain energy. Hence, the facilities are also called storage rings. They provide highly polarized, intense and focused X-ray pulses, which are necessary to investigate nuclear resonances in thin film samples. In the following, the experimental setup used to probe elastic (NRS) and inelastic (NIS) properties are described. The theoretical background for both techniques are provided in the previous sections 2.2.3 and 2.2.4.

A sketch of a storage ring with a beamline set up for nuclear resonance scattering is shown in Fig. 3.7(a). The depicted setup is based on the beamline P01 at PETRA III. At storage rings, the X-ray pulses are produced by electron bunches which are forced into a trajectory following the circumference of the ring (at PETRA III: 2.3 km, APS: 1.1 km). Dipole, quadrupole and sextupole magnets keep the electron bunches inside the ring and focus them as tight as possible. The electron energy hereby is a few GeV, periodically injected by pre-accelerators.

Every time an electron bunch is bent by a dipole magnet, light is tangentially emitted. The opening angle is proportional to the inverse of the Lorentz-factor $\gamma = 1/\sqrt{1 - v^2/c^2}$. Due to this relativistic effect, the light is strongly collimated. The resulting X-ray pulse is highly intense, however, energetically broad ($\sim 10^4$ eV). For the purpose of this work, the light must be as monochromatic and intense as possible, since the nuclear resonance has an extremely narrow energy linewidth in the sub-μeV range. A narrower energy spectrum

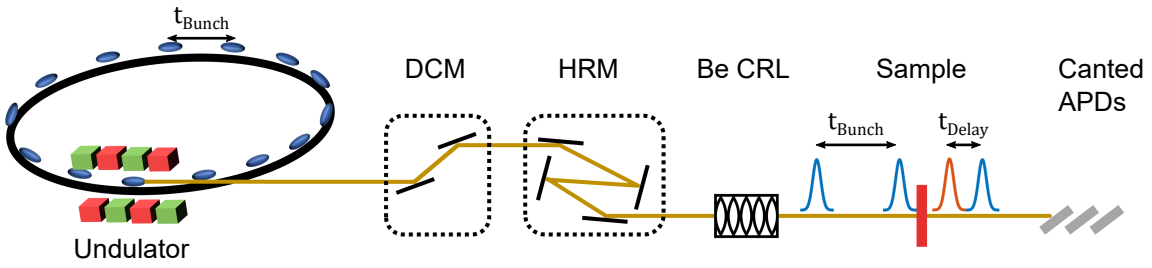

Figure 3.7.: A sketch of the beamline layout at P01 at PETRA III. The X-ray pulse generated in the undulator is monochromized first by a double crystal monochromator (DCM) and then by a high-resolution monochromator (HRM). A beryllium compound refractive lens (CRL) focuses the pulse on the sample. The delayed signal is measured by canted avalanche photon diodes (APD).

is provided by undulators.

An undulator consists of a periodic array of magnets, as indicated in the sketch in Fig. 3.7(a), forcing the electrons into a sinusoidal motion. By tuning the undulator parameters correctly (e.g. period length and magnetic field strength), the wavy motion leads to a constructive interference of the light emission. The light is therefore even more collimated, intense and energetically narrower ($\sim 10^2$ eV). At the beamline P01 at PETRA III, for example, where two undulators are employed, this leads to about 10^{15} photons per second in a 10 eV bandwidth when a center energy of 10 keV is chosen.

At the beamline, the energy linewidth gets reduced by first a double crystal monochromator (DCM) and finally by a high-resolution monochromator (HRM), specifically designed for the nuclear resonance energy. Both monochromators use well-defined Bragg peaks of single crystals, mostly silicon. At P01, the HRM is realized by a four-crystal setup, as sketched in Fig. 3.7(a). An even more sophisticated six-reflection HRM is available at the APS at beamline 30-ID where the center crystals are cooled by liquid nitrogen. The cooling adds stability to the reflections, which allows a higher photon flux through the HRM. The monochromator setups lead eventually to an energy linewidth of about 1.3 meV to 0.6 meV. Additionally, the HRMs are tunable by about ± 100 meV, which covers the energy range needed for nuclear inelastic experiments.

If needed, focusing of the X-ray pulse is possible by multiple beryllium lenses, called compound refractive lens (CRL). As previously stated, refraction is weak in the X-ray regime, therefore multiple lenses are needed. For grazing incidence experiments, the vertical focus is mostly important since the footprint of the beam is large at small incidence

angles of about 0.1°. Here, a focus of about 10 µm to 20 µm is possible. The horizontal focus is only needed, if the sample has lateral structures with dimensions below 2 mm. A description of the sample environment and the detection for experiments using nuclear resonance scattering and nuclear inelastic scattering is provided in the following.

3.5.1. Nuclear Resonant Scattering

In a nuclear resonant scattering experiment, a sample consisting of a resonant material gets excited by an X-ray pulse and the coherently elastically scattered photons are detected together with their arrival time relative to the moment of the pulse excitation, i.e. the time delay. In the sketch of Fig. 3.7(a), the sample is mounted in the forward scattering geometry, meaning that the time delayed response is measured in the coherent forward scattering channel. The nuclear response after the X-ray excitation is detected by avalanche photon diodes (APD). When photons are absorbed in the absorption region of the APD, charge carriers in the semiconductor are generated. In the gain region, an avalanche effect starts, which eventually results in the electronic detection of the event. To optimize the photon absorption probability without increasing the absorption region thickness, which would lead to a reduction of the temporal resolution, multiple and canted diodes are used. The subsequent electronics detect single photon events in a temporal relation to the exciting synchrotron X-ray pulse, given by the time delay t_{Delay}. Therefore, the maximum time range is given by the time between two electron bunches, t_{Bunch}, 192 ns at PETRA III and 153 ns at the APS in their timing bunch filling. The time resolution is limited by the electron bunch length, the APD absorption region thickness and the electronics, and is approximately 0.5 ns. An overview about the detection scheme can be found in [Rö04].

In this work, the coherent signal for thin film samples is measured in a $\vartheta - 2\vartheta$ geometry with grazing incidence angles of about 0.1° – 1°. In Fig. 3.8, a picture of a typical experimental setup is shown. The X-ray pulse, indicated by the arrow, hits the sample, which is tilted by ϑ relative to the beam direction. The detector, which is here an assembly of four canted APDs, is tilted by 2ϑ relative to the beam. The setup further contains a Mössbauer drive installed in the reflected beam path. With a reference absorber mounted on the drive, information about the energy spectrum of the resonantly scattered photons from the sample can be gathered. The setup with the Mössbauer drive is used to measure

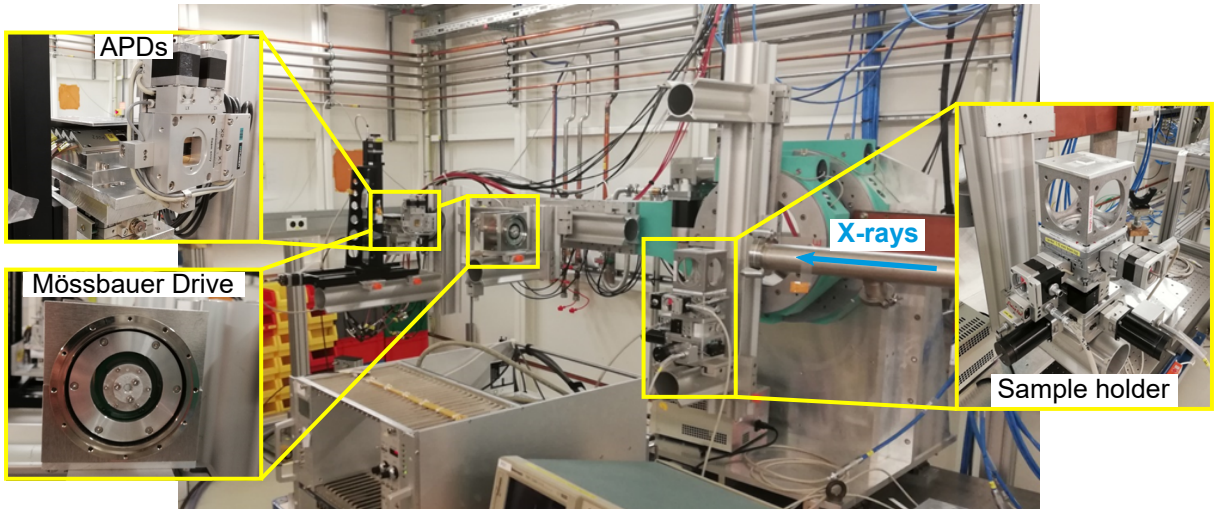

Figure 3.8.: Photo of the experimental setup for measuring the collective Lamb shift. The X-ray pulse (blue arrow), hits the by ϑ tilted sample and the reflected time delayed signal is measured by four APDs, which are tilted by 2ϑ. An additional Mössbauer drive is placed in the reflected beam path to gather additional energy information of the time delayed photons.

the collective Lamb shift and will be explained in section 3.5.2.

In the nuclear resonance scattering setup, two signals are measured: The prompt signal and the delayed signal. The prompt signal is collected without any time delay. Therefore it probes the fast, meaning $< 1\,\text{ns}$, electronic interactions of the X-ray pulse with the sample, which were described in section 3.3.1. Consequently, X-ray reflectivity curves are obtained in a ϑ–2ϑ scan. The delayed signal is measured after a certain time window after the prompt, the veto. The veto is necessary for the electronics to recover after the prompt signal was measured, which is several orders of magnitude stronger than the delayed signal. Typical veto times are in the region of 10 ns after the prompt signal. If this time is set too short, the delayed signal will be altered by the prompt, especially at early times. By time integrating the delayed signal for each angle in a ϑ–2ϑ scan, a reflectivity curve of only the nuclear response is obtained. The nuclear reflectivity contains valuable spatial information about the resonant layer.

At a fixed incidence angle, the nuclear response after excitation can be measured in a time resolved manner. As explained in the theoretical sections, the temporal nuclear decay pattern provides information about the hyperfine structure of the resonant nuclei. The

incident angle determines the X-ray radiation field strength within the thin film sample. Consequently, different parts of the thin film sample can be investigated by choosing the correct angle. At the critical angle, for example, only the surface layer, and a few nanometers below, is probed.

The obtained data are analyzed by employing the software *CONUSS* developed by W. Sturhahn [CON] and the python package *pynuss* (version 1.0.0) developed and provided by J. Evers and K. P. Heeg[1].

3.5.2. Energy-time-domain interferometry

In nuclear resonance scattering, the coherent nature of the nuclear excitation is measured in the time domain. Since only intensities are recorded, a Fourier transformation of the results into the energy domain cannot be directly done. Especially a shift in the energy cannot be determined by the Fourier transformation. One way to obtain information about the energy spectrum is by drawing conclusion from the hyperfine parameters obtained from the temporal decay. With the knowledge of the hyperfine parameters, the layer thickness and the incidence angle the energy spectrum of a sample can be modeled. However, this method is subject to many uncertainties arising from measurement errors for each parameter.

A direct measurement of the energy spectrum can be obtained by measuring the combined temporal response of the sample and a reference absorber. In this interferometric approach, the reference absorber is mounted on a Mössbauer drive, as shown in Fig. 3.8 so that an energy-time-domain measurement can be performed. The experimental setup was for example used by Röhlsberger *et al.* to investigate the collective Lamb shift with nuclear resonances [Röh10]. The resonant photons scattered from the sample can again resonantly interact with the reference foil. Energy information about the sample is gained since the reference absorber is energetically detuned by the Mössbauer drive similar to conventional Mössbauer spectroscopy. However, in contrast to the conventional technique, the coherent scattering can be measured and thus the interferences of the combined sample-reference absorber system. The interference pattern is recorded as a function of the delay time of the photons measured in the APDs and the Mössbauer drive velocity, i.e. the energy detuning, of the reference absorber.

[1]Max-Planck-Institut für Kernphysik, 69117 Heidelberg, Germany.

In this work, the reference foil consists of non-enriched SnO_2 powder, which is firmly attached between two Kapton foils. The Doppler drive in the experiment is driven in the constant acceleration mode, i.e. the voltage driving the coils of the drive follows a periodic triangular function. The periodicity of the triangular function matches the resonance frequency of the Doppler drive setup. If a delayed signal is measured by the APD, the corresponding voltage of the Doppler drive is recorded. The voltage is proportional to the current velocity of the drive, which is the quantity of interest. Therefore, a voltage-to-velocity calibration has to be done.

For the experiments conducted in this work, the velocity calibration was done by using the isomer shift between different tin compounds: A SnO_2 powder and a β-Sn foil, which were placed at the sample position of the setup. Together with the SnO_2 reference absorber on the Doppler drive, the zero velocity position is determined (SnO_2 powder) and the position at 2.56 mm/s (isomer shift between β-Sn and SnO_2).

In total, a two dimensional histogram is measured, where the delayed events are counted as a function of the Doppler drive velocity and time delay after excitation. The resulting two dimensional plot is then the combined response of sample and reference foil after X-ray excitation. If an event is measured, four possible interaction pathways are possible. First, the X-ray pulse does not interact at all, i.e. neither with the reference foil nor the sample. The X-ray pulse is therefore just the prompt signal, so it can be removed by only counting events from a certain time delay on, typically > 10 ns. The other interaction pathways include the interaction with either the reference foil or the sample or with both. Events originating from one of these three interaction pathways have a time delay, so they will be all counted. The measured intensity for an event with a delay time t and a detuning E_D is related to the complex reflectivity coefficient of the sample $r(E)$ and the complex transmission coefficient of the Doppler shifted reference foil $t(E - E_D)$, by [Röh10]

$$I(E_D, t) = \left| \mathcal{F}\left[r(E) t(E - E_D) \right](t) \right|^2 , \tag{3.8}$$

where $\mathcal{F}$ denotes the Fourier transformation. The quantity of interest, $r(E)$, can be indirectly determined with a comparison of the measurement data and with simulations, for which $r(E)$ is assumed and the intensity is calculated by Eq. 3.8.

A direct determination of $|r(E)|^2$ is also possible for certain conditions. For that, it is helpful to look closer at the reflectivity coefficient of the combined response, $r_c(E, E_D) =$

$r(E)t(E-E_D)$. Both, the reflectivity coefficient of the sample and the transmission coefficient of the reference absorber, can be separated into a constant electronic and an energy dependent nuclear coefficient, e.g. $r(E) = r_e + r_N(E)$. Thus, the combined reflectivity coefficient can be written as,

$$r_c(E, E_D) = (r_e + r_N(E))(t_e + t_N(E - E_D)) \tag{3.9}$$

$$r_c(E, E_D) = r_e t_e + r_e t_N(E - E_D) + t_e r_N(E) + r_N(E) t_N(E - E_D). \tag{3.10}$$

The expansion made in the last step reflects the four possible interaction pathways. The Fourier transformation into the time domain leads to the temporal response of the combined setup, $\tilde{r}_c(t, E_D)$, given by,

$$\tilde{r}_c(t, E_D) = r_e t_e \delta(t) + r_e \tilde{t}_N(t) e^{iE_D t/\hbar} + t_e \tilde{r}_N(t) + \mathcal{F}[r_N(E) t_N(E - E_D)](t), \tag{3.11}$$

where $\tilde{t}_N$ and $\tilde{r}_N$ are the transmission and reflection coefficients of the resonance absorber and sample in the time domain for $t > 0$. The first term of Eq. 3.11 reflects the interaction pathway without resonant scattering. Therefore, the temporal response is a delta function, $\delta(t)$, which is the prompt in the measurement. It can be neglected, if only events with delay times bigger than the temporal pulse width of the prompt are counted. The second term reflects the interaction pathway where only the reference absorber resonantly interacts. However, the electronic reflection is strongly suppressed in a waveguide minimum. Therefore, the constant electronic coefficient r_e is very small in relation to the nuclear coefficient r_N. Thus, also the second term of Eq. 3.11 can be neglected and consequently, only the last two terms are contributing at delay times bigger than the temporal prompt pulse width.

The last term of Eq. 3.11 corresponds to the interaction pathway, where the X-ray pulse interacts with sample and reference absorber, and is the most interesting term. If the sample is a thin film cavity excited in a waveguide minimum, the resonance is superradiantly broadened. This will be later discussed in section 6.1. The superradiant broadening means that the resonance linewidth is much bigger than the natural linewidth. The resonance linewidth of the reference absorber, on the other side, is of the order of the natural linewidth. Therefore, the resonance linewidth of the sample is much bigger than the resonance linewidth of the reference absorber. The reflection coefficient can

thus be assumed to be constant over the resonance width of the transmission coefficient, i.e. $r(E)t(E-E_D) \approx r(E_D)t(E-E_D)$. The temporal response of the combined setup is therefore,

$$\tilde{r}_c(t,E_D) \approx t_e\tilde{r}_N(t) + r_N(E_D)\tilde{t}_N(t)e^{iE_Dt/\hbar}. \tag{3.12}$$

If now only events with late delay times are measured, where the temporal response of the sample died out due to the fast superradiant decay in contrast to the slow natural decay of the reference absorber, only the last term of Eq. 3.12 gives a contribution to $\tilde{r}_c$. Then, the measurement of the quantity $I(t_1,t_2,E_D)$, given by [Röh10]

$$I(t_1,t_2,E_D) = \int_{t_1}^{t_2} |\tilde{r}_c(t,E_D)|^2\, dt, \tag{3.13}$$

which is the time integrated intensity from time t_1 to t_2, is proportional to $|r(E_D)|^2$. The time t_1 has to be chosen to be late enough so that the nuclear response of the sample died out. t_2 is limited by the experimental condition, i.e. the temporal separation between two X-ray pulses. Thus, the energy spectrum of the sample can be directly measured with the Mössbauer drive setup in the case of a thin film cavity.

3.5.3. Nuclear Inelastic Scattering

For measurements of the inelastic channel, an APD is placed above the sample. Since the incoherent signal is isotropically distributed, the detector is placed as close as possible to the sample to obtain maximal intensity. A scan of the sample angle ϑ provides an incoherent nuclear reflectivity curve. The maximum signal is obtained when the electric field is maximal at the position of the resonant layer, so for example at the critical angle. Due to the incoherent nature, however, the intensity scales only linearly with the electric field enhancement, instead of quadratically as in the case of coherent scattering. For a fixed incidence angle, the incoherent signal is measured as a function of the incoming beam energy by scanning over an energy range of, e.g. $E_0 \pm 100\,\mathrm{meV}$, relative to the transition energy E_0.

The general idea for the analysis is given in section 2.2.4. In the experiment, the incoming beam energy is described by an energy distribution function around the center energy, which is called the instrumental function. Its width is determined by the high resolution monochromator, which has an energy bandwidth of typically 1 meV. The mea-

sured incoherent signal is therefore given by the incoherent spectrum convoluted with the instrumental function. Most prominently, the effect is visible at the elastic peak. Theoretically, the elastic peak is extremely sharp given by the natural nuclear linewidth. It can be therefore approximated by a delta-function in comparison to the much broader instrumental function. Thus, the convolution of the elastic peak with the instrumental function is equal to the instrumental function.

For the data analysis, the elastic peak has to be removed from the incoherent spectrum. Since the elastic peak is equal to the instrumental function, the simplest solution is to use the instrumental function for the removal procedure. However, it should be noted that the removal procedure is subjective because the relative contribution of inelastic and elastic scattering in the region of the elastic peak is a-priori unknown. Therefore there is no correct solution. Thus, the incoherent scattered intensity in the energy region of the elastic peak, normally below 1 meV or 2 meV, will be strongly influenced by the elastic peak removal procedure. For measuring the instrumental function, the incoherent channel is not recommended, since the spectrum around $E = E_0$ is affected by multi-phonon contributions. Instead, the instrumental function is typically measured in the coherent channel while scanning the energy. In the case of thin films, incoherent and coherent channels can be measured at the same time by placing additional APDs in the reflected beam direction.

After the elastic peak removal, the inelastic spectrum needs to be properly normalized in order to get the inelastic absorption probability $f_{LM}S_{in}$, as given in Eq. 2.17. It was derived by Lipkin that the average energy, which the nuclei absorb, must be equal to the recoil energy of a free atom [Lip60; Lip95]. This relation between the inelastic absorption probability and the recoil energy can be written as [Chu99],

$$\int E f_{LM} S_{in}(E) dE = E_R, \tag{3.14}$$

with E_R being the recoil energy, which for the ^{119}Sn resonance is 2.6 meV. Since the inelastic spectrum is proportional to the inelastic absorption probability, relation 3.14 can be used to correctly normalize the inelastic spectrum. Eq. 3.14 is one out of multiple sum rules derived by Lipkin, where the others connect the inelastic absorption probability to thermodynamic properties such as the mean kinetic energy or the mean force constant.

With the inelastic absorption probability determined, the multi phonon contributions

can be calculated, and finally the phonon density of states. The phonon density of states allows to calculate thermodynamic properties of the resonant materials. A comparison with the thermodynamic properties derived from Lipkin's sum rules is a convenient quality check of the analysis.

The data analysis is conducted by employing the software *PHOENIX* developed by W. Sturhahn [PHO] and *nisdos* developed and provided by I. Sergeev[2].

[2]Deutsches Elektronen-Synchrotron, 22607 Hamburg, Germany

4. Structural properties and hyperfine interactions in thin tin films

Employing thin tin films for probing photon-nuclei interactions requires a detailed knowledge of the structural and nuclear properties of the films. In this chapter, film properties such as smoothness and crystal structure are investigated for tin films, which are prepared by a combination of sputter deposition and vacuum quenching, as explained in section 3.2. The results of X-ray reflectometry and X-ray diffraction measurements are presented and discussed.

With the acquired structural knowledge, nuclear resonance scattering on the tin films are performed and the results are presented with the goal to obtain insight into the nuclear properties of tin films. Thereby, the influence of a magnetic environment on the hyperfine structure of a tin film is probed by an external magnetic field. Additionally, due to the depth sensitivity of nuclear resonance scattering in a grazing incidence setup, the hyperfine structure of the interface to the surrounding material of the tin film is revealed.

4.1. Preparation of smooth tin films

During sputter deposition, tin atoms are forming big clusters on the substrate, when the temperature of the substrate, T_S, is kept at room temperature. In the upper panel of Fig. 4.1(a), the height profile of these clusters is measured by atomic force microscopy. An atomic force microscope scans the surface of a sample with a vibrating tip. Due to forces, such as van der Waals forces in between tip and the sample surface, the vibration frequency changes as a function of distance between tip and surface. Based on this principle, the topology of the surface is revealed. In Fig. 4.1(a), clusters of tin with lateral dimensions of several hundreds of nanometers and heights up to 80 nm are visible. This island formation is reported in the literature [Hou17]. However, the situation changes drastically, if the tin

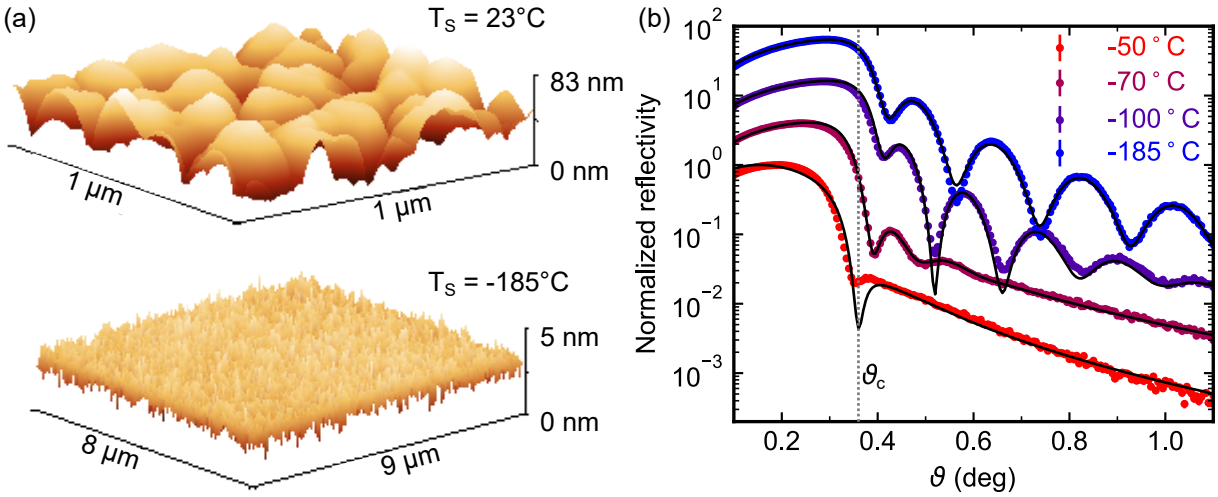

Figure 4.1.: Measurements showing the effect of the substrate temperature during sputtering on the roughness of tin films. (a) Comparison of atomic force microscopy measurements on tin films prepared at room temperature and at −185 °C. (b) X-ray reflectivity measurements of tin films prepared at various substrate temperatures. The critical angle ϑ_c of β-tin is indicated. The graphs are offset by a factor of three to each other.

is sputtered on a cooled substrate. In the lower picture of Fig. 4.1(a), the height profile of a tin film is shown which was prepared by using the same preparation parameters, e.g. same deposition time, but on a substrate cooled down to $T_S = -185\,°\mathrm{C}$. Here, the height profile shows a flat surface over an area of several µm. A rms roughness of 0.7 nm is obtained. The flat surface is a striking difference to the tin film shown in the top part of Fig. 4.1(a).

The change of smoothness can also be seen in the X-ray reflectometry measurements, as shown in Fig. 4.1(b). The growth of the tin film prepared at $T_S = -50\,°\mathrm{C}$ is still dominated by the island formation. The reflectivity shows no pronounced thickness beats, since the clusters suppress any coherent reflections from interfaces which could constructively interfere. Moreover, the critical angle is lower than expected. Using Eq. 3.3 with $f_1 \approx Z = 50$, an X-ray wavelength of 1.54 Å and the expected density of β-Sn of 7.27 g/cm^3, the critical angle should be at $\vartheta_c = 0.36°$, as indicated in Fig. 4.1(b). The lower critical angle, therefore, indicates a lower film density. It is likely a consequence of the cluster formation which leads to a lower average density similar to a sponge. Thus, tin deposited on a substrate at $T_S \geq -50\,°\mathrm{C}$ does not form a compact film. With decreasing substrate temperature, however, the behavior gradually changes. With $T_S = -70\,°\mathrm{C}$, the critical

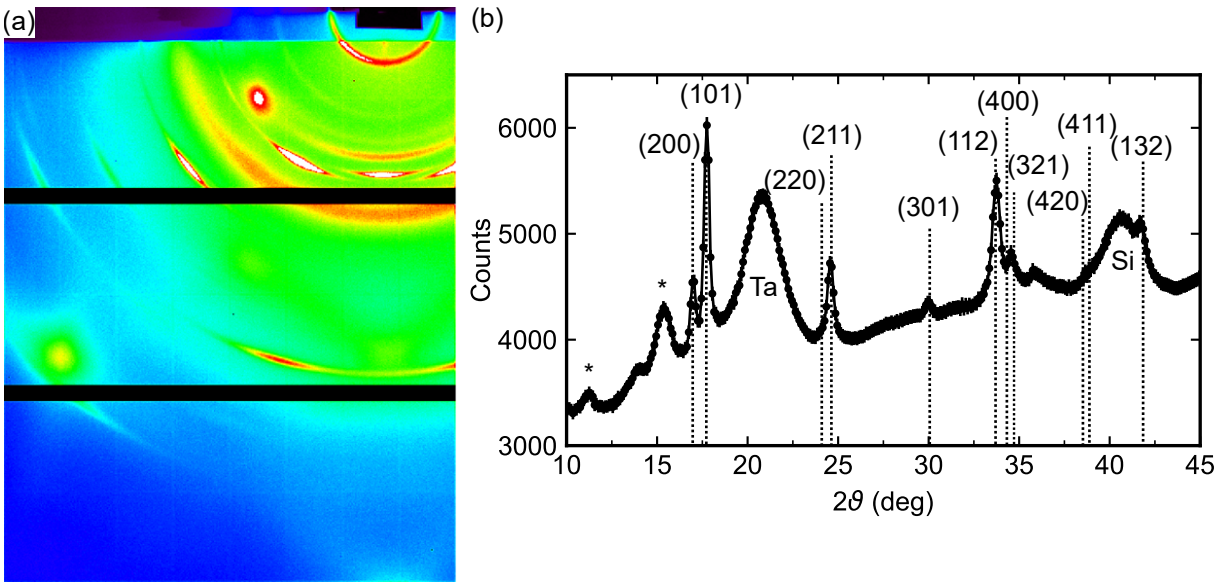

Figure 4.2.: Diffracted intensity of a 20 nm tin film embedded between tantalum prepared on a substrate cooled down to −110 K at a fixed incidence angle of 3°. A 2D *PILATUS* detector counted the diffracted X-ray photons (a) and the resulting count statistic was integrated over the azimuthal angle (b). The X-ray energy was set to 14.41 keV. The theoretical positions of β-Sn Bragg peaks along with the corresponding Miller-indices are indicated. Additionally, Bragg peaks belonging to α-Ta are marked. Peaks, which could not be identified are marked by *.

angle increases and a weak thickness beat pattern appears. For tin films prepared on a substrate at $T_S = -100\,°C$, the critical angle finally matches the expected value and the thickness beat pattern is clearly visible. The fit with the software GenX provides a film density of $7.27\,g/cm^3$ and a roughness of 1.2 nm. The tin film has therefore the same density as β-Sn, but has still an increased roughness. At the lowest possible substrate temperature, $T_S = -185\,°C$, the roughness decreases further to 0.7 nm, which is the same result as obtained from the atomic force microscope measurement. The tin film is 22 nm thick, therefore, the relative roughness is about 3%. This result renders the preparation of more complex layered structures possible which will be used for the nuclear resonance scattering studies.

The results from above confirm that the preparation method leads to smooth tin films. As a next step, the crystal structure is characterized. In Fig. 4.2, a GIWAXS (grazing incidence wide angle X-ray scattering) measurement is shown, conducted at beamline

Table 4.1.: Peak position and the full width at half maximum (FWHM) resulting from the fit of individuals peaks in the XRD measurement shown in Fig 4.2 with a Gaussian function. The crystallite size was calculated by the Scherrer equation.

hkl	2ϑ	FWHM	Crystallite size
(200)	16.99(0)°	0.33(1)°	135(3) Å
(101)	17.74(1)°	0.36(3)°	124(11) Å
(211)	24.58(1)°	0.39(2)°	117(6) Å
(301)	29.99(1)°	0.42(2)°	108(4) Å
(112)	33.74(1)°	0.57(2)°	80(2) Å

P01, *PETRA III*, at an X-ray energy of 14.41 keV. The measurement is performed on a 20 nm tin film prepared on a substrate cooled down to −110 K and embedded between tantalum layers. The incidence angle was fixed at 3° and a 2D *PILATUS* detector was used, which counts the diffracted intensity over a two dimensional space shown in Fig. 4.2(a). Thus, not only the diffracted intensity in the scattering plane is measured, but also along the azimuthal angle. In Fig. 4.2(b), the counts were integrated over the azimuthal angle. The theoretical positions of the Bragg peaks for β-Sn (ICSD[1] Collection Code: 252800), which are indicated with their corresponding Miller indices, match well with the measured peaks. Therefore, the tin crystals in the film are unambiguously in the β tin crystal structure.

For a quantitative description, the peak positions and widths must be extracted. A Gaussian function was used as a fit function for the peak. In Tab. 4.1, the position and the full width at half maximum (FWHM) of the most prominent peaks are given. With the FWHM given, the crystallite size can be calculated by using the Scherrer equation, given in Eq. 3.7. The result for each peak is listed in Tab. 4.1. As a result, the average crystallite size is approximately 12(2) nm. The crystallite size is therefore in the same order as the thickness. This contradicts the prediction of the structure zone model, which is described in the previous chapter 3.2. The low substrate temperature is expected to remove any diffusion energy of the tin atoms on the substrate. Hence, an amorphous structure is predicted. However, since the tin film is heated up to room temperature after preparation, recrystallization processes are possible [Buc52]. These processes could lead to the crystallites, which are visible in the diffraction measurement.

[1]Inorganic Crystal Structures Database [ICS]

A closer look in Tab. 4.1 shows that the calculated crystallite size depends on the angle 2ϑ. This is likely related to that fact, that other contributions to the FWHM, such as internal strain and instrumental broadening, are not included. Since including these effects in the calculation would lead to bigger crystal sizes, the given results must be understood as the lower boundary for the crystallite size. The disentanglement of different effects requires a high-resolution XRD measurement for multiple Bragg peaks, which is not provided here.

In summary, the fabrication process of tin films using cooled substrates leads to the desired growth of smooth tin films, which have the same density and crystal structure as the β-Sn crystal configuration. The amount of lattice defects cannot be derived from the above measurements. However, since the tin films behave like desired, nuclear resonance scattering experiments can be conducted to investigate the hyperfine structure of the tin films.

4.2. Nuclear resonance scattering on tin films

As a starting point, a 20 nm tin film in the natural isotopic composition is investigated by nuclear resonance scattering of synchrotron radiation. Therefore, about 8.6% of the tin nuclei are ^{119}Sn. The film is embedded between two tantalum layers. The structure was investigated in the grazing incidence geometry at the critical angle, which is at about $\vartheta_c = 0.12°$ at the X-ray energy of 23.88 keV. The temporal decay after excitation is shown in Fig. 4.3(a). The linear behavior in the logarithmic scale shows that the decay is nearly exponential. This corresponds to a single nuclear transitions, which means that almost no hyperfine interactions are present. The temporal decay was modeled with a 18.6(2) nm natural enriched tin film without any hyperfine splittings as shown in Fig. 4.3(a). The thickness was confirmed by reflectivity measurements. The lack of a quadrupole splitting is unexpected for an assumed β-Sn film, since bulk β-Sn has a quadrupole splitting of 0.28 mm/s. When comparing the quadrupole splittings of common tin compounds and crystal configurations, see Tab. 2.1, only α-Sn has no quadrupole splitting. However, since the X-ray reflectometry and X-ray diffraction measurements show only β-Sn-like properties, such as density and crystal configuration, α-Sn can be excluded. Since the quadrupole interaction is sensitive to tiny crystal variations, the tin crystals seem to slightly differ from the β configuration.

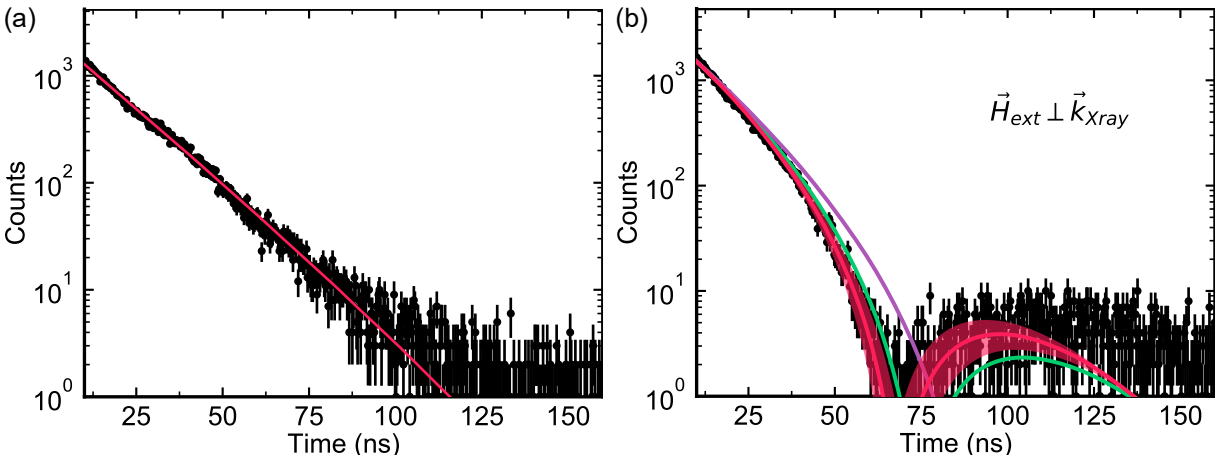

Figure 4.3.: (a) Temporal nuclear decay of a 20 nm tin film with natural isotopic composition embedded in tantalum. The fit is shown red. (b) The same temporal decay with an additional external magnetic field of about 275(25) mT applied. The fit is shown in red together with an error of ±20 mT. Additionally, simulated temporal decays in a 250 mT (green) and 200 mT (violet) magnetic field are shown.

To probe the sensitivity of the tin films to magnetic environments, a magnetic field of about 275(25) mT is applied to the film by a permanent magnet. The orientation of the field is in the film plane and perpendicular to the X-ray pulse direction. The temporal decay is shown in Fig. 4.3(b). A quantum beat at about 70 ns appears in the decay. The magnetic field causes the hyperfine structure to split and the resulting total of six possible dipole transitions results in a beat pattern in the temporal decay. In small magnetic fields, the difference in transition frequencies is so small, that the decay pattern only shows one effective beat. This is especially true for ^{119}Sn. The magnetic splitting of an energy state is proportional to the g-factor, which is the ratio between the magnetic moment and the angular momentum. For ^{119}Sn nuclei, the g-factor of the ground state is five times higher than of the excited state. Thus, in small magnetic fields, only the splitting of the ground state into a doublet has a considerable impact on the temporal decay pattern.

The fit of the decay pattern yields a magnetic hyperfine field of 279(2) mT, which is equal to the applied external magnetic field within the error bars. This leads to two conclusions. Firstly, since metallic tin is paramagnetic, it can be concluded that the paramagnetic contribution to the magnetic hyperfine field is smaller than the error of the measurement, if present at all. A paramagnetic contribution arises from the spin polarization of conduction electrons and the resulting polarization of s-type electrons,

which have a finite probability density to be inside the nucleus.

The second conclusion is that the tin film can probe magnetic field strengths of about 250 mT or higher. Simulated nuclear decays in a 250 mT field and in a 200 mT field are shown in Fig. 4.3(b) as well. The beat pattern in the 250 mT magnetic field is still clearly visible. In the 200 mT field however, the beat is not resolvable anymore. An increase in the measurement time by a factor of four would be required to clearly measure the beat pattern. Thus, the tin film can resolve about 250 mT magnetic fields within reasonable measurement times (<2h). Even though this magnetic field was externally applied, the same principle holds for internal magnetic fields via spin polarization, for example.

The fit procedure of the beat pattern results in an error of 2 mT of the magnetic field strength. By only looking at clear visual changes in the quantum beat, the error bar is about 20 mT, as indicated in Fig. 4.3(b). This gives valuable parameters to probe magnetic environments. The magnetic environment should produce a magnetic hyperfine field at the tin nuclei of ≥ 250 mT or it should impact an existing magnetic hyperfine field by at least ± 20 mT. These are valuable parameters for future experiments as will be discussed in section 7.

In Fig. 4.3(a), a small deviation from the exponential decay is visible which were not further discussed so far. It indicates that a different tin compound is present, which might be related to the interface to the tantalum layers. To investigate the interface effect, a thinner tin layer with a thickness of 7 nm was prepared, which was again embedded in tantalum. To enhance the signal, an isotopically enriched ^{119}Sn sputter target was used with an enrichment of 97%. The nuclear resonance scattering experiment was set up in the same way as for the previous tin film. The temporal decay of this thin tin layer is shown in Fig. 4.4(a). As a comparison, the temporal decay of the 20 nm tin film is shown in gray. The first observation is that the temporal decay is faster for the thin film than for the thicker film. This is caused by the enrichment of ^{119}Sn nuclei, which leads to an increased effective thickness and therefore to a speed up effect. A second observation is that the slight deviation from the exponential decay in the thick tin layer are more pronounced in the thin film. The quantum beats do not fit with common tin structures or compounds, such as oxides. To get more insight into the hyperfine structure in the thin tin film, conversion electron Mössbauer spectroscopy (CEMS) was additionally conducted on the same structure by V. Raghavendra Reddy[2]. The measurement is shown in Fig.

[2]UGC-DAE Consortium for Scientific Research, Indore, India

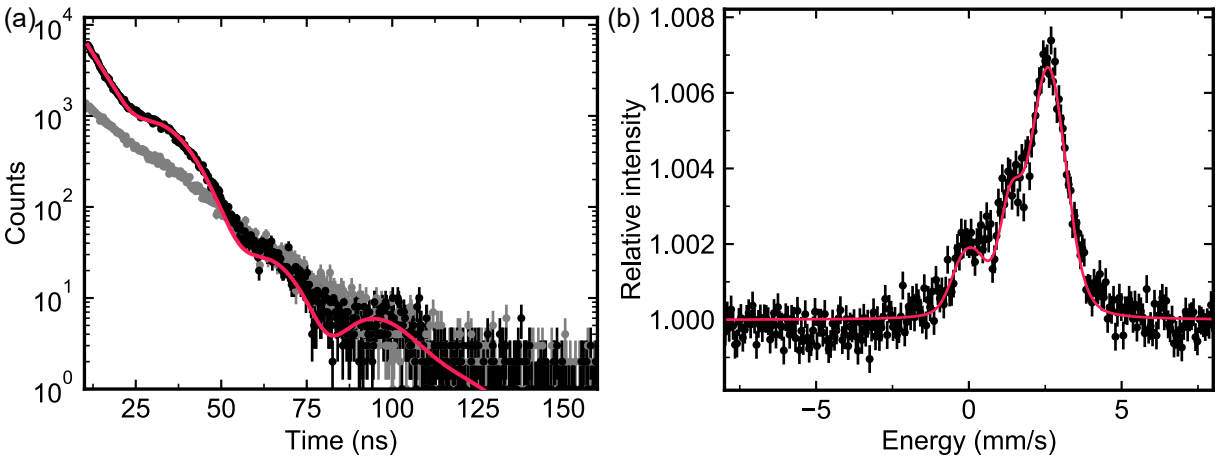

Figure 4.4.: (a) Temporal decay pattern of a 7 nm tin film embedded in tantalum (black) in a comparison to the temporal decay of a 20 nm tin film (gray). (b) Conversion electron Mössbauer spectroscopy measurement on the same 7 nm tin film. Depicted is the intensity relative to the background away from resonance versus the Mössbauer drive velocity. For energy conversion: 1 mm/s ≙ 79.6 neV. Red curves in both graphs represent the fit using CONUSS.

4.4(b). The fit using the software CONUSS reveals that in addition to β-Sn with its isomer shift around 2.6 mm/s and a smaller SnO_2 contribution at 0.0 mm/s, another tin compound is present with an isomer shift of around 1.3 mm/s. The fit results are shown in Tab. 4.2. This isomer shift does not belong to a common tin crystal phase or tin oxide and is likely related to the interface to the tantalum layers.

However, the CEMS measurement has no information how the hyperfine structure is distributed within the tin layer. This information is given by the temporal decay pattern in Fig. 4.4(a) since it was obtained at grazing incidence. To fit the decay, the results of the CEMS measurement were used and resonant interface layers are added between tin and tantalum. While the center layer is assumed to be β-Sn, the interface layers contain all information of the unknown tin compound. Since the total thickness of the tin layer is known by X-ray reflectometry, only the relative thicknesses of interface to center layer is fitted to match the measured temporal decay. The fit result is given in Tab. 4.3 and the fitted temporal decay is plotted in Fig. 4.4(a). With an interface layer thickness of 8 Å, the temporal decay pattern can be well reproduced. Thus, about 1 nm at each interface is strongly affected by the adjacent tantalum. The negative isomer shift relative to β-Sn means that the probability of electrons being inside the nucleus, thus s-type electrons, is

Table 4.2.: Fit parameters of the CEMS spectrum shown in Fig.4.4(b). Values without an error are fixed during the fit procedure and, if possible, taken from Tab. 2.1

Parameter	Fit result
Weight β-Sn	65(2)%
Isomer shift	2.60(5) mm/s
Quadrupole splitting	0.23 mm/s
Weight Ta-Sn	18(2)%
Isomer shift	1.35(10) mm/s
Quadrupole splitting	0.0 mm/s
Weight SnO_2	17(2)%
Isomer shift	0.0 mm/s
Quadrupole splitting	0.57 mm/s

Table 4.3.: Fit parameters of the temporal decay pattern shown in Fig.4.4(a). Values without an error are fixed during the fit procedure and, if possible, taken from Tab. 2.1

Parameter	Fit result
Thickness center layer	5.3(1) nm
Isomer shift	2.60(5) mm/s
Quadrupole splitting	0.23 mm/s
Thickness interface layer	0.8(1) nm
Weight Ta-Sn	73(3)%
Isomer shift	1.35(10) mm/s
Quadrupole splitting	0.0 mm/s
Weight SnO_2	27(3)%
Isomer shift	0.0 mm/s
Quadrupole splitting	0.57 mm/s

smaller in the tin-tantalum compound than in β-Sn. The contact to tantalum therefore seems to lead to a rearrangement of the electronic structure of tin and/or a charge transfer of the 5s valence electrons of tin to tantalum. Electronic configuration calculations in combination with these results could resolve the chemical state of the interface layer.

In conclusion, the nuclear resonance scattering experiment shows that the center part of the tin film inside tantalum behaves like β-Sn, but at the interface, the electronic configuration changes. This interface effect might also pave a way to engineer the vibrational behavior of embedded thin tin films.

Moreover, with the absolute (250 mT) and relative ($\pm$20 mT) detection limit for magnetic hyperfine fields in tin films found, a closer look into the detection of spin structures employing thin tin films can be taken. The discussion in the following aims to answer the question which conditions need to be fulfilled in order to render the detection of spin polarizations in tin films possible. Thereby, the spin polarization can be either static or time dependent in form of a spin current.

4.3. Probing spin currents with tin films

An obvious case study for tin films is to probe its magnetic environment due to its paramagnetic property. Indeed, multiple studies on tin probing magnetic properties have been conducted. They were mainly focused on tin atoms being diluted in magnetic materials [Huf70], magnetic tin compounds [Gor94] or tin as a probe for external magnetic fields [Tro16]. The question which immediately arises is, if tin films can be used to probe magnetic structures, especially nanostructures, to investigate also time dependent phenomena such as spin currents. In combination with using different isotopic layers, such as ^{118}Sn and ^{119}Sn, the spin currents could also be measured spatially resolved.

Due to a spin current, or spin polarization, a spin bias $\Delta\mu$ is built up in tin measured as the energy difference between the electronic density of states for the two different spin directions. The spin bias can then impact the hyperfine structure of tin. Since the electron shell of tin has no total angular momentum or spin, the only possible source for a magnetic hyperfine field is the Fermi contact field contribution. It is given by [All76]

$$B_{cont} = -\frac{2}{3}\mu_0\mu_B \cdot \sum_{ns} \left(|\psi_{ns}(0,\uparrow)| - |\psi_{ns}(0,\downarrow)|\right), \tag{4.1}$$

with $\mu_0 = 1.257 \times 10^{-6}\,\mathrm{T\,m/A}$ being the vacuum permeability and $\mu_B = 9.274 \times 10^{-24}\,\mathrm{A\,m^2}$ the Bohr magneton. The sum term describes the spin polarization at the position of the nucleus summed over all s-shells, since only those have a non-zero probability density of being inside the nucleus. $|\psi_{ns}(0,\uparrow)|$ and $|\psi_{ns}(0,\downarrow)|$ are the probability density per unit volume m^{-3} of the s-electron with the main quantum number n and spin $\uparrow$ and $\downarrow$ at the position of the nucleus, $r = 0$. In general, the interaction between different electrons inside the electron shell is complex and needs to be numerically calculated, e.g. via density functional theory.

In the following, an estimation of the contact field is provided. A splitting $\Delta\mu$ of the spin density of states leads to a spin polarization per unit volume of,

$$\left(\left\langle n_\uparrow \right\rangle_t - \left\langle n_\downarrow \right\rangle_t\right) = \Delta\mu g(E_F), \tag{4.2}$$

assuming that the spin density of states for both spin direction can be described by the same function $g(E)$ and $\Delta\mu \ll E_F$ (e.g. for β-Sn: $E_F = 10.2\,\mathrm{eV}$ [Lid06] and $\Delta\mu \propto 10^{-5}\,\mathrm{eV}$). Furthermore, for a paramagnet, the magnetization M in an external magnetic field $\mu_0 H$ is given by $M = \chi H$, with the magnetic susceptibility χ. But the magnetization is also given via the spin polarization per unit volume by

$$\langle M \rangle_t = \mu_B \cdot \left(\left\langle n_\uparrow \right\rangle_t - \left\langle n_\downarrow \right\rangle_t\right) \tag{4.3}$$

$$\overset{4.2}{=} \mu_B \cdot \Delta\mu g(E_F). \tag{4.4}$$

The spin splitting $\Delta\mu$ can be expressed by a magnetic field $B = \mu_0 H$ and by using the relation of a magnetic dipole interaction with a magnetic dipole moment μ: $\Delta\mu = \mu \cdot B$, where the sign was dropped, since only differences in energy are important. In a paramagnet, which has no total angular momentum or total spin, only the delocalized conduction electrons carry a magnetic moment, which is equal to $\mu = \mu_B$. These paramagnets are called Pauli paramagnets. Thus, $\Delta\mu$ is equal to $\Delta\mu = \mu_B \cdot B = \mu_B \mu_0 H$. Inserting this expression into Eq. 4.4 yields,

$$\langle M \rangle_t = \mu_B^2 g(E_F) \mu_0 \cdot H \tag{4.5}$$

$$=: \chi_P H, \tag{4.6}$$

with $\chi_P = \mu_0 \mu_B^2 g(E_F)$ called Pauli susceptibility. This result connects the spin density of states, $g(E_F)$, with the magnetic susceptibility, which can be found in tables for various materials, if the material can be described as a Pauli paramagnet. This is the case for β-Sn. With this relation found, the spin polarization of the valence electrons can be expressed by,

$$\left(\left\langle n_\uparrow \right\rangle_t - \left\langle n_\downarrow \right\rangle_t\right) = \frac{\chi_P}{\mu_0 \mu_B^2} \Delta\mu. \tag{4.7}$$

The spin polarization is given per unit volume m^{-3}. For the following discussion, the spin polarization must be given per nucleus. Thus, equation 4.7 must be divided by the number density ρ_n.

In order to calculate the contact field contribution, the probability density of the spin polarized electrons to be inside the nucleus has to be found. The isomer shift in Mössbauer studies depends on a similar probability density, the contact density, which is the total probability density of all atomic electrons to be inside the nucleus. Mössbauer experiments and numerical studies were conducted in the past to calculate this contact density ρ_c. Osadebe *et al.* [Osa87] calculated the contact density of the core electrons of tin, meaning of the $4\mathrm{d}^{10}$ electron configuration, and the total contact density of β-Sn. For the discussed spin polarization case, the approximation that only the valence electrons are spin polarized can be made. This neglects any spin polarization of core electrons for simplicity. With this assumption, the difference of the total contact density of β-Sn, $\rho_c(\beta - \mathrm{Sn})$, and of the core electrons, $\rho_c(4d^{10})$ provides the important contact density of only the valence electrons: $\rho_c(\mathrm{val}) = \rho_c(\beta - \mathrm{Sn}) - \rho_c(4d^{10}) = 184053.0\, a_0^{-3} - 183993.63\, a_0^{-3} = 59.37\, a_0^{-3}$, with the Bohr radius $a_0 = 5.292 \times 10^{-11}\,\mathrm{m}$. The values are taken from Osadebe *et al.* [Osa87]. With the spin polarization given in equation 4.7, the contact field can now finally be written as

$$B_{cont} = -\frac{2}{3}\mu_0 \mu_B \cdot \left(\left(\left\langle n_\uparrow \right\rangle_t - \left\langle n_\downarrow \right\rangle_t\right) \rho_c\right) \tag{4.8}$$

$$= -\frac{2}{3}\frac{\chi_P}{\mu_B \rho_n} \Delta\mu \cdot \rho_c(\mathrm{val}). \tag{4.9}$$

Thus, the magnetic hyperfine field can be estimated for a given spin splitting $\Delta\mu$.

A spin splitting can be generated, e.g. by spin pumping. When a ferromagnet/non-magnetic metal bilayer, such as iron/tin, is resonantly excited at the ferromagnetic resonance, a spin current flows into the non-magnet. This phenomenon is called spin pumping. Depending on the material properties of the non-magnetic material, the spin current can

travel through the material or a spin polarization is build up on the interface.

Due to spin pumping, a spin bias $\Delta\mu$ is built up in the non-magnet measured. It is given by [Bra02]

$$\Delta\mu = \left(\left\langle n_\uparrow \right\rangle_t - \left\langle n_\downarrow \right\rangle_t\right)/g(E_F), \tag{4.10}$$

The maximum spin bias, which can be built up, is equal to the ferromagnetic resonance energy $\hbar\omega_F = hf_F$ [Bra02]. With typical ferromagnetic resonance frequencies in the low GHz regime, the maximum spin bias is typically on the order of 10 µeV.

Using Eq. 4.9 with the magnetic susceptibility of $\chi_P \simeq \chi = 2.4 \times 10^{-6}$ and the atomic number density $\rho_n = 3.685 \times 10^{28}\,\mathrm{m}^{-3}$ for β-Sn, a spin splitting of 10 µeV leads to a Fermi contact field of $\simeq 3\,\mathrm{mT}$. This field is below the absolute and relative measurement limit of the nuclear resonance scattering method, as derived from the experiments in chapter 4. Therefore, a magnetic hyperfine field or a shift of the magnetic hyperfine field due to spin pumping in tin cannot be measured in the discussed geometry.

It needs to be taken into account that only the valence electrons at the Fermi energy are actually spin polarized. For β-Sn, the electrons at the Fermi level are mostly of p-type character, which have a zero contact density. Therefore, the actual contact field will be smaller. Not taken into account as well is the polarization of core electrons. This polarization contribution depends heavily on the exact electronic configuration and cannot be easily determined. However, it affects the contact field by factor in the regime of $0.5 - 2$ [Fre65]. Therefore, the above obtained result should be a good estimation for the magnitude of the magnetic hyperfine field generated via spin pumping.

The result from above can be compared with the Knight shift measured in nuclear magnetic resonance measurements. In the nuclear magnetic resonance experiments, a static magnetic field is applied to a sample and the resonance frequency of a certain isotope, e.g. ^{119}Sn, is probed, thus, the ground state splitting of the hyperfine structure in the external magnetic field. In paramagnetic metals, the magnetic hyperfine field at the nucleus can be different to the external field due to the above described spin polarization of the atomic electrons. The Knight shift is defined as the shift in the magnetic hyperfine field for a metal relative to the hyperfine field shift in an insulator. Thus, it probes the effect of the spin polarization of the conduction electrons. For β-Sn, a Knight shift of about 0.76% was found [Blo53].

To compare this with the result from above, the spin splitting $\Delta\mu$ can be expressed

by a hypothetical external field by $\Delta\mu = \mu_B \mu_0 H_{ext}$. With $\Delta\mu = 10\,\mu\text{eV}$, an external field of $\mu_0 H_{ext} \simeq 170\,\text{mT}$ is obtained. Using the Knight shift of [Blo53] *et al.*, the shift of the magnetic hyperfine field is therefore $0.76\% \cdot 170\,\text{mT} \simeq 1\,\text{mT}$. It is thus of the same order of magnitude as the above calculated contact field. Thus, the Knight shift is a good estimation for the expected hyperfine field due to a spin polarization, at least for a Pauli paramagnet such as tin.

The discussion above shows, that the expected hyperfine field generated by spin pumping is about three orders of magnitude to small to be measured, assuming a lower absolute measurement limit of 250 mT for nuclear resonance scattering derived from the tin film experiments. In order to measure a spin polarization, either the sensitivity of the material must be enhanced, meaning a higher Knight shift, or the spin splitting must be increased. The first option is only limited possible, because typical Knight shift values are in the region of 1%. Therefore, the only realistic possibility is to increase the spin polarization. Spin polarization due to spin pumping is limited by the ferromagnetic resonance frequency $\Delta\mu \leq h f_F$. This resonance frequency f_F is determined by the magnetic properties of the material, however, typically about a few GHz.

Another possibility would be to directly inject a spin polarized current into the tin by applying a voltage between the ferromagnet and the non-magnet. This effect was measured with a copper film in contact with cobalt, where a current density j produced a spin splitting in the copper of [Kuk15]

$$\Delta\mu = \frac{2(2\alpha_F - 1) l_{sf}^N \rho_e^N e j}{1 + 4\alpha_F(1-\alpha_F)\frac{l_{sf}^N \rho_e^N}{l_{sf}^F \rho_e^F}}, \tag{4.11}$$

with the spin asymmetry parameter of the ferromagnetic material α_F, the spin diffusion length in the non-magnet/ferromagnet l_{sf}^N / l_{sf}^F, the electrical resistivity of the non-magnet/ferromagnet, ρ_e^N / ρ_e^F and the elementary charge $e = 1.602 \times 10^{-19}\,\text{C}$. Following the work of [Kuk15] *et al.*, in the case of the ferromagnetic cobalt the parameters are: $\alpha_F = 0.8$, $l_{sf}^F = 38\,\text{nm}$ and $\rho_e^F = 210\,\Omega\,\text{nm}$. β-Sn has an electric resistivity of $\rho_e^N = 115\,\Omega\,\text{nm}$. The spin diffusion length is not known, but preliminary ferromagnetic resonance measurements give a rough estimate of $l_{sf}^N \approx 100(50)\,\text{nm}$. Thus, a typical current density of $j = 1 \times 10^{11}\,\text{A/m}^2$ results in a spin splitting of about $\Delta\mu \simeq 0.7\,\text{meV}$. Using again Eq. 4.9, a Fermi contact field of 210 mT would be generated. This field is on the

same order as the lower measurement limit of 250 mT for nuclear resonance scattering on thin tin films. Thus, the directly injected spin current could be measured via nuclear resonance scattering.

The discussion shows, that even though the detection of spin currents generated by spin pumping might not be possible in tin films, spin currents in general can be very well measured by tin films if the produced spin splitting is big enough. A point which was not discussed yet, is that the tin film forms interface layers with its adjacent material. With the exact electronic configuration at the interfaces being a-priori difficult to calculate, the exact hyperfine field shift is hard to predict. Therefore, multiple ferromagnet/tin bilayer systems need to be studied to find the best combination. The combination of permalloy and tin, however, seems promising considering that in this system the Lamb-Mössbauer factor is drastically increased, which renders the measurement of the spin current in ultrathin tin films possible. Thus, the spin current can be probed spatially resolved.

5. Lattice dynamics of embedded thin tin films

Interfaces in thin film structures have become important especially since the scaling down of technical applications, such as electrical devices, to the nanometer scale. Due to a high percentage of atoms being located at an interface, properties of thin films are strongly influenced by the interface region. The effect of interfaces on the hyperfine structure was already measured in the previous chapter for tin films embedded in tantalum. Here, the interface to tantalum seemed to lead to a rearrangement of the electronic structure of the tin atoms, which resulted in an altered isomer shift.

The results of the tantalum-tin layers raise the question, if also a magnetic influence can be measured in the paramagnetic tin layer if the embedding material is magnetic. A possible "magnetic proximity effect" [Man14] plays an important role, if spin currents inside the tin layer are aimed to be detected. To investigate the magnetic proximity effect, a 3 nm tin layer is prepared in between two 10 nm permalloy films as schematically shown in Fig. 5.1(a). Permalloy is a ferromagnetic nickel-iron alloy, $Fe_{20}Ni_{80}$, with a relatively strong saturation magnetization [Krü07]. Since permalloy films deposited by magnetron sputtering are polycrystalline with each crystallite exhibiting only a weak magnetocrystalline anisotropy [Yin06], thin permalloy films have no net magnetocrystalline anisotropy and are therefore considered as soft magnetic. This renders the material attractive for magnetic nanostructures, e.g. for spin pumping applications [Mos10].

The temporal nuclear decay at three different incident angles is shown in Fig. 5.1(b). The incident angles are tuned to the waveguide mode of the layer structure, slightly detuned from the waveguide mode and to the critical angle. The fit of the nuclear decay by the software CONUSS provides a quadrupole splitting of 1.12(5) mm/s. The hyperfine structure will be discussed in more detail in the next section. More importantly, however, a fit of the nuclear decay is only successful, if the Lamb-Mössbauer factor of the tin

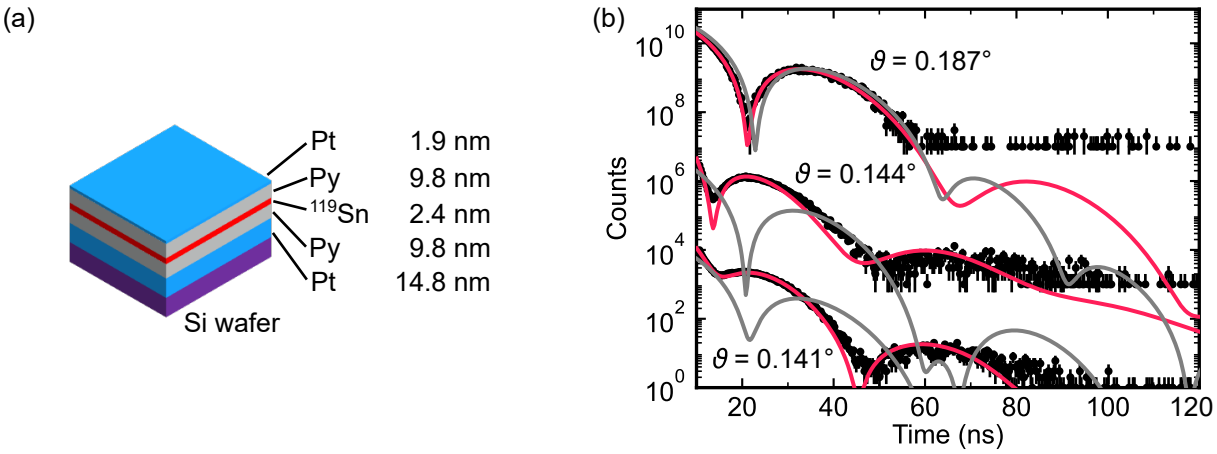

Figure 5.1.: (a) Schematic of the permalloy-tin layer structure with thicknesses provided from reflectivity measurements. (b) Temporal nuclear decay of the embedded tin layer at three different angles: Inside the waveguide mode of the layer system (0.141°), slightly detuned from the waveguide mode (0.144°) and at the critical angle (0.187°). The decay was fitted with an assumed Lamb-Mössbauer factor of 0.04 (gray) and of 0.28 (red).

film is drastically increased: From 0.04 to 0.28. This can be seen by comparing the temporal decay in the waveguide mode and at the critical angle. The beat pattern shifts to earlier times when the incidence angle is tuned to the waveguide mode. This indicates a dynamical beat feature in the temporal decay. However, if simulated with the Lamb Mössbauer factor of bulk β-Sn of 0.04, as plotted in Fig. 5.1(b) (gray), no dynamical beat should occur in this sample. Thus, the effective thickness of the tin layer must be higher than expected. Since the thickness of the tin layer is confirmed by reflectivity measurements, only an enhancement of the Lamb-Mössbauer can reproduce this behavior. The fit with an increased Lamb-Mössbauer factor of 0.28 is shown in Fig. 5.1(b) (red).

While the magnetic proximity effect seems to be absent in the permalloy-tin layer system, the increased Lamb-Mössbauer factor of the thin tin layer indicates that the tin layer becomes "harder" inside permalloy. This result sparked an investigation of the thermodynamic properties of embedded thin tin films with the goal to engineer the vibrational properties to increase the Lamb-Mössbauer factor in the tin films.

In the following, systems containing tin films embedded in different materials are investigated by nuclear inelastic scattering. The aim is to probe the dynamical behavior of the tin films. Two parameters are looked at in more detail: The tin layer thickness and the embedding material. At first, the embedding material is kept constant and the tin

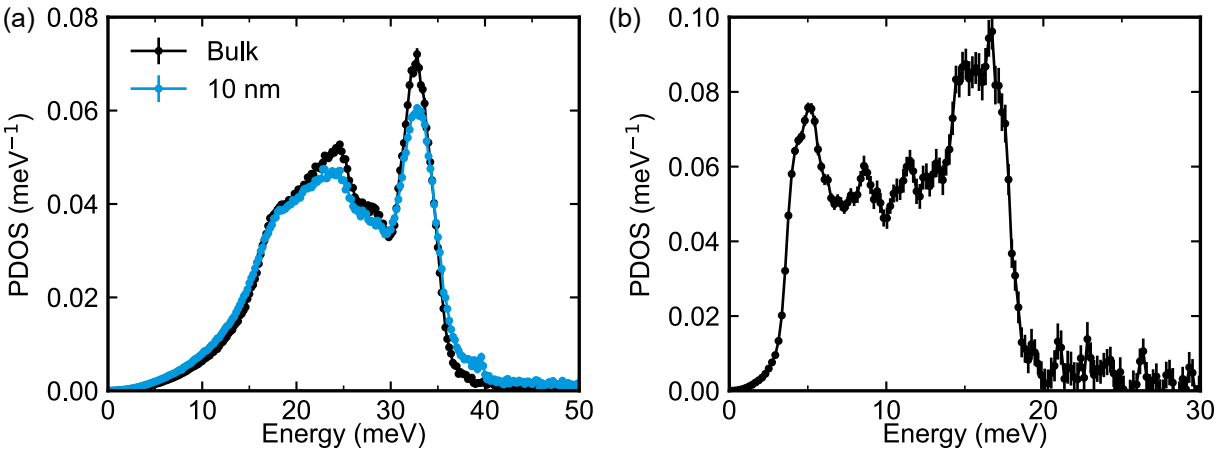

Figure 5.2.: (a) Phonon density of states (PDOS) of permalloy. The partial PDOS of the ^{57}Fe nuclei was measured in a bulk permalloy metal (black) and in a 10 nm permalloy film capped by tantalum to prevent oxidation (blue). (b) PDOS of ^{119}Sn in the β tin crystal structure.

layer thickness is varied. For the thickness dependency study, the permalloy-tin system is employed since a high effect strength was already measured. Secondly, the tin layer is kept at a thickness of 2 nm, while the adjacent material was varied, namely gold, tantalum, chromium, titanium, iron and boron carbide. The results of all system are then discussed.

5.1. Tin embedded in permalloy

Permalloy has the benefit to contain iron and therefore nuclear resonance experiments are possible by using the ^{57}Fe resonance as well. For example, nuclear resonance scattering experiments revealed that the iron in permalloy has a strongly split hyperfine structure due to a magnetic hyperfine field of about 28 T [Boc15]. By nuclear inelastic scattering, the phonon density of states (PDOS) of the ^{57}Fe nuclei inside of permalloy can be measured. Measurements were conducted at P01 at *PETRA III* (Hamburg) at room temperature. The resulting phonon density of states of iron in bulk permalloy is shown in Fig. 5.2(a). Even though only the partial iron phonon density of states is accessible, it closely follows the total phonon density of states of permalloy due to the chemical similarity between iron and nickel [Luc13]. Phonon states of up to $\approx$ 38 meV are visible. The distinct phonon peak at 33 meV is a "van Hove singularity" [VH53]. A van Hove singularity occurs where the

phonon dispersion relation $\omega(k)$ is flat since here are many phonon modes within a small energy interval. A flat dispersion occurs typically at the zone boundaries of the Brillouin zone. The phonon density of states was also measured in a 10 nm permalloy film, which was capped by tantalum to prevent oxidation. This density of states is shown in Fig. 5.2(a) as well. Generally, the phonon density of states of the thin film follows the bulk density of states. A damping of the phonon modes is visible by a general broadening of the features and an increase of low and high energy phonon modes. This is typical for thin films, e.g. shown by Röhlsberger *et al.* [Röh99], and is related to an increased scattering rate of the phonons at interfaces and grain boundaries. The increased scattering rate leads to a decreased phonon lifetime and hence to broader energy features. Additional effects such as phonon confinement in thin films can also play a minor role in the shown phonon density of states. Phonon confinement occurs, when the adjacent material has a drastically different phonon density of states, which leads to a suppression of certain phonon modes in the thin film, since they cannot propagate in the adjacent material.

Tin, on the other hand, has no phonons above 18 meV. The phonon density of states of bulk β-Sn is shown in Fig. 5.2(b). The measurement was taken also at *PETRA III* on a β-Sn foil at 110 K by courtesy of Ilya Sergeev. The phonon density of states has a cut-off energy at about 18 meV. It also shows two van Hove singularities for the acoustical phonons around 5 meV and optical phonons at 15 meV. Optical phonons are present due to the two-atomic base of the tetragonal β-Sn lattice, however, without a gap, since the two atoms are chemically identical. The phonon modes in β-Sn are at much lower energies compared to iron, because the force constants are weaker in comparison to permalloy or iron. The softness correlates with smaller elastic constants. For example, the bulk modulus of β-Sn is about 58 GPa [Na10] while α-Fe has a bulk modulus of 170 GPa [Ada06]. β-Sn is therefore much softer.

5.1.1. Diluted tin in permalloy

In the permalloy-tin system the tin layer thickness is varied to investigate the effect of the interface. Since tin is a much heavier atom than iron or nickel, it cannot be expected that a infinitely thin tin layer vibrates in the same way as the surrounding atoms in permalloy. To know the maximum effect permalloy can have on tin atoms, the lowest possible thickness, which is equal to diluted tin atoms inside permalloy, is measured at

first. Such a sample was prepared in the following way: A 110 nm permalloy film was prepared and every time when 10 nm of permalloy material was sputtered, ^{119}Sn was co-sputtered with a nominal thickness of 0.1 nm. The procedure was repeated ten times followed by a capping of 10 nm permalloy and a thin layer of tantalum. In total, 1 nm of ^{119}Sn was distributed in 110 nm permalloy, which makes an average dilution of 0.1 vol. % tin in permalloy.

The nuclear inelastic scattering experiment was conducted at beamline 30-ID at the *APS* at room temperature. The resulting phonon density of states of diluted ^{119}Sn in permalloy is shown in Fig. 5.3(a). The spectrum has a broad peak at around 15 meV and a lesser pronounced plateau in the region around 30 meV. Phonon modes until 40 meV are visible. When comparing the obtained phonon density of states to the spectrum of β-Sn, not much similarity is recognizable. On the contrary, the tin atoms vibrate with energies similar to those of permalloy, with a cut-off energy equal to the one in permalloy. Still, the phonon density of states is also not directly comparable to the density of states of permalloy. It is related to the fact that tin atoms are much heavier than iron or nickel and the force-constant between tin and iron/nickel atoms might be different to the force constant between atoms in permalloy.

The question of how impurities vibrate inside a host matrix led to the development of multiple models [Gro78]. One of the most successful models was developed by Mannheim *et al.* [Man68; Man71; Man72] for cubic systems. The model assumes that a host atom is substituted with an impurity atom. Thereby, the model considers only nearest-neighbor central forces and pure harmonic lattice interactions. It was applied to a number of vibrational studies in diluted systems, e.g. [Set00; Luc08; Del15]. Based on the phonon density of states of the host matrix $g_h(\omega)$, the mass ratio of host to impurity atom, m_h/m_i and the ratio of the force constants between host-host atoms and host-impurity atoms, A_{h-h}/A_{h-i}, the phonon density of states of the impurity atom g_i can be modeled by [Set00]

$$g_i(\omega) = \frac{m_h}{m_i}\left(\frac{g_h(\omega)}{\left(1+\rho(\omega)S(\omega)\right)^2+\left((\pi/2)\,\omega\rho(\omega)g_h(\omega)\right)^2} + \frac{\delta(\omega-\omega_L)}{\rho(\omega)^2T(\omega)+m_h/m_i-\left(1+\rho(\omega)\right)^2}\right), \tag{5.1}$$

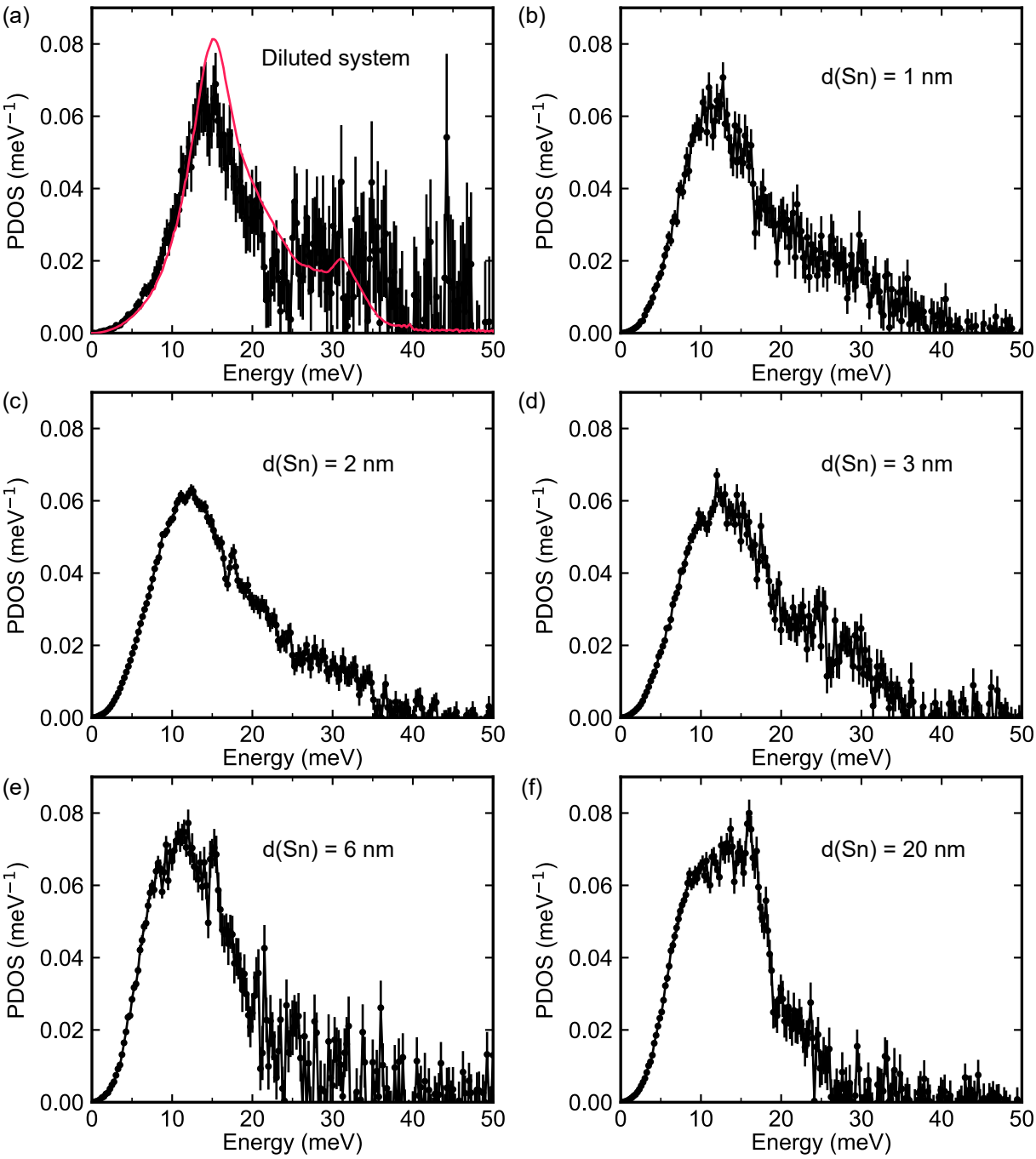

Figure 5.3.: Phonon density of states (PDOS) of tin inside permalloy for (a) a diluted system with an estimated 0.1 vol.% tin and (b-f) for a tin layer of varying thickness d(Sn) embedded between two 10 nm permalloy layers. The diluted system was fitted by the impurity model of Mannheim *et al.* [Man71] with a force constant ratio $A_{h-h}/A_{h-i} = 0.84$.

where,

$$\rho(\omega) = \frac{m_h}{m_i} - 1 + \frac{\omega^2 (1 - A_{h-h}/A_{h-i})}{\mu(2)}, \tag{5.2}$$

$$S(\omega) = \mathcal{P} \int_0^\infty \frac{\omega'^2 g_h(\omega')}{\omega'^2 - \omega^2} d\omega', \tag{5.3}$$

$$T(\omega) = \omega^4 \int_0^\infty \frac{g_h(\omega')}{\omega'^2 - \omega} d\omega', \text{ and} \tag{5.4}$$

$$\mu(n) = \int_0^\infty \omega^n g_h(\omega) d\omega. \tag{5.5}$$

$\mathcal{P}$ denotes the principal value of the integral. Localized modes at the frequency ω_L can appear, if the frequency satisfy $1 + \rho(\omega_L) S(\omega_L) = 0$ and $\omega_L > \omega_{\max}$, with $\hbar\omega_{\max}$ describing the cut-off energy of the phonon density of states of the host material. The localized modes are modeled by a Dirac δ-function here, however, in reality the modes should be broadened by finite phonon lifetimes.

The impurity model was applied to the phonon density of states of the diluted tin-permalloy system. The spectrum of the 10 nm permalloy film was used as the phonon density of states of the host matrix, since it should come close to the vibrational spectrum which the tin atoms experience. Because the mass ratio is known, only the force constant ratio is used as a free parameter to find the best possible fit between model and experiment. The result is shown in Fig. 5.3(a) with the force constant ratio $A_{h-h}/A_{h-i} = 0.84$. The impurity model describes the experimental result well. First, it describes the low-energy phonon part, meaning the suppression of the β-Sn low-energy phonons. Second, it predicts the high-energy phonons and the cut-off energy. Therefore, the vibrational properties of the tin atoms are mostly determined by the permalloy host matrix. Some deviations are visible in the energy part below the β-Sn cut-off energy of 18 meV. It indicates, that the tin atoms are not completely diluted inside the host matrix but also tin clusters are likely present which might be a result from the preparation procedure. The result shows that in the limiting case of an ultrathin tin layer in permalloy the vibrational properties of tin are dictated by the adjacent material.

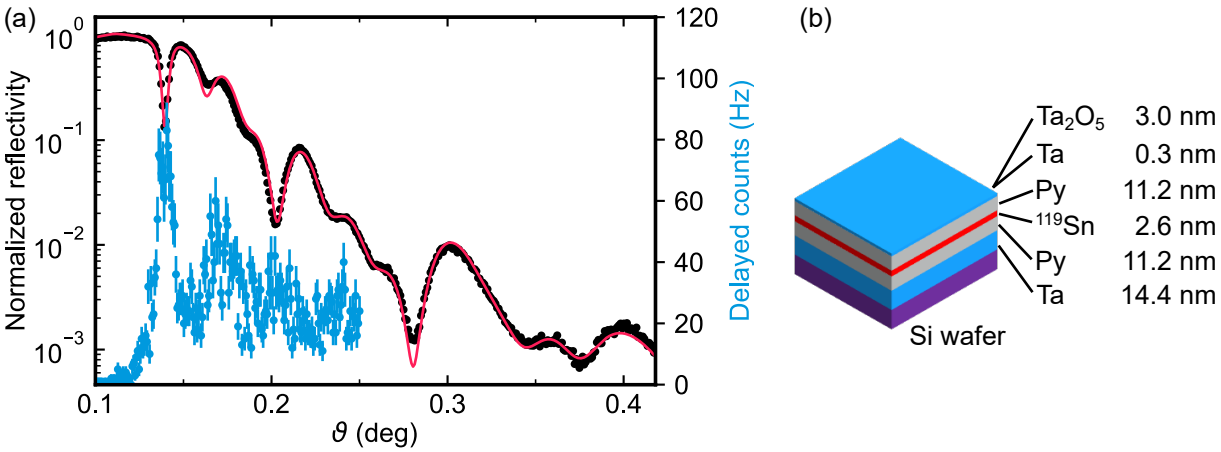

Figure 5.4.: (a) Normalized electronic reflectivity (in logarithmic scale, red) and reflectivity of the delayed nuclear inelastic signal (in linear scale, blue) of the layered permalloy-tin system. Fit of the electronic reflectivity is plotted in black (GenX software). (b) Schematic of the layer structure with thicknesses provided by the fit of the electronic reflectivity of (a).

5.1.2. Thickness dependent NIS study

To investigate the role of the interfaces for the vibrational properties, a series of samples with different tin thicknesses embedded between two 10 nm permalloy layers were prepared. A 15 nm seed tantalum layer and a tantalum capping layer with a thickness varying from 1 nm to 3 nm were used. The tantalum layers provide a cavity-like structure which enhances the inelastic signal as discussed in section 3.4.

The electronic reflectivity together with the delayed nuclear inelastic signal of a nominal 3 nm thick tin layer inside permalloy is shown in Fig. 5.4(a). In the electronic reflectivity, the waveguide minimum at 0.14° is clearly visible. Since here the X-ray pulse couples into the waveguide structure, the wavefield is strongly enhanced in the center of the layered structure, thus, at the position of the enriched tin layer. Therefore, also the inelastic signal is increased. The fit of the electronic reflectivity by the software GenX provides a tin layer thickness of 2.6 nm, which is slightly less than which was aimed for. A schematic of the layered structure together with the results of the reflectivity fit is provided in Fig. 5.4(b).

For all systems, the inelastic spectrum is measured at the incidence angle with the highest delayed nuclear inelastic signal, which is typically at the angle where the radiation

couples into the first-order waveguide mode. Besides an increase in signal, the waveguide mode has the benefit that the X-ray wavefield is centered inside the tin layer. Therefore, both tin-permalloy interfaces contribute equally to the scattered signal. Only for the thickest tin layer of 20 nm, the critical angle provides a higher signal. Here, the waveguide structure becomes ineffective due to the high photoabsorption of tin. From the measured inelastic spectrum, the phonon density of states can be derived. The resulting phonon density of states of all systems are shown in Fig. 5.3 with the tin layer thicknesses: (b) 1 nm, (c) 2 nm, (d) 3 nm, (e) 6 nm and (f) 20 nm.

For thin tin layers, meaning < 6 nm, the phonon density of states resembles that of the diluted system. A broad peak exists around 15 meV and a plateau in the region around 30 meV. The cut-off energy is about 37 meV to 40 meV. The described features are clearer in these systems, since the drastically increased tin amount relative to the diluted system leads to much better statistics in shorter measurement time. The findings are surprising, since at these thicknesses, the tin atoms cannot be described as impurities anymore. The presence of a continuous layer of tin between the two permalloy layers is confirmed by the fit of the electronic reflectivity, as shown previously in Fig. 5.4(a). However, the measured vibrational properties are still more resembling the impurity system than a tin system.

In the 6 nm sample, a shift to lower energies is visible with high energy modes only extending up to 30 meV. The broad peak shifts down to energies around 11 meV. Around 18 meV the density of states drops significantly. At 15 meV a peak is visible, which resembles the van Hove singularity of the optical phonons of β-Sn. All these features indicate that the tin layer gets softer and that some β-Sn-like crystal grains are present.

The trend gets more clearer in the case of the 20 nm tin layer. The drop at 18 meV is sharper and the broad peak forms a plateau from 10 meV to 17 meV. Above the β-Sn cut-off is still a significant amount of phonon modes with energies up to 28 meV. It reflects the fact that still about 15% of the tin nuclei are in an interface region, assuming an interface thickness of 1.5 nm. However, even with the consideration of the interface contribution, the low-energy part of the phonon density of states lacks the typical low-energy phonons of β-Sn around 5 meV. It indicates that the tin crystal structure in the layer differs significantly from the β crystal phase.

From the phonon density of states, a number of thermodynamic parameters can be calculated by Eqs. 2.21 and the Lamb-Mössbauer factor by Eq. 2.11. In Tab. 5.1 the

Table 5.1.: Lamb-Mössbauer factor, f_{LM}, inner energy, U, mean force constant F and vibrational entropy, S_{vib}, derived from the phonon density of states for embedded tin in permalloy with varying tin layer thickness d. The diluted system is given by the nominal tin layer thickness of 1 Å. Also given are the parameters for a β-Sn foil and a 10 nm ^{57}Py layer with the latter being measured at the ^{57}Fe resonance. As a comparison, literature values for bulk β-Sn [Bar00] and for β-Sn clusters with a crystallite size of 35(9) nm [Hou17] are given. The force constant is given per atomic mass unit, which is in the case of ^{119}Sn equal to 119 and for ^{57}Fe 57.

d (nm)	f_{LM} @ 296 K	U @ 0 K (meV)	F ($\mathrm{Nm^{-1}amu^{-1}}$)	S_{vib} @ 35 K($3k_B$)
0.1	0.52(1)	26(2)	1.5(1)	0.05(1)
1	0.33(1)	26.9(5)	1.47(4)	0.10(1)
2	0.28(1)	24.9(3)	1.28(3)	0.11(1)
3	0.28(1)	24.1(5)	1.18(4)	0.11(1)
6	0.19(1)	21.4(7)	0.92(6)	0.16(1)
20	0.21(1)	21.1(5)	0.85(4)	0.15(1)
β-Sn	0.420(3) (@110 K)	18.2(3)	0.66(2)	0.22(1)
10 nm Py	0.75(1)	39.9(1)	2.86(1)	0.02(1)
[Bar00]	0.042(6) (@296 K)	-	-	-
[Hou17]	0.66(2) (@35 K)	-	0.55(5)	0.24(1)

derived thermodynamical parameters of all measured tin-permalloy systems are listed together with the results from bulk β-Sn and from iron in a 10 nm permalloy film. The diluted system is labeled with its nominal tin layer thickness of 0.1 nm. While the Lamb-Mössbauer factor and the entropy are more sensitive to low energy phonons, the inner energy and especially the force constants are strongly affected by the high-energy part, where also the error of the derived phonon density of states is the highest. Therefore, a cut-off energy of 40 meV was imposed on the derivations, since neither tin nor permalloy have phonon modes above this energy. The inner energy is given for 0 K, because at this temperature, the contribution of the high energy modes to the inner energy is the least due to the Bose-Einstein statistics, see Eqs. 2.21. The entropy is also given at a low temperature of 35 K, firstly, to reduce the weight of the high-energy modes as well and secondly so that it can directly be compared to the measurements on tin nanoclusters by Houben *et al.* [Hou17]. The results of Houben *et al.* are given in Tab. 5.1 for their smallest tin nanoclusters where the tin crystallites have a size of 35(9) nm [Hou17]. The

Lamb-Mössbauer factor at room temperature for bulk β-Sn is taken from Barla *et al.* [Bar00]. The derived Lamb-Mössbauer factor of the measured β-Sn foil cannot be easily extrapolated to room temperature since metallic tin has a considerable degree of anharmonicity and therefore, the phonon density of states of β-Sn changes with temperature [Bar00].

The derived thermodynamic parameters for the diluted system are drastically different from bulk tin. Most prominent is the Lamb-Mössbauer factor, which is more than a factor of 12 higher than bulk tin. The hardening is also visible by the increased mean force constant. The reason becomes clear, when comparing the values to the much harder permalloy reflected in a high Lamb-Mössbauer factor, a high inner energy and a higher mean force constant. From the derived force constants, a force constant ratio of iron and nickel atoms inside permalloy and of tin atoms inside the permalloy matrix can be calculated by $A_{h-h}/A_{h-i} = 2.86(1)/1.5(1) \cdot 57/119 = 0.91(6)$. It agrees well with the force constant ratio predicted by the impurity model applied directly on the phonon density of states, which provided a force constant ratio of 0.84. Thus, the result confirms that the vibrational properties of the tin atoms can solely be described by the permalloy matrix with only considering the differences in masses and force constants.

The 1 nm tin film is also much harder than bulk tin. The Lamb-Mössbauer factor is increased by a factor of eight. Although the phonon density of states looked similar to the diluted system, the thermodynamic parameters differ in some aspects. Parameters which depend more on low-energy phonons, such as Lamb-Mössbauer factor or vibrational entropy, differ more substantially, while the force constant and the inner energy, which depend stronger on high-energy phonons, are nearly the same within the error bars. Since clustering of tin will likely lead to the formation of metallic tin and therefore to an increase in low energy phonons, see phonon density of states of β-Sn in Fig. 5.2(b), the parameters suggest that there is a certain amount of tin clusters.

The trend to a softer lattice is increased in the 2 nm and 3 nm tin films. Here, also the force constant and inner energy differ stronger from the diluted system. However, the Lamb-Mössbauer factor is still increased relative to bulk tin by a factor of seven. Therefore, the thermodynamic properties of the tin films are mainly dictated by the adjacent permalloy up to a layer thickness of 3 nm.

From 6 nm on, the tin layer is substantially softer than the diluted system. The impact of the interface seems to be decreased. Especially the high-energy part gets closer to

bulk tin, which can be seen from the force constant. The mean force constant in the 20 nm tin film is already close to the bulk film. Quantities which are sensitive to the low-energy phonons, however, still differ significantly from bulk β-Sn as already noticed from the phonon density of states. The inner energy is still increased by 16% and the Lamb-Mössbauer factor by a factor of more than five. It is unlikely that the deviations of the thermodynamic quantities from the values of bulk β-Sn are caused by the interface, since 20 nm tin corresponds to more than 40 atomic tin layers. These deviations are more likely to be linked to the crystalline structure of the tin layer. This will be discussed later.

5.1.3. Structural characterization of the interface region

The results indicate that the thermodynamic properties of thin tin films can be tuned by the interface up to a layer thickness of 3 nm. To get more insight into the origin, conversion electron Mössbauer spectroscopy (CEMS), X-ray diffraction (XRD) and nuclear resonance scattering are conducted. In Fig. 5.5 XRD, CEMS and nuclear resonance scattering measurements are shown for the 3 nm tin film inside permalloy. The XRD pattern exhibits no diffraction peaks from the tin layer, but only from tantalum and permalloy. This is not surprising since in such a thin film, the crystallite sizes are expected to be limited by the layer thickness. Thus, if any tin crystallites are present, the small size will lead to strongly broadened diffraction peaks. The diffraction peaks of the surrounding materials are therefore likely to eclipse any possible diffraction peaks from the tin layer.

The CEMS spectrum, however, gives valuable information about the hyperfine structure of the tin layer. The spectrum features a strong peak which appears to be split and a lesser contribution around 0 mm/s. Therefore, the fit of the spectrum is based on the assumption that two tin compounds are present: SnO_2 and an unknown compound with a quadrupole splitting. The fitted spectrum is plotted in Fig. 5.5(b). Based on the fit, the unknown compound has an isomer shift of 2.16(1) mm/s and a quadrupole splitting of 1.12(5) mm/s. SnO_2 contributes with a spectral weight of 13 % to the spectrum.

The splitting of the unknown compound can also be modeled with a small magnetic hyperfine field, which might be present due to the previously discussed magnetic proximity effect. The energy resolution of the CEMS measurement is not high enough to differentiate between a small magnetic splitting or a small quadrupole splitting.

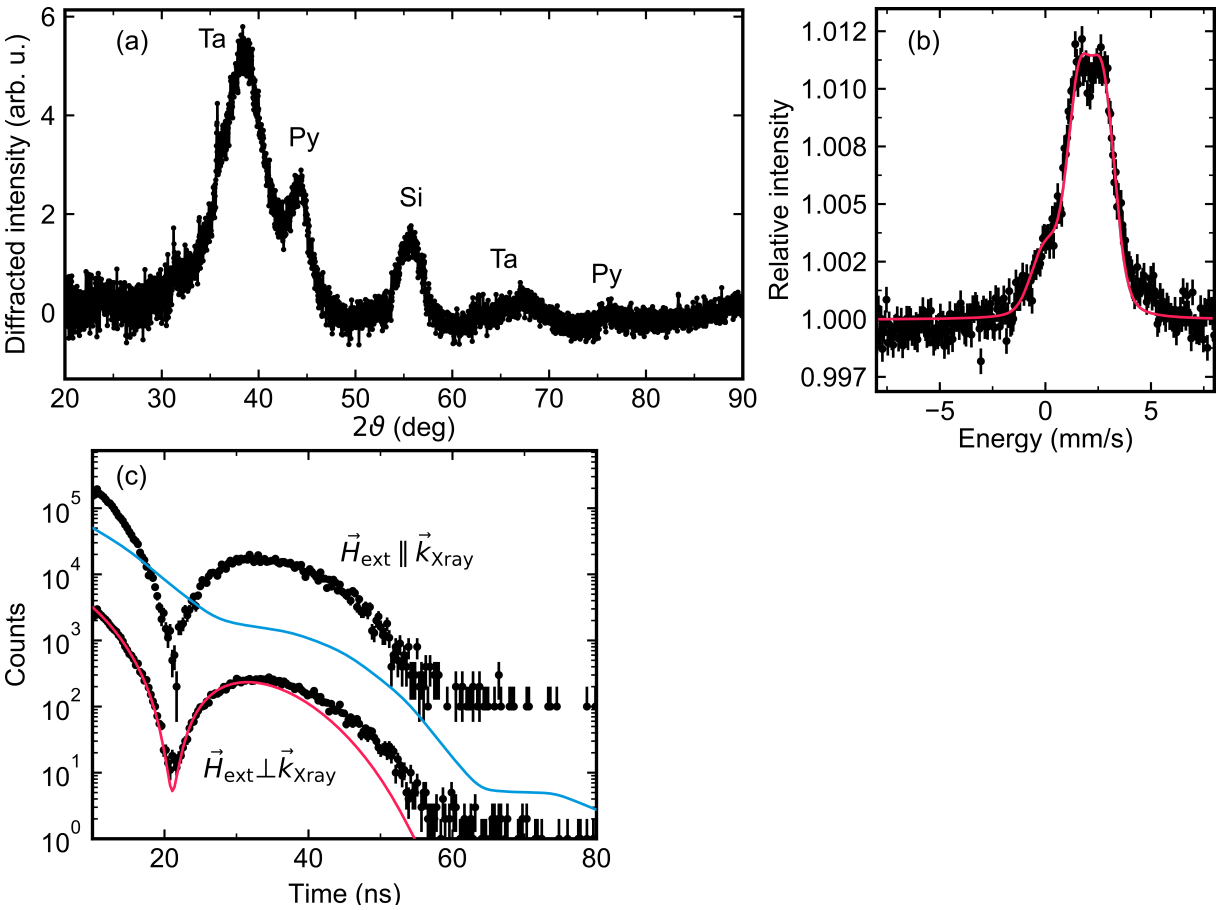

Figure 5.5.: (a) X-ray diffraction measurement on the 3 nm tin film embedded in permalloy. Diffraction peaks are assigned to the crystal structure of α-Ta and β-Ta, as well as of Ni_3Fe, the crystal structure of permalloy. (b) Conversion electron Mössbauer spectroscopy measurement. The energy scale is relative to the isomer shift to SnO_2 and for energy conversion: 1 mm/s $\widehat{=}$ 79.6 neV. (c) Nuclear resonance scattering results. An external in-plane magnetic field $\vec{H}_{ext}$ was applied parallel and perpendicular to the X-ray direction, $\vec{k}_{Xray}$. The temporal decay are offset by a factor of 100. While the measurements show no dependency, the simulations (red/blue) differ drastically.

In the time domain, however, the dependence of the decay pattern on the magnetic hyperfine field orientation can be used to clarify the origin of the splitting. To influence the orientation, an external magnetic field is used, which is strong enough to align the magnetization of the permalloy layer and thus of the potential magnetic hyperfine field. In the nuclear resonance scattering experiment, a 100 mT external field was used, which is aligned in the plane of the layers.

In Fig. 5.5(c), the temporal nuclear decay is shown for a parallel and a perpendicular magnetic field orientation relative to the X-ray direction. Both temporal decays are identical and thus, the temporal decay is independent on the magnetic field orientation. In contrast, when simulating the case of a magnetic hyperfine field, the decay patterns change drastically, when the orientation of the hyperfine field is varied. The temporal decay therefore shows unambiguously that the splitting of the unknown compound is not magnetic but due to the presence of an electric field gradient. Therefore, there is no magnetic proximity effect.

The presence of a tin compound at the interface could mean that an intermetallic phase between tin and iron and/or nickel was formed in the deposition process. Indeed, the phase diagram of iron and tin possesses two intermetallic phases, FeSn and $FeSn_2$, which are stable at room temperature [Kum96]. But not only with iron, also with nickel, tin forms stable intermetallic phases at room temperature such as Ni_3Sn, Ni_3Sn_2 and Ni_3Sn_4 [Nas85]. There are no intermetallic phases containing all three elements. However, if an intermetallic phase of two of the elements is formed, e.g. iron and tin, the missing third element, e.g. nickel, is able to form a solid solution with the other intermetallic compound [Hua16].

Some of the nickel-tin/iron-tin intermetallic phases are paramagnetic and feature a similar isomer shift and quadrupole splitting as the tin film inside permalloy. The hyperfine parameters of theses intermetallic compounds are shown in Tab. 5.2. While there is no clear match, the similarity between the literature and experimental hyperfine parameters strongly suggest that the unknown compound is an intermetallic compound. The isomer shift increases towards the β-Sn value of 2.56 mm/s with increasing tin amount. Therefore, the measured 2.16 mm/s isomer shift indicates an intermetallic compound with a high tin fraction. The hyperfine parameters of the amorphous Sn-Ni-Fe alloys are within the same region as the one measured. Therefore, it can be concluded that the interface of the tin-permalloy system consists of an amorphous Sn-Fe-Ni alloy.

5.1.4. ^{57}Fe on tin

Since permalloy contains iron, the tin-permalloy interface can also be investigated by using the ^{57}Fe resonance. Thus, the vibrational properties of the "other side" of the interface can be probed. Since vibrational properties of permalloy are reasonable close to

Table 5.2.: Hyperfine parameters of paramagnetic Fe-Sn, Ni-Sn and Sn-Ni-Fe intermetallic phases. The Sn-Ni-Fe compounds are all amorphous. For FeSn, only the paramagnetic contribution is given, however, a magnetically split tin site is typically present as well [Häg75]. The isomer shift is given relative to SnO_2.

Compound	Isomer shift (mm/s)	Quadrupole splitting (mm/s)	Reference
FeSn	1.87	1.60	[Häg75]
$FeSn_2$	2.18	0.89	[Cha13]
Ni_3Sn	1.50	0.15	[Nai06]
Ni_3Sn_2	1.78	1.18	[Eli73]
Ni_3Sn_4	1.97	0.93	[Mil98]
Sn-Ni-Fe	2.35	1.13	[Szi10]
	2.14	0.85	[Szi12]
	1.75	1.03	[Szi12]
	2.0(1)	1.18	[Lak13]
This work	2.16(1)	1.12(5)	

α-Fe, in the following a simple iron-tin interface is probed. This has the benefit to obtain the direct phonon density of states of the interface on the iron side, in contrast to only a partial density of state in the case of permalloy.

A nominal 0.3 nm ^{57}Fe layer was prepared on a 10 nm tin layer and capped with 8 nm iron which was depleted of ^{57}Fe and tantalum to prevent oxidation. Using a different isotopically enriched iron has the advantage to be sensitive to the first monolayer of iron at the interface only, since a monolayer of iron has a nominal thickness of about 3 Å. The system was prepared as the previous tin samples, thus, on a cooled substrate. As reference, a 10 nm ^{57}Fe layer was measured which was prepared also on a cooled substrate. The resulting phonon densities of states are shown in Fig. 5.6, where the phonon density of states of the 10 nm iron layer is shown in gray.

The reference sample has pronounced peaks at 22 meV, 27 meV and 34 meV, which are typically for α-Fe [Sta07]. Together with a cut-off energy of 38 meV the spectrum has similar characteristics as permalloy as shown in Fig. 5.2(a). The interface phonon density of states of iron looks drastically different. Besides a pronounced, broad peak around 24 meV, there are several smaller features at 4 meV, 10 meV, 15 meV and 34 meV. In contrast to the tin phonon density of states, the iron spectrum cannot be explained within an impurity model. The impurity model by Mannheim *et al.* only predicts phonon

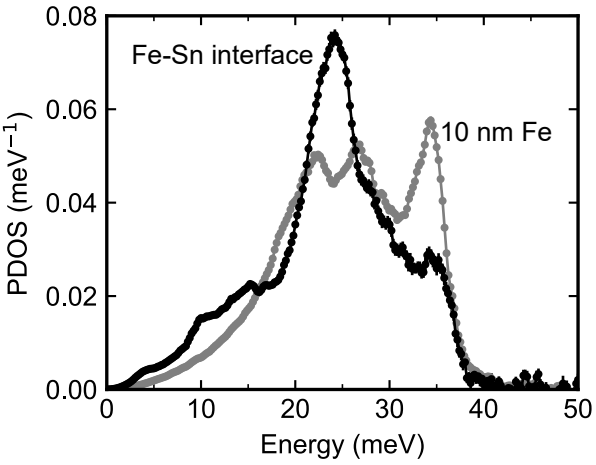

Figure 5.6.: Phonon density of states (PDOS) of a nominal 3 Å thick ^{57}Fe layer on top of 10 nm tin and capped with a 8 nm iron layer, which was depleted of ^{57}Fe (red). A reference phonon density of states of a 10 nm ^{57}Fe layer is shown in gray.

modes up to the cut-off energy of the host matrix, except for some distinct local modes. Most of the iron phonon modes, however, lie above the cut-off energy of β-Sn, which is at 18 meV.

The thermodynamic parameters derived from the reference iron layer and the iron-tin interface system are listed in Tab. 5.3. In contrast to the hardening of the tin layers, the iron gets softer at the interface. The mean force constant is reduced by 12 % relative to the reference iron layer. Although a softening of iron at the interface can be expected, the drastic deviation of the phonon density of states from the reference sample is untypical for iron at interfaces. For example, Keune *et al.* [Keu18] measured the interface between iron and silver. Although silver has similar low-energy phonon modes like tin, the measured phonon density of states of iron is only slightly shifted to lower energies. An

Table 5.3.: Lamb-Mössbauer factor, f_{LM}, inner energy, U, mean force constant F and vibrational entropy, S_{vib}, derived from the phonon density of states for the Fe-Sn interface and the 10 nm iron layer. The force constant is given per atomic mass unit, which is in the case of ^{57}Fe equal to 57.

	f_{LM} @ 296 K	U @ 0 K (meV)	F (Nm^{-1}amu^{-1})	S_{vib} @ 35 K($3k_B$)
Fe-Sn interface	0.66(1)	35.3(3)	2.31(4)	0.03(1)
10 nm Fe	0.76(1)	37.6(1)	2.62(2)	0.02(1)

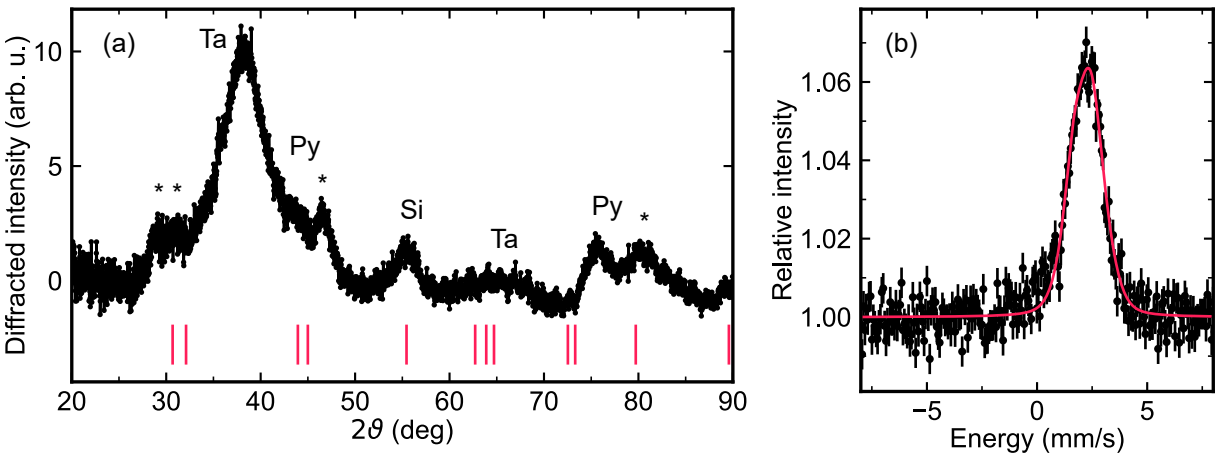

Figure 5.7.: (a) X-ray diffraction measurement on 20 nm tin film embedded in permalloy. Diffraction peaks are assigned to the crystal structure of α-Ta and β-Ta, as well as of Ni_3Fe, the underlying crystal structure of permalloy. Unassigned peaks are marked by an asterisk. Theoretical diffraction peak positions of β-Sn are indicated in red (ICSD Collection Code: 252800 [ICS]). (b) Conversion electron Mössbauer spectroscopy measurement. The energy scale is relative to the isomer shift of SnO_2 and for energy conversion: 1 mm/s $\widehat{=}$ 79.6 neV.

important difference to the iron-tin interface is that the iron-silver phase diagram possesses no intermetallic compounds [Swa84]. Thus, there is less thermodynamic pressure at the silver-iron interface for interlayer mixing.

The combined results of the measurements at the ^{119}Sn resonance and at the ^{57}Fe resonance strongly indicates that the interface of the tin-permalloy system consists of an intermetallic compound. This intermetallic compound is presumably the reason why the tin layer becomes harder. The effect is visible up to a tin layer thickness of 3 nm. For thicker layers, the softer tin behavior starts to dominate, presumable originating from tin atoms in the center of the layer.

Even though an increase in softness is measurable in the thicker tin layers, the thermodynamic behavior of the 20 nm tin layer still differs from the expected β-Sn behavior. For example, the Lamb-Mössbauer factor is increased by a factor of five relative to β-Sn. Therefore, additional XRD and CEMS measurements were conducted at this higher thickness. The results are shown in Fig. 5.7. In contrast to the previously presented tin-tantalum system, see Fig. 4.2, the XRD pattern in Fig. 5.7(a) exhibits no diffraction peaks at the theoretical positions of the β-Sn structure, as indicated in the figure. How-

ever, there are diffraction peaks, marked by an asterisk, which have a similar pattern as β-Sn, especially the double-peak feature around 30°. The peaks could not been assigned to any tin crystal structure, as well as to any tin oxide or intermetallic compound with iron or nickel. Also a scaling of the lattice constants of β-Sn did not reproduce the peak positions. The origin is therefore not known, but due to the similarity to the β-Sn diffraction peak pattern, a strongly distorted β-Sn crystal lattice might be present. Also the CEMS spectrum lacks a β-Sn contribution at 2.56 mm/s, while instead a tin compound with an isomer shift of around 2.2 mm/s is visible. The spectrum in Fig. 5.7(b) was fitted with two tin compounds: The interface compound with the parameters as previously derived, see Tab. 5.2 and an unknown compound. With the parameters of the interface compound fixed, for the unknown component an isomer shift of 2.22(2) mm/s and no quadrupole splitting was obtained by the fit using the software CONUSS. The spectral weight of the unknown compound is 94.3(4)%. Since these values do not match with any nickel-tin or iron-tin intermetallic compound, see Tab. 5.2, and it seems unlikely that the whole 20 nm tin layer formed one intermetallic compound layer with permalloy, the same conclusion as from the XRD measurement can be drawn: The tin layer appears to be in a highly disturbed crystalline structure. Moreover, the measured phonon density of states of the 20 nm tin film embedded in permalloy exhibits β-Sn like features, e.g. the cut-off energy, and strong deviations in the low-energy phonon regime, e.g. the missing van-Hove singularity at 5 meV. The lack of low energy phonons might be related to a small crystallite size which imposes a maximum phonon wavelength, assuming that phonons cannot propagate beyond a grain border.

The growth of small and strongly disturbed tin crystallites are common in layers prepared at cryogenic temperatures [Buc52]. At the moment of deposition, the tin crystal structure is expected to be amorphous and recrystallizes when the sample is brought to room temperature. The recrystallization process of the tin layer is sensitive to the roughness of the substrate and potential impurities [Buc52]. Therefore, it is reasonable to assume that the tin layer recrystallizes when embedded in the nanocrystalline tantalum, as seen in the previous chapter, while the recrystallization is suppressed in the polycrystalline permalloy. However, the presented results do not allow an unambiguous identification of the origin.

Table 5.4.: Lamb-Mössbauer factor, f_{LM}, inner energy, U, mean force constant F and vibrational entropy, S_{vib}, derived from the phonon density of states for embedded tin in varying materials. The force constant is given per atomic mass unit, which is in the case of ^{119}Sn equal to 119 and for ^{57}Fe 57.

Material	f_{LM} @ 296 K	U @ 0 K (meV)	F ($\mathrm{Nm^{-1}amu^{-1}}$)	S_{vib} @ 35 K($3k_B$)
B_4C	0.10(1)	18.7(5)	0.66(3)	0.21(1)
Au	0.12(1)	21.1(5)	0.82(3)	0.17(1)
Cr	0.13(2)	20(2)	1.0(2)	0.16(1)
Ta	0.14(1)	22.7(6)	0.94(4)	0.16(1)
Ti	0.18(1)	22.3(5)	0.95(4)	0.16(1)
Fe	0.24(1)	22.0(6)	1.04(5)	0.12(1)
Py	0.28(1)	24.9(3)	1.28(3)	0.11(1)

5.2. Variation of the embedding material

The results from tin films embedded in permalloy show that the thermodynamic behavior of thin tin films are influenced by the interfaces to permalloy up to a tin layer thickness of about 3 nm. In the following, the thermodynamic properties of the surrounding material will be varied in order to evaluate if the vibrational behavior of thin tin layers can be changed on purpose.

For this study, 2 nm tin layers are embedded inside materials, which cover a broad range of thermodynamic properties. These trilayers are themselves sandwiched between two tantalum layers. The chosen materials are boron carbide, gold, chromium, tantalum, titanium and iron. The measured tin phonon density of states for each system is shown in Fig. 5.8. The derived thermodynamic parameters are listed in Tab. 5.4. In the following, each system will be described in more detail.

Tin in boron carbide

In contrast to all other materials, boron carbide (B_4C) is not a metal but a semiconductor, where the atoms are covalently bonded. As typical for carbide systems, boron carbide is extremely hard. For example, its bulk modulus is 247 GPa [Liu20], which is the highest value of all investigated materials. The hardness is also reflected in its phonon density of states.

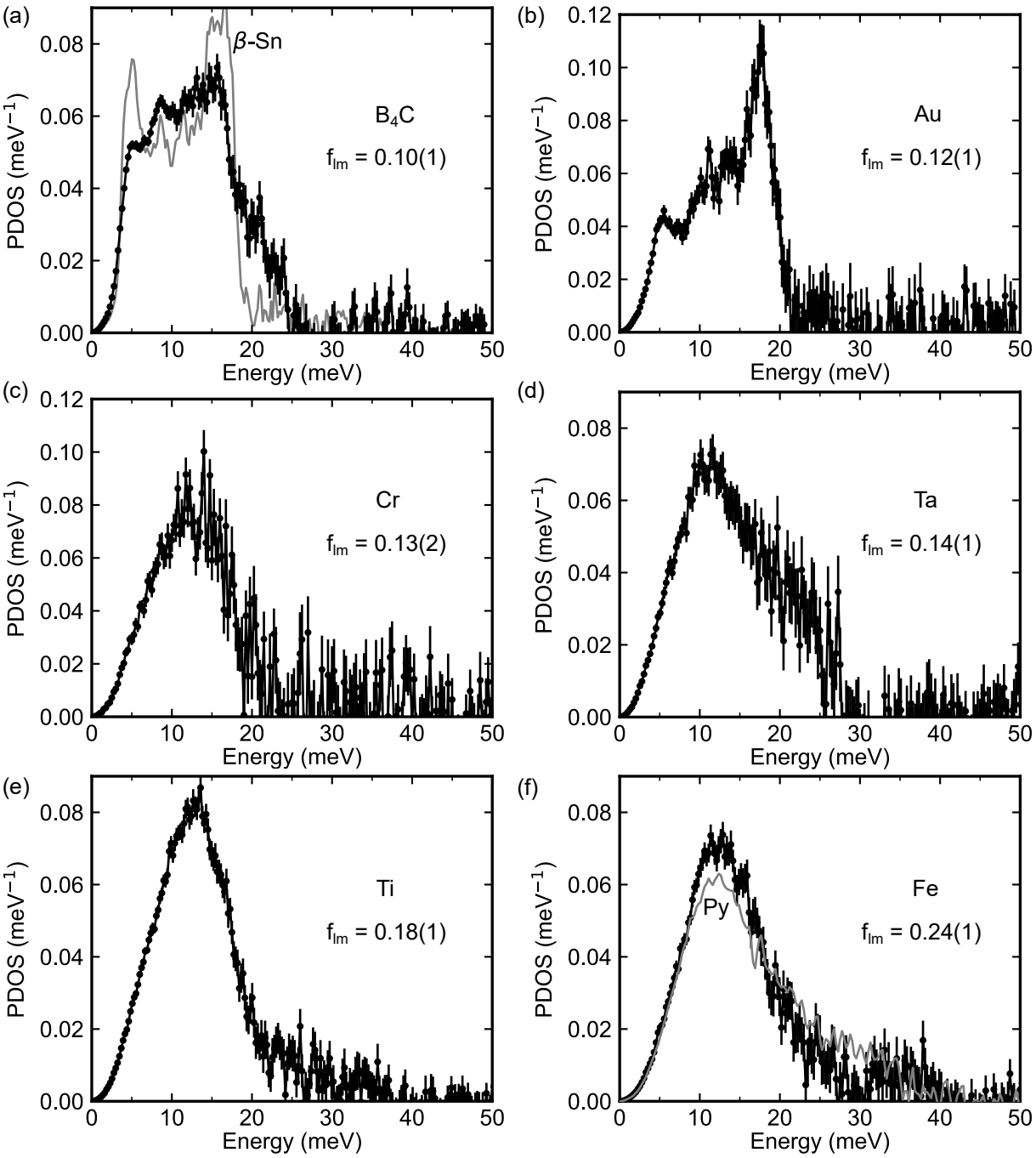

Figure 5.8.: Phonon density of states (PDOS) of a 2 nm tin film inside of (a) boron carbide, (b) gold, (c) chromium, (d) tantalum, (e) titanium and (f) iron. For comparison, the PDOS of bulk β-Sn is plotted in (a) and the PDOS of 2 nm tin in permalloy is plotted in (f) (both in gray). The derived Lamb-Mössbauer factor f_{lm} is given for each system.

The phonon density of states was for example calculated by Liu *et al.* [Liu20] using density functional theory. Neglecting the high energy modes at about 200 meV, the cut-off energy is at 140 meV. Since most phonon modes are at these high energies, the number of phonon modes below 20 meV is tiny. Therefore, the overlap with phonon modes of β-Sn is nearly zero.

In Fig. 5.8(a), the phonon density of states of the 2 nm tin film embedded in boron carbide is shown together with the density of states of bulk β-Sn (gray). Except of some smaller deviations, the shape of the spectrum is similar to β-Sn. The hardness of boron carbide seems to have no effect on the tin layer. Most of the deviations are likely to be caused by the thin layer thickness than by the contact to boron carbide. The suppression of the phonon peaks at 5 meV and 15 meV and the slight increase in low-energy phonons below 5 meV are typical features of nanocrystalline materials [Röh99]. Only the high energy phonon modes might be caused by the vicinity to boron carbide. Parshin *et al.* [Par12] investigated a similar system with tin inside of porous glass. The resulting phonon density of states has the same features as the tin/boron carbide system. A possible bonding between tin atoms and boron carbide could lead to an increase in high energy phonon modes.

In general however, the thin tin film is not affected by the boron carbide surrounding and behaves like β-Sn, contrary to the tin-permalloy system. Therefore, the tin-boron carbide interface appears to be not impacted by mixing or the formation of tin compounds. The Lamb-Mössbauer factor in the tin film is 0.10(1) and, thus, is less increased relative to bulk β-Sn than in the tin films embedded in permalloy.

Tin in gold

In contrast to boron carbide, gold has a phonon density of states in an energy range very close to the energy range of the phonon density of states of β-Sn. Additionally, gold and tin form intermetallic compounds [Liu03] and therefore, the phonons of the tin layer are expected to be influenced.

The phonon density of states of the thin tin layer inside gold is shown in Fig. 5.8(b). While the acoustical β-Sn phonon peak at 5 meV is visible, the strong peak at 17 meV indicates that the tin is heavily affected by the surrounding gold. The phonon density of states of bulk gold in its fcc crystal structure is shown in Fig. 5.9 [Sch81]. The spectrum

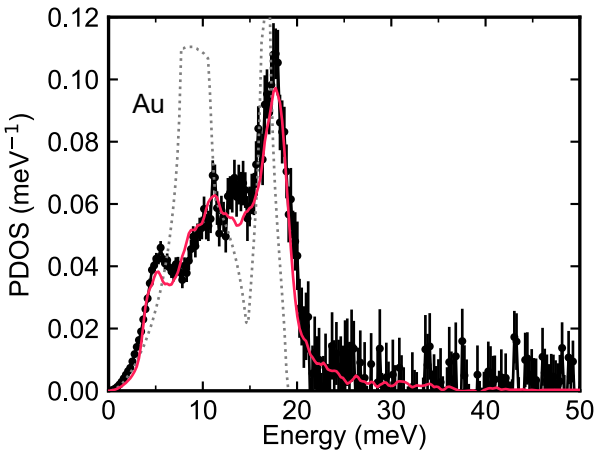

Figure 5.9.: Phonon density of states (PDOS) of a 2 nm tin film inside of gold. Theoretical calculated PDOS of bulk Au is shown in gray (dotted line). The experimental PDOS was fitted according to the Mannheim model [Man71] with a force constant ratio of 1.168 and 40.6% bulk tin. The fit is shown in red.

lies nearly completely within the spectrum of bulk β-Sn with just a slightly larger cut-off energy at 19 meV.

The obtained phonon density of states can be modeled by a linear combination of the phonon density of states of bulk β-Sn, g_{Sn}, and of tin as an impurity inside of the gold matrix, g_{imp}. The latter contribution is again calculated by using Mannheim's impurity model. Since both phonon density of states are based on bulk materials, an additional damping needs to be included to describe the nanocrystalline system correctly. Phonon damping inside nanocrystals can be modeled by a damped harmonic oscillator [Ful10]. In this model, the original phonon density of states g_0 gets convoluted by an energy distribution $D(E', E)$ of a damped harmonic oscillator parameterized by a quality factor Q. The damped phonon density of states g_d is then calculated by, [Röh99]

$$g_d(E) = \int_0^\infty D(E, E') g_0(E') dE', \quad \text{with} \tag{5.6}$$

$$D(E, E') = \frac{1}{\pi Q E} \frac{1}{(E/E' - E'/E)^2 + 1/Q^2}. \tag{5.7}$$

The quality factor is assumed to be constant over the range of phonon energies. The model was successfully applied to reproduce the phonon density of states of nanocrystals in a number of studies, e.g. [Röh99; Sta07; Hou17]. It is based on the description of

the dynamical structure factor in inelastic neutron scattering to incorporate anharmonic phonon interactions [Fåk97].

The experimental phonon density of states g_{exp} was modeled to,

$$g_{\mathrm{exp}} = w_{\mathrm{Sn}} \cdot g_{d,\mathrm{Sn}} + w_{\mathrm{imp}} \cdot g_{d,\mathrm{imp}}, \tag{5.8}$$

with the factors w_{Sn} and w_{imp} to weight the individual contributions of β-Sn and the impurity phonon density of states. The weight factors, the quality factors for both damped oscillators, Q_{Sn} and Q_{imp}, and the force constant ratio for the impurity density of states were used as fit parameters. The result is shown in Fig. 5.9 (black line). The resulting fit parameters are: $w_{\mathrm{Sn}} = 40.5\%$, $Q_{\mathrm{Sn}} = 100$, $w_{\mathrm{imp}} = 59.5\%$, $Q_{\mathrm{imp}} = 10.5$ and the force constant ratio $A_{h-h}/A_{h-i} = 1.17$. The model matches the experimental data well. The fact that more than 50 % of the tin atoms behave like impurity atoms in gold indicates that a substantial amount of tin diffused into gold. Moreover, the presence of pure β-Sn clusters indicate that either a tin recrystallization process after deposition occurs or that the diffusion is so strong that tin clusters segregate along the diffusion paths. Overall it can be concluded that gold has a strong impact on phonons in the thin tin layer. However, since the thermodynamic properties of both metals are similar, the hardness of the tin layer is only slightly changed. This can be seen in the moderately increased Lamb-Mössbauer factor of 0.12(1) in the tin film.

Tin in chromium, tantalum and titanium

The previous two cases featured a material with a vastly different thermodynamic behavior (boron carbide) and a material with a similar behavior compared to β-Sn (gold). In the following, three metal materials are looked at in more detail, chromium, tantalum and titanium, whose thermodynamic behaviors lie in between gold and permalloy.

The bulk phonon density of states of bcc-chromium, bcc-tantalum and hcp-titanium are shown in Fig. 5.10. All three metals have a higher cut-off energy than β-Sn with tantalum at 21 meV, chromium at 40 meV and titanium at 38 meV.

In Fig. 5.8, the obtained phonon densities of states of 2 nm tin layer embedded in chromium (c), tantalum (d) and titanium (e) are shown. All three spectra exhibit a broad phonon peak around 10 meV (tantalum), 12 meV (chromium) and 13 meV (titanium). In chromium there is an additional small feature at 14 meV.

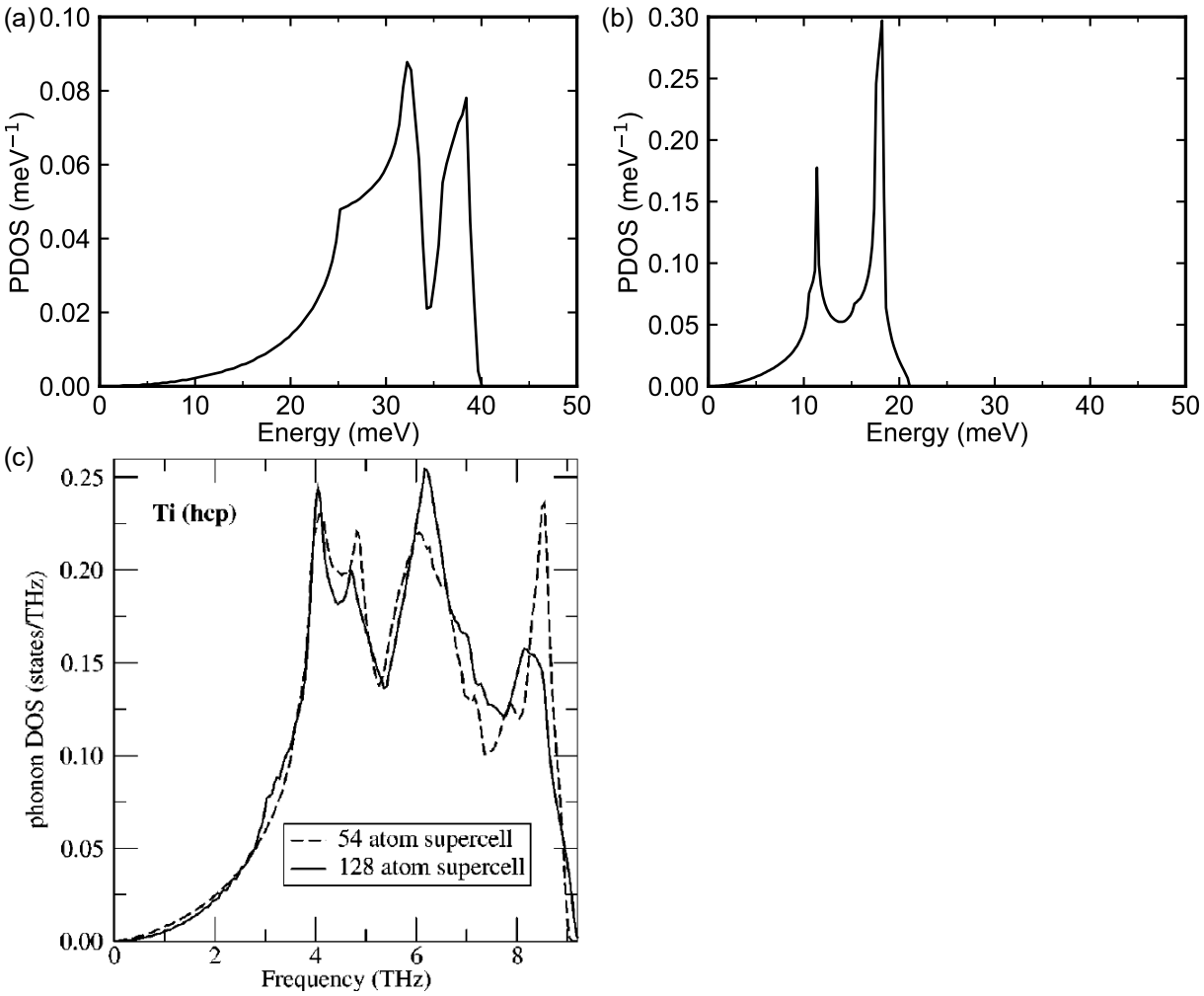

Figure 5.10.: Calculated phonon density of states (PDOS) of (a) bcc-chromium and (b) bcc-tantalum by using literature force constants [Sch81]. (c) Reprinted PDOS of hcp-titanium with permission from Rudin *et al.* [Rud04] (Copyright (2004) by the American Physical Society). For unit conversion: $4.1\,\mathrm{meV} = h \cdot 1\,\mathrm{THz}$ with h being the Planck constant.

The cut-off energy of the tin phonons seems not to correlate with the cut-off energy of the adjacent material (20 meV in chromium, 28 meV in tantalum and about 30 meV in titanium).

Especially in chromium, where the cut-off energy is similar to permalloy, no tin phonon modes are visible above 20 meV. This indicates that tin and chromium do not mix at the interface. Indeed, no intermetallic compound between chromium and tin is reported

in the literature. Still, the measured phonon density of states differs strongly from β-Sn, except from some smaller features, e.g. at 14 meV. As already previously seen in permalloy, this might be caused by a distorted crystal structure in the tin film of only 2 nm thickness. The two effects combined, no mixing and distorted crystal structure, leads to a Lamb-Mössbauer factor of 0.13(2).

In tantalum and titanium, on the other side, the increased cut-off energy of the tin phonons corresponds better to the cut-off energy of the phonons in tantalum and titanium. Tin in tantalum even provides phonon energies above the theoretical cut-off energy of tantalum phonons. This is likely related to the nanocrystalline structure of tantalum, which leads to an increased damping, and a possible presence of the metastable tetragonal tantalum phase. Tetragonal tantalum can be even the dominant crystal phase in thin tantalum films and is thermodynamical harder than bcc tantalum [Aba19]. The high energy phonon modes indicate the presence of tin-tantalum intermetallic compounds, such as Ta_3Sn or Ta_2Sn_3 [Mar17]. Even though tantalum and tin seem to mix at the interface, the tin layer hardness is only moderately increased with a Lamb-Mössbauer factor of 0.14(1) since tantalum does not provide high energy phonons.

The tin-titanium phase diagram provides a variety of stable tin-titanium intermetallic crystal phases [Oka10]. Accordingly, the tin layer has phonon modes up to 30 meV. However, most of the spectral weight in the tin phonon density of states is located below 20 meV. Thus, contrary to the previous cases, the possibility to form intermetallic compounds does not lead to a strong increase in high energy phonon modes in the tin layer. Nevertheless, the additional lack of low-energy phonon modes results in a Lamb-Mössbauer factor of 0.18(1).

Tin in iron

To complete the material study, also the tin-iron system is investigated. The tin phonon density of states is shown in Fig. 5.8(f). In the previous section, this system was discussed already in detail. In comparison to permalloy, shown in gray in the figure, the iron-tin system behaves similarly with a small spectral weight shift to lower energies. This might indicate less mixing at the interface in relation to the permalloy-tin interface. However, overall, the phonon density of states behaves like in the permalloy system, which is expected due to the chemical and thermodynamical similarity between iron and

permalloy. The Lamb-Mössbauer factor in this system is 0.24(1) and thus slightly smaller than in the permalloy-tin system, which also is visible by comparing the force constants in Tab. 5.4. The mean force constant of tin in iron is about 20% smaller than of tin in permalloy.

5.3. Discussion

In summary, the results show that the vibrational behavior of thin tin films is influenced by the thermodynamic properties of the adjacent material, the mixing at the interface and the crystalline structure of the tin layer. The obtained tin phonon density of states varies from a near β-Sn system in boron carbide to a strongly distorted phonon spectrum with modes much higher than the β-Sn cut-off energy in permalloy.

Interfaces between thin films are known to be highly complex. Especially interdiffusion plays an important role in the mixing of two adjacent materials. At room temperature, diffusion in thin films is mainly dominated by diffusion along grain boundaries [Poa81]. Here, the highly disturbed crystal lattice leads to a high atomic mobility [Sut96]. Therefore, grain boundaries act as short-circuit paths for diffusion. Diffusion inside grains, meaning lattice diffusion, is typically many orders of magnitude slower than grain boundary diffusion at room temperature. However, an indirect lattice diffusion can occur, if the grain boundaries migrate: If the grain size changes, previously diffused atoms along the grain boundary will be integrated inside the grain [Sut96]. This "migration" of the grain boundaries occurs, for example, during an annealing process.

The exact diffusion mechanism differs strongly from system to system and simple predictions can hardly be made. Singh *et al.* [Sin84] investigated self-diffusion of tin in films with thicknesses of a couple of hundred nanometers. The films were prepared via thermal evaporation on either a water-cooled substrate or a cryogenically-cooled substrate (liquid nitrogen). While in both systems the grain boundary diffusion is several orders of magnitude higher than lattice diffusion at room temperature, the films which were prepared on the cryogenically-cooled substrate showed significantly enhanced diffusion dynamics. The deposition on a cryogenically cooled substrate leads to smaller crystallites size in the thin film and therefore to more grain boundaries. As a consequence, the grain boundary diffusion is enhanced. While this study was focused on tin films, the influence of the cooling deposition method on other metal films is likely to be similar. Thus, *the applied*

preparation method increases the interdiffusion and therefore renders engineering of the thermodynamic properties of tin layers possible.

The driving force for the grain boundary diffusion is generated by chemical potential differences. Especially when intermetallic compounds can be formed, there is a strong desire by the materials to mix [Poa81]. In the above described inelastic measurements, the systems, where tin forms intermetallic compounds with its adjacent material, showed a strongly distorted phonon density of states with phonon modes above the cut-off energy of β-Sn. On the other side, in systems, where tin does not form intermetallic compounds, i.e. in boron carbide and chromium, the measured phonon density of states features predominantly low energy phonons in the region expected for β-Sn. Especially in boron carbide, which has covalently bonded atoms and an amorphous film structure, mixing at the interface, and therefore diffusion, appears not to be present at all. Amorphous materials are homogeneously disordered, meaning there is no long distance order and also no grains. Therefore, there are no grain boundaries, which would provide a short circuit diffusion path. Due to the lack of mixing, the tin re-crystallizes upon annealing to room temperature and therefore vibrational behavior of β-Sn can be measured.

The tin-chromium system provides a different case. Even though, no intermetallic compounds can be formed, chromium is likely to be in a nanocrystalline crystal form. That means, that the film structure is inhomogeneously disordered, because it consists of nanometer sized crystalline grains between which the chromium is strongly disordered. Therefore, there are short circuit diffusion paths in contrast to the amorphous boron carbide films. Thus, at the tin chromium interface, diffusion to a small extend is possible. Since the tin film is only 2 nm thick, which are about five atomic layers, chromium impurities can lead to a suppression of the re-crystallization process of tin [Buc52]. Subsequently, although tin only mixes up to a small amount with chromium, the suppression of crystallization could lead to the still distorted phonon density of state measured in the tin chromium system.

In contrast to the cases of chromium and boron carbide, the tin-gold system forms multiple intermetallic compounds. Additionally, gold is known to strongly interdiffuse with its surrounding material [Poa81]. Thus, not only intermetallic compounds are formed at the interface but also a tin segregation along the grain boundaries can be expected. This is confirmed by a high resolution transmission electron microscopy (HR-TEM) measurement which was combined with energy dispersive X-ray spectroscopy (EDX) to allow for

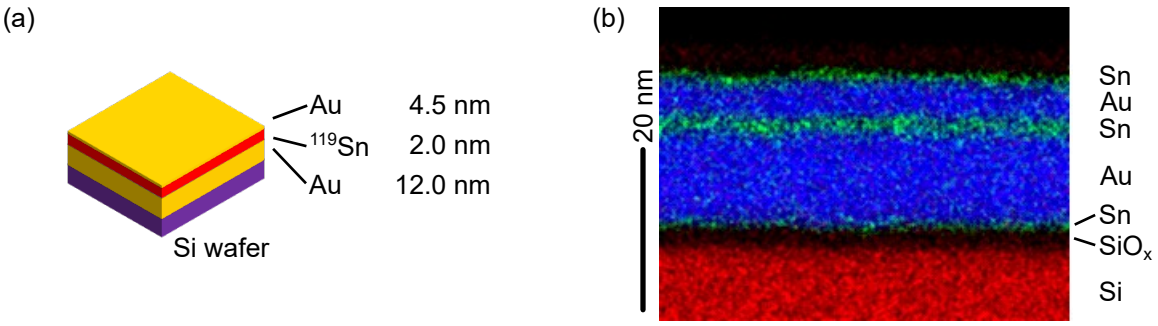

Figure 5.11.: (a) Schematic of the gold-tin layer structure. (b) High resolution transmission electron microscopy measurement combined with energy dispersive X-ray spectroscopy. The chemical elements are color coded: Silicon (red), gold (blue) and tin (green).

element detection[1]. The measurement was performed on a gold-tin layer system which was not capped by tantalum. A schematic of the sample is shown in Fig. 5.11(a). The result of the EDX HR-TEM measurement is shown in Fig. 5.11(b). Even though the preparation method ensures that tin was only deposited between both gold films, tin is found below and above gold. Thus, tin diffusion in gold must be so strong that tin atoms diffused through the gold layer and segregated on the surface. This mechanism was enhanced in this particular layer system since no tantalum was deposited on top of the sample. Therefore, there is a thermodynamical pressure on tin to diffuse to the surface in order to oxidize. This phenomenon can also be found in gold-titanium systems, for example [Poa81]. Thus, the gold-tin system is affected by strong interdiffusion, leading to the formation of gold-tin intermetallic compounds and segregation of tin.

In conclusion, the thermodynamic properties of a thin tin film can be tuned by embedding it in an appropriate metal. The requirement is interdiffusion at the metal-tin interface, which can be achieved by choosing a material which forms intermetallic compounds with tin. The phonon density of states of the tin film is then strongly influenced by the phonons of the adjacent material. The influence can be simulated within an impurity model, even though not in all cases, e.g. not in tantalum or titanium. With a thickness above 3 nm the tin layer behaves increasingly like tin, since the influence of the interface influence decreases.

In the investigated systems, the thin tin layer embedded in permalloy has the most increased hardness. The Lamb-Mössbauer factor in the 1 nm tin film is 0.33(1). Therefore,

[1] conducted by *Eurofins Material Science Netherlands B.V.*

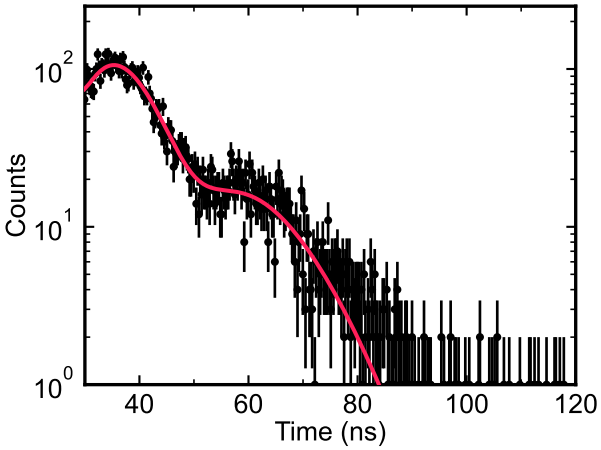

Figure 5.12.: Temporal nuclear decay of 2 nm tin embedded between two 10 nm titanium layers. The fit is shown in red.

the nuclear resonance scattering cross-section is increased by a factor of more than eight relative to bulk β-Sn. From a nuclear quantum optics perspective, the tin-titanium system offers the most with an increased Lamb-Mössbauer factor of 0.18 and a material (titanium) with a low density (4.5 g/cm^3). However, to employ thin tin films in nuclear quantum optics, the Lamb-Mössbauer factor is only one aspect. A second important aspect is the hyperfine structure of the tin film. An unperturbed hyperfine structure is desired in order to have an ideal two-level quantum system. Therefore, nuclear resonance scattering was conducted on the tin film embedded in titanium. The nuclear decay recorded at an incidence angle of 0.242° is shown in Fig. 5.12. The decay exhibits multiple beats which indicates already a splitted hyperfine structure. A fit was produced by assuming a β-Sn site with the theoretical values for isomer shift and quadrupole splitting, see Tab. 2.1, and an unknown tin compound. By using the software CONUSS, the unknown compound contributes to the hyperfine structure by 46(1)%, is isomer shifted relative to β-Sn by 0.89(1) mm/s and has a quadrupole splitting of 0.67(1) mm/s. These values are close to Ti_2Sn: Isomer shift relative to β-Sn of 0.78 mm/s and quadrupole splitting of 0.99 mm/s [O'B03]. Thus, even though the thermodynamic properties might allow to use tin films inside titanium for nuclear quantum optics, due to the perturbed hyperfine structure, the tin films provide no benefit over typical iron thin films. Also tin inside permalloy has, as shown in Fig. 5.5, a complex hyperfine structure. Thus, while the goal of engineering the thermodynamic properties to increase the Lamb-Mössbauer factor of thin tin films

was achieved, the enhancement of the crystal rigidness came so far at the expense of an increasingly perturbed hyperfine structure. Therefore, for the following nuclear quantum optics experiments, tin dioxide layers are prepared, since stannic oxide has in its bulk form a high Lamb-Mössbauer factor.

Apart from nuclear resonance scattering, the ability to engineer the phonon density of states in thin tin films allows tune the thermal conductivity for thermoelectrical applications or the design of phonon-photon cavities for the investigation of acousto-optical interactions.

6. Quantum optics with ^{119}Sn

In nuclear quantum optics, the fundamental aspects of photon-matter interaction in the X-ray regime are investigated by the excitation of nuclear resonances. Thereby, the nucleus with its extremely narrow resonance linewidth combined with an ideally unsplit hyperfine structure models a prototypical two-level quantum state system. Due to the coherent nature of the nuclear excitation, also collective effects of an ensemble of nuclei are accessible. An important requisite of nuclear quantum optics studies is the thin film cavity. The design of a thin film cavity was described in section 3.4. A strong enhancement of the excitation field can be achieved inside the thin film cavity, and thus an enhancement of the interaction strength between nuclei and X-rays. By different designs of the thin film cavity, quantum optical effects were measured in the X-ray regime, e.g. the collective Lamb shift [Röh10], electromagnetically induced transparency [Röh12], subluminal propagation of the X-ray pulse [Hee15] or the observation of Rabi oscillation between two resonant layers [Hab17].

While the design of the thin film cavities were varied, all studies so far employed the nuclear resonance of ^{57}Fe at 14.41 keV. ^{57}Fe has some advantages in comparison to other isotopes, however also some disadvantages. The nuclear properties of ^{57}Fe in comparison to the ^{119}Sn resonance are listed in Tab. 6.1. The resonance linewidth is even narrower in ^{57}Fe than in ^{119}Sn with a natural linewidth being five times smaller than the linewidth of ^{119}Sn. Additionally, the nuclear resonance absorption cross section is nearly twice as high at the iron resonance. But, more importantly than the nuclear properties, common iron compounds have suitable material properties for thin film studies. Iron and most of its typical intermetallic compounds are easy to handle materials and have typically high Lamb-Mössbauer factors of about 0.8. It is therefore not surprising that ^{57}Fe is the most common isotope in Mössbauer studies. Also most beamlines at synchrotrons which offer nuclear resonance scattering are typically equipped with a well running setup optimized for the ^{57}Fe resonance.

Table 6.1.: Comparison of the nuclear parameters between the isotopes ^{119}Sn and ^{57}Fe taken from [MED]. Advantageous parameters for nuclear quantum optics are colored in green. The nuclear resonance cross section, σ_0, was calculated by equation 2.14 and the electronic absorption cross section by the use of the scattering factor f_2 provided by [CXR], see section 3.3.1. The magnetic moments are given in units of the nuclear magneton $\mu_N = 5.051 \times 10^{-27}\,\mathrm{J/T}$.

Parameter	^{119}Sn	^{57}Fe
Energy (keV)	23.88	14.41
Γ_0 (neV)	25.3	4.66
τ_0 (ns)	26.0	142
Natural abundance (%)	8.6	2.1
Magnetic moment (ground) (μ_N)	-1.05	0.09
Magnetic moment (excited) (μ_N)	0.63	-0.15
Quadrupole moment (ground) (barn)	0.0	0.0
Quadrupole moment (excited) (barn)	0.09	0.16
Internal conversion factor α	5.22	8.2
Nuclear resonance absorption cross section σ_0 (kbarn)	1379.6	2560.5
Total electronic absorption cross section at resonance σ_{Ph} (kbarn)	2.39	5.83
Nuclear to electronic ratio σ_0/σ_{Ph}	578.3	439.1

However, the major disadvantage of the ^{57}Fe nuclei is that most iron compounds have a split hyperfine structure, especially in thin films. This can be troublesome in nuclear quantum optics experiments, where a clean two-level quantum system is mostly desired. For example, metallic iron in its α crystal structure is ferromagnetic at room temperature, which leads to a magnetic hyperfine field of about 33 T and therefore to a magnetic splitting of the nuclear levels. To counter that, iron thin films are prepared with thicknesses below 1 nm, since the ferromagnetic phase is not stable in these ultrathin films. However, a strong quadrupole splitting is found in these films with strengths of about seven times of the natural linewidth of the ^{57}Fe resonance [Röh10]. Also paramagnetic compounds with iron such as stainless steel in its austenitic phase have, when prepared as thin films, a strong quadruple splitting [Sah11]. Therefore, a thin film material, which only has a single nuclear transition, has yet to be found.

This chapter introduces the ^{119}Sn resonance for nuclear quantum optics experiments. Since it is also a common Mössbauer isotope, most nuclear scattering beamlines are

equipped with a setup designed for the ^{119}Sn resonance. As Tab. 6.1 shows, there are multiple nuclear properties where ^{119}Sn nuclei are superior to ^{57}Fe nuclei. The most obvious advantage is its higher resonance energy, which leads to less electronic absorption as specified by the total electronic absorption cross section in Tab. 6.1. This is especially important for thin film cavities since less electronic absorption leads to higher field enhancements in the cavity. For nuclear quantum optics studies, the most interesting parts are the material properties of tin and its compounds. The metallic β-Sn phase is paramagnetic and thus has no magnetic hyperfine field. The hyperfine structure is only perturbed by a tiny quadrupole splitting which is smaller than its natural linewidth [Soa73]. This might change in thin films and is heavily dependent on its environment as seen in the previous chapter. Also stannic oxide (SnO_2) is non magnetic and has only a small quadrupole splitting of about two times its natural linewidth. Thus, β-Sn and tin dioxide have only slightly perturbed hyperfine structures and are therefore close to a prototypical two-level quantum system.

A disadvantage of tin is its low Lamb-Mössbauer factor. Especially the metallic β-Sn phase with its Lamb-Mössbauer factor of 0.04 is therefore unattractive for nuclear quantum optics experiments, since the probability for a coherent elastic scattering process is strongly decreased. By tuning the thermodynamic properties of the thin tin films, the Lamb-Mössbauer factor can be increased, as described in chapter 5. However, so far an increase of the Lamb-Mössbauer factor was accompanied by a perturbed hyperfine structure. An alternative is tin dioxide. The oxide compound has already a high Lamb-Mössbauer factor of 0.6 in its bulk form and therefore no engineering of the thermodynamic properties is needed. Consequently, diffusion at the interface should be suppressed in order to have bulk tin dioxide hyperfine properties in the tin dioxide film with its only small quadrupole splitting. Thus, for the following experiments, the tin dioxide films are embedded in boron carbide since the tin-boron carbide system showed only little signs of interface diffusion in the previous chapter. In combination with the covalently bound atoms in tin dioxide, interlayer diffusion should be drastically reduced. Even though a Lamb-Mössbauer factor of 0.6 is still smaller than of typical iron compounds, the ^{119}Sn resonance is less likely to decay via an internal conversion process than ^{57}Fe, as quantified by the internal conversion factor in Tab. 6.1. Thus, roughly the same amount of tin nuclei in tin dioxide take part in nuclear resonance scattering than iron nuclei in typical iron compounds.

Since the hyperfine structure of tin dioxide films should not change with the thickness, studies of thin film cavities embedding also thick resonant layers can be performed. In this chapter, the collective Lamb shift is measured in thin film cavities containing tin dioxide films with increasing thicknesses. In the following, a brief description of the collective Lamb shift is given before the results of the thin film cavities are presented and discussed.

6.1. The collective Lamb shift

In its theoretical description, the collective Lamb shift resembles the "normal" single-atom Lamb shift. While the latter is connected to the spontaneous decay of an excited state placed in a reservoir of infinite photon modes, the collective Lamb shift is connected to the superradiant decay of a coherently excited ensemble of resonators.

A theoretical review of the superradiant decay and the collective Lamb shift is given, e.g. by Gross *et al.* [Gro82]. The main condition for superradiant decay is that the generic ensemble of resonators consists of indistinguishable constituents. Therefore, the system state and its evolution does not change under all permutations of its constituents. When a light pulse coherently excites the ensemble, the excitation is then delocalized over all constituents of the ensemble. The coherently excited state $|\psi_c\rangle$ can mathematically be expressed by [Röh20],

$$|\psi_c\rangle = \frac{1}{\sqrt{N}} \sum_a^N |e_a\rangle \, |G_0(a)\rangle \,, \tag{6.1}$$

which is the sum over all N resonators with resonator a being in the excited state $|e_a\rangle$, while all others are in the ground state $|G_0(a)\rangle$, which is a sum over all individual ground states excluding resonator a. Due to the delocalization, the subsequent decay is N times more probable. Hence, the decay is N times accelerated, an effect which is called "superradiance".

A complete description of the ensemble within a quantum mechanical framework leads not only to the superradiance phenomenon but also to an energy shift of the resonance [Gro82]. The energy shift originates from the interaction of one resonator with the photon modes of a reservoir of infinite photon modes (Lamb shift) and from an additional interaction between different resonators. The latter contribution is mathematically described by the exchange of virtual photons between the resonators, and leads to a term which is equal to a dipole-dipole interaction [Gro82]. Due to its similarity to the Lamb shift, the

energy shift of the collectively excited nuclei is called collective Lamb shift.

The discussion so far is limited to the case where the wavelength of the incident radiation is much bigger than the spatial dimensions of the ensemble, i.e. $kR \ll 1$, with k being the wave vector and R the spatial dimensions of the ensemble. If this condition fails, the excitation of each constituent is weighted by the phase factor $e^{i\vec{k}\vec{r}_a}$ accounting for the resonator position $\vec{r}_a$. Then, the collective excitation is given by [Röh20],

$$|\psi_c\rangle = \frac{1}{\sqrt{N}} \sum_a^N e^{i\vec{k}\vec{r}_a} |e_a\rangle |G_0(a)\rangle . \tag{6.2}$$

For example, the resonance of a single resonator is given by,

$$f(E) \propto \frac{1}{E - E_0 + i\Gamma_0}, \tag{6.3}$$

where E_0 is the resonance energy and Γ_0 is the resonance linewidth. In the large ensemble limit, i.e. $kR \gg 1$, the incorporation of collective effects leads to a replacement of $i\Gamma_0$ with a complex-valued correction Δ_c given by [Röh20],

$$\Delta_c = i\Gamma_c \left(1 - \frac{iS}{kR}\right) \qquad \text{with} \quad \Gamma_c = \frac{2\pi\rho_n R}{k^2}\Gamma_0, \tag{6.4}$$

with ρ_n being the number density of the resonators and S an ensemble geometry dependent factor. The imaginary part of Δ_c results in a broadening, the superradiance, and the real part leads to an energy shift, the collective Lamb shift. The correction Δ_c depends therefore on the density of resonators, as expected for collective effects, and on the ensemble geometry, quantified by the factor S.

The description of the collective excitation in Eq. 6.2 is identical to the description of a nuclear exciton, see Eq. 2.15. Thus, the coherent nature of the nuclear excitation renders the measurement of collective effects such as the collective Lamb shift in general possible. The measurement, however, requires a strong coupling strength between the nuclei and photons since otherwise the collective effects are easily eclipsed by inhomogeneous broadening effects, originating from slight variations in the environment of the nuclei [Röh20]. Such a strong coupling strength is provided inside a thin film cavity [Röh10]. In the thin film cavity, the incident radiation is strongly enhanced due to the formation of a standing wave, see section 3.4. If the resonant nuclei are placed in the center of the cavity, where

the enhancement is the strongest, the nuclei can interact with the high photonic density resulting in a strong enhancement of the collective effects. E.g. in a thin film cavity containing an ultrathin iron layer, a collective Lamb shift was measured which shifted the resonance by nine times the natural linewidth [Röh10].

The dynamics of the nuclear ensemble inside a thin film cavity can be described by the transfer matrix method, which was briefly explained in section 3.3.1. In this method, each layer is described by a layer matrix, which incorporates the light propagation along the reflection channel and the transmission channel. Thereby, the light pulse is assumed to incide on the sample under a small angle ϑ. The layer matrix of layer i, $\mathbf{L}_i$, is given by [Rö04],

$$\mathbf{L}_i = e^{i\mathbf{F}_i d_i} \qquad \text{with} \quad \mathbf{F}_i = \begin{pmatrix} f_i + k_{0z} & f_i \\ -f_i & -f_i - k_{0z} \end{pmatrix}, \tag{6.5}$$

with d_i being the layer thickness, k_{0z} the z-component of the incident light wave vector, i.e. $k_{0z} = k_0 \sin\vartheta$, and f_i the scattering amplitude of layer i. In general, f is polarization dependent and is therefore a 2x2 matrix [Rö04]. However, for the here assumed case of non-magnetic scattering, the polarization of the photon does not change after scattering rendering f a scalar quantity. The scattering amplitude f incorporates electronic and nuclear scattering and is given by,

$$f = \frac{2\pi}{k_{0z}} \rho_n (-r_e f_1 + i r_e f_2 + f_N), \tag{6.6}$$

with ρ_n being the number density, f_1 and f_2 the atomic scattering factors, as described in section 3.3.1, and f_N the nuclear scattering amplitude given by Eq. 2.13 for the ideal case of no hyperfine splitting. The transfer matrix $\mathbf{M}$, as defined in section 3.3.1 is then given by the matrix product of all layer matrices: $\mathbf{M} = \prod_i \mathbf{L}_i$.

With the transfer matrix calculated, the reflection coefficient of the thin film cavity can be determined by the transfer matrix components with $r = -M_{21}/M_{22}$. With this method, arbitrary thin film structures can be calculated. All information about the hyperfine structure of the resonant layer is contained in the nuclear scattering amplitude.

To calculate a thin film cavity with an embedded resonant layer, a compact analytical solution can be found if the resonant layer is assumed to be ultrathin. For an ultrathin resonant layer, the matrix exponential of the resonant layer matrix, $\mathbf{L}_N$, can be truncated

after first order, leading to [Rö04]

$$\mathbf{L}_N = e^{i\mathbf{F}_N d_N} \approx (\mathbf{I}_2 + i d_N \mathbf{F}_N), \tag{6.7}$$

where $\mathbf{I}_2$ is the 2x2 identity matrix and d_N the thickness of the resonant layer. Assuming a single nuclear transition with a Lorentzian resonance, the nuclear scattering amplitude is given by Eq. 2.13. Within the ultrathin film approximation, the reflection coefficient of the thin film cavity is then given by, [Rö04]

$$r(E) \propto \frac{1}{E - E_0 + i\Gamma_0/2 + \Delta_c} \quad \text{with} \tag{6.8}$$

$$\Delta_c = i\frac{\Gamma_0}{2} f_0 \rho_N d_N \left(|\mathrm{Re}\,(pq)| + i\mathrm{Im}\,(pq)\right) \quad \text{and} \quad f_0 = \frac{f_{LM}\sigma_0}{2\sin\vartheta}, \tag{6.9}$$

where σ_0 is the resonant cross-section as defined in Eq. 2.14, f_{LM} is the Lamb-Mössbauer factor, ρ_N is the number density of the resonant isotope. The cavity enters the equation by the field amplitudes p and q at the position of the resonant layer. They are calculated by a truncated transfer matrix, which connects the field amplitudes at the position of the resonant layer with the field amplitudes above the cavity. Similar to Eq. 3.4, the truncated matrix $\mathbf{M}_{z_N}$ at the position of the resonant layer is defined by, [Rö04]

$$\begin{pmatrix} E^T_{z_N} \\ E^R_{z_N} \end{pmatrix} = \mathbf{M}_{z_N} \begin{pmatrix} E^T_0 \\ E^R_0 \end{pmatrix}, \tag{6.10}$$

with z_N being the depth position of the resonant layer and $(E^T_{z_N}, E^R_{z_N})$ the field amplitudes at the position of the resonant layer in the transmission and reflection channel. The truncated matrix $\mathbf{M}_{z_N}$ includes all layer matrices from the resonant layer to the uppermost layer. The total field amplitude at the resonant layer is therefore given by,

$$E^T_{z_N} + E^R_{z_N} = \left((\mathbf{M}_{z_N})_{11} + (\mathbf{M}_{z_N})_{21}\right) E^T_0 + \left((\mathbf{M}_{z_N})_{22} + (\mathbf{M}_{z_N})_{12}\right) E^R_0, \tag{6.11}$$

where $(\mathbf{M}_{z_N})_{ij}$ are matrix elements of the truncated transfer matrix. The amplitudes p and q are then defined by, [Röh10]

$$p = (\mathbf{M}_{z_N})_{11} + (\mathbf{M}_{z_N})_{21} \quad \text{and} \quad q = (\mathbf{M}_{z_N})_{22} + (\mathbf{M}_{z_N})_{12}\,. \tag{6.12}$$

The parameters p and q are therefore the field amplitudes from the transmission channel and reflection channel contributing to the total field amplitude at the position of the resonant layer. For the calculation, resonant interactions are excluded [Röh10], therefore, p and q capture the field enhancement effect of the "empty" cavity.

In Eq. 6.8, the complex-valued correction Δ_c carries again the information about the collective excitation with the imaginary part being the superradiant broadening and the real part the collective Lamb shift. Thereby, the Lamb shift appears to be negative indicating an attractive force between the resonators similar to the van-der-Waal force. Within the ultrathin film approximation, the collective Lamb shift scales therefore with the areal density of the resonant layer $\rho_N d_N$ and the wave field amplitudes, p and q, at the position of the resonant layer, i.e. the field enhancement of the thin film cavity. The exact geometry of the nuclear ensemble, however, does not play a role in the ultrathin film approximation, since the film dimension is much smaller than the wavelength of the standing wave formed in the thin film cavity and therefore, $\exp(i\vec{k}\vec{r}_a) \approx 1$.

With increasing layer thickness, the collective Lamb shift is expected to increase. Within the ultrathin layer approximation, the increase is linear provided that the field enhancement is constant. The latter assumption, however, is hardly true since the resonant layer disturbs the wave field in the cavity substantially with increasing thickness due to electronic absorption. Additionally, the wave field within the resonant layer varies for an increased layer thickness, rendering the phase factor of Eq. 6.2 important.

In Fig. 6.1(a), the energy dependent reflectivity $R(E) = |r(E)|^2$, is shown for thin film cavities embedding increasingly thick tin dioxide layers. The thin film cavity consists of a boron carbide guiding layer sandwiched between two platinum mirror layers. The thickness of the capping platinum layer is adjusted to allow a maximum field enhancement inside the cavity, called also "critical coupling". The tin dioxide layer is embedded in the center of the guiding layer. The simulations are done with the transfer matrix method using the software package pynuss. For the thinnest tin dioxide layer (a hypothetical 0.01 nm thickness, gray), nearly no collective effect is visible. However, with increasing thickness the energy spectrum becomes broader (superradiance) and is increasingly shifted to negative energies (collective Lamb shift). While the spectra for the thinner tin dioxide layers are Lorentzian-like as expected from the ultrathin approximation, see Eq. 6.8, the spectra of the thicker layers (5 nm and 10 nm) exhibit a dip at resonance. This feature emerges due to the increasing relevance of the phase factor of Eq. 6.2. The nuclei in the

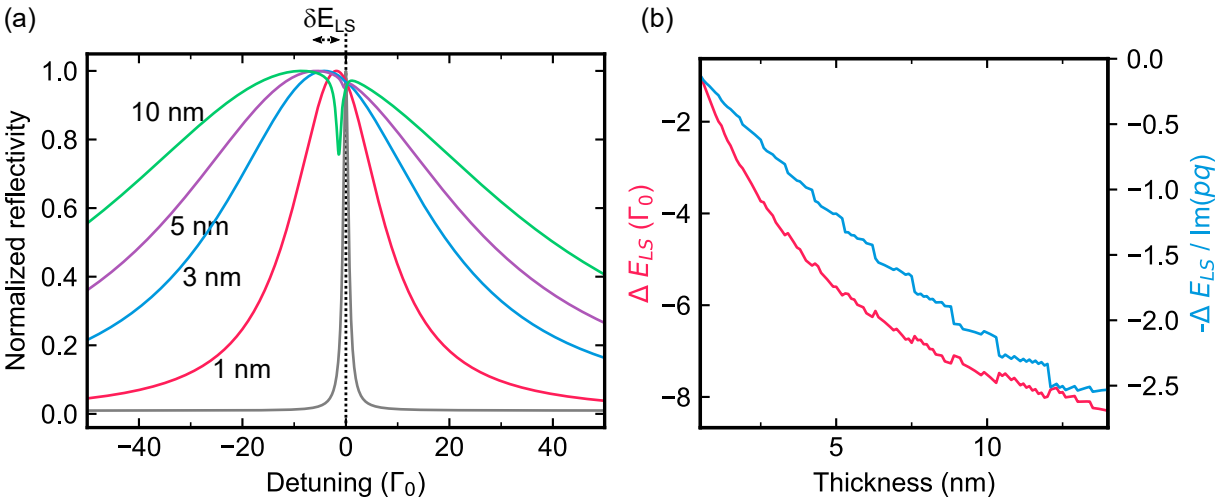

Figure 6.1.: (a) Simulated energy dependent reflectivity for thin film cavities embedding a 0.01 nm (black), 1 nm, 3 nm, 5 nm or 10 nm tin dioxide film. The collective Lamb shift δE_{LS} is indicated. The energy is given by the detuning relative to the resonance energy at 23.88 keV in units of the natural linewidth $\Gamma_0 = 25.3$ neV. (b) Collective Lamb shift in energy units (red) and normalized by the field enhancement via Im(pq) (blue) as a function of the tin dioxide layer thickness.

resonant layer experience different field enhancements depending on their position in the cavity.

The collective Lamb shift in energy units and normalized by Im(pq) are shown as a function of the tin dioxide layer thickness in Fig. 6.1(b). The shift is derived by fitting the simulated energy spectra to a Lorentzian. As expected, the resonance is increasingly shifted to negative energies with increasing thickness. Thereby, the normalized collective Lamb shift exhibits a linear relation to the tin dioxide layer thickness as predicted by the ultrathin layer approximation, see Eq. 6.8. Due to the emergence of the dip feature at resonance, the fit with a Lorentz function becomes increasingly imprecise with thicker tin dioxide layers resulting in the additional small structure on top of the curve.

While the transfer matrix is a robust method to calculate quantum optical effects, the insights into the origin of the effects are limited. Therefore, a quantum optical framework was developed by Heeg *et al.* [Hee13] which describes the nuclear system as well as the incident light quantum mechanically. Derived from this model, the collective Lamb shift arises from the coherent coupling of different nuclei with the cavity mode. Thereby, the collective Lamb shift scales with $N|g|^2$, with N being the number of nuclei and g

the coupling constant which accounts for the field enhancement of the cavity. Thus, the model predicts an increasing collective Lamb shift with an increasing layer thickness as well since the number of nuclei increases. The model assumes that the waveguide mode of the cavity can be modeled by two photon modes accounting for the reflection and transmission channel. However, in the perturbed case of a thick resonant layer, multiple modes need to be included. The inclusion combined with a division of the thick resonant layer into multiple subensembles results in the emergence of the spectral feature at resonance as seen in Fig. 6.1(a) [Len20]. The dip can be attributed to a coherent coupling of the different regions inside the resonant layer. The feature is therefore similar to the electromagnetically induced transparency phenomenon which emerges if two separate resonant layers are used [Röh12].

To measure thickness dependent nuclear quantum optics effects, the hyperfine structure of the employed resonant material should be constant over the thickness range. As previously discussed, tin dioxide is a promising candidate for these studies. In the following, the collective Lamb shift as a function of thickness is measured.

6.2. Collective Lamb shifts in SnO_2 cavities

For the measurement of the collective Lamb shift, cavities are prepared with an increasing thickness of the embedded tin dioxide layer. In Fig. 6.2, the reflectivity measurements of all thin film cavities are shown together with a sketch for each sample structure. The cavities consists of two platinum layers as the outer mirror layers, and a boron carbide layer as the guiding layer for the X-rays. After half of the boron carbide layer is prepared, the tin dioxide layer is deposited and subsequently capped with the other half of the boron carbide layer. Therefore, the tin dioxide layer is centered in the guiding layer. The total boron carbide layer thickness is about 16 nm and the thickness of the tin dioxide layer is 1 nm, 3 nm, 6 nm or 9 nm. For the preparation, isotopically enriched ^{119}Sn material was used. Additionally, a cavity was prepared where the guiding layer consists completely of tin dioxide. Here, the tin dioxide layer has a thickness of 10 nm.

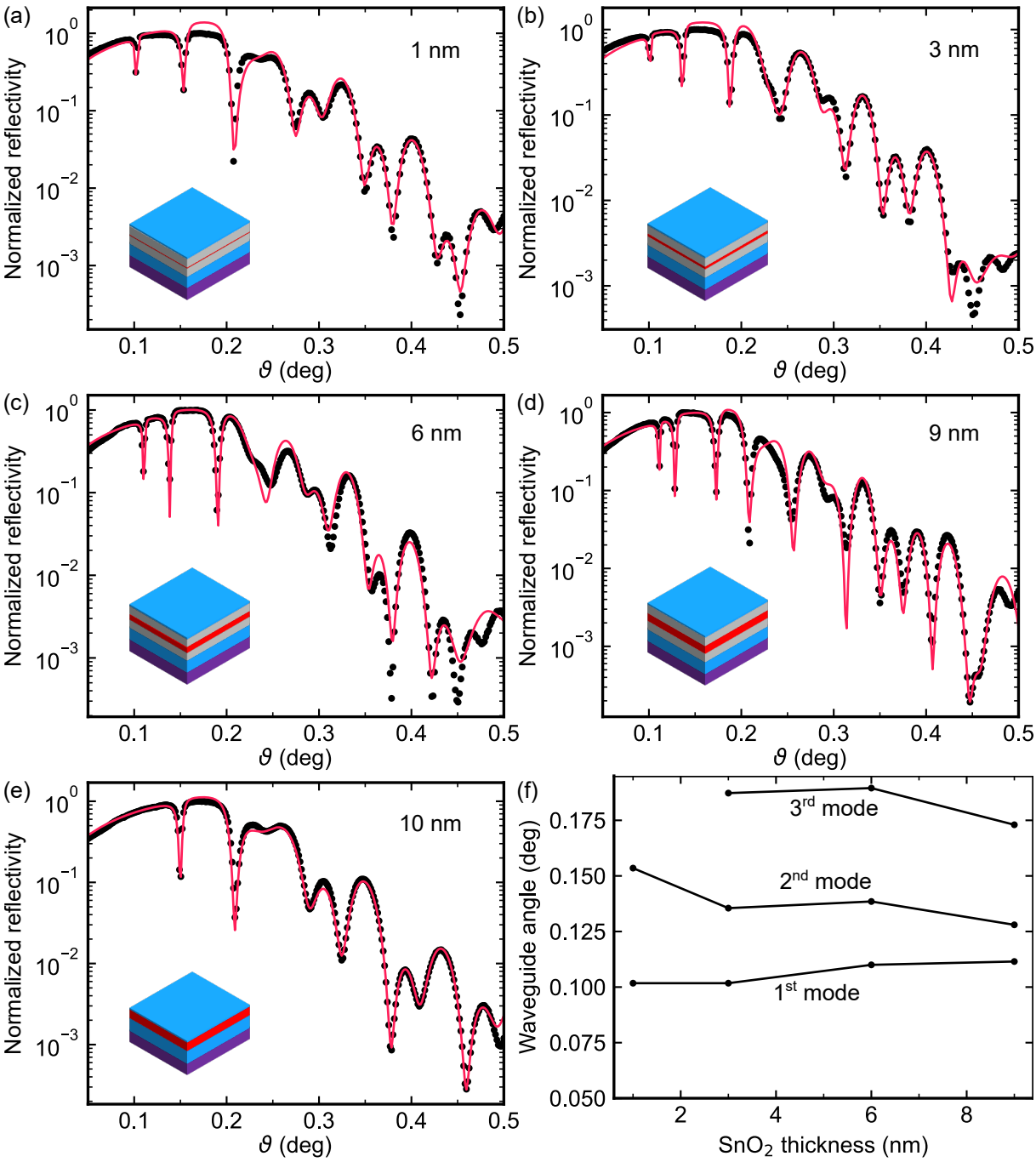

Figure 6.2.: Reflectivity measurements of the thin film cavities embedding a (a) 1 nm, (b) 3 nm, (c) 6 nm and (d) 9 nm SnO_2 film using 23.88 keV X-rays. A schematic of each cavity structure is shown as inset with the materials color coded: Tantalum (blue), boron carbide (gray), tin dioxide (red) and silicon (violet). Additionally, the reflectivity of a 10 nm SnO_2 film inside a cavity without boron carbide is shown (e). The fit (red) was done by GenX. (f) Derived incidence angles of the first, second and third waveguide mode as a function the tin dioxide layer thickness in the cavity.

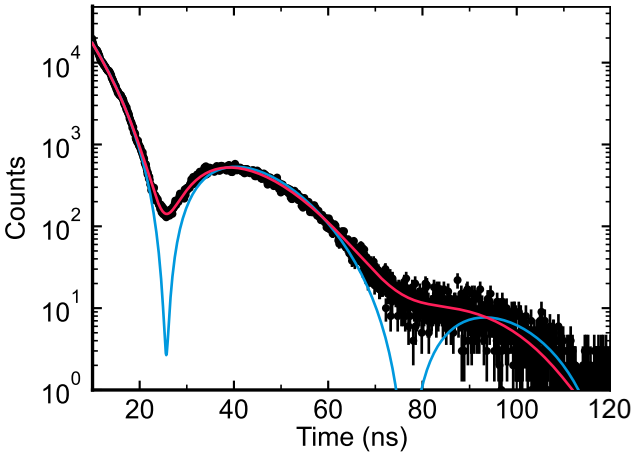

Figure 6.3.: Temporal nuclear decay after X-ray pulse excitation of the reference absorber consisting of tin dioxide together with the fit from CONUSS with (red) and without (blue) thickness distribution.

All layer thicknesses are confirmed by a fit using the software GenX of the reflectivity measurements, which is overlaid on the data shown in Fig. 6.2. The fit results of all structures are listed in the appendix A.1.1.

The reflectivities are shown in Fig. 6.2(a-d). At multiple angles the cavities exhibit pronounced minima below the critical angle of platinum (at 0.2°), the cavity resonances. At these angles, the X-rays couple into the cavity, get strongly enhanced by forming a standing wave and, in an ideal cavity without damping, eventually couple out at the borders of the sample. The incidence angles of the first, second and third waveguide mode derived from the reflectivities are shown in Fig. 6.2(f) as a function of the tin dioxide layer thickness in the cavity. For the measurement of the collective Lamb shift, the first waveguide mode is of interest since the maximum intensity of the standing wave is at the position of the tin dioxide layer. Also possible would be the third waveguide mode, which is formed in the thicker cavities. Because the cavities are designed to have the maximum intensity at the tin dioxide layer in the first waveguide mode, the incidence angle of the nuclear resonance scattering setup is set to the first dip of the reflectivity intensity.

The acquisition of the energy spectrum of the sample requires a precise knowledge of the hyperfine structure of the reference foil. Therefore in a first step, the tin dioxide foil is analyzed. The temporal nuclear decay of the reference foil is shown in Fig. 6.3. Using CONUSS, the decay pattern can be modeled by a 61(1) µm thick tin dioxide foil

with a quadrupole splitting of 0.47(1) mm/s. The tin dioxide is assumed to have a natural abundance of ^{119}Sn of 8.6%. Due to the "foil" being a powder pressed between two Kapton foils, the thickness is not uniform, which can be seen in the decay pattern by the damped minima. In Fig. 6.3, the decay pattern is fitted with a Gaussian thickness distribution which has a full width at half maximum (FWHM) of 25 µm. The differences of a foil with and without an assumed thickness distribution is shown in Fig. 6.3. Mathematically, the thickness distribution is realized by incoherently summing up the time spectra of different thicknesses weighted by the Gaussian distribution. Since this requires additional computational resources no thickness distribution of the reference foil is assumed for the following analysis of the cavities. It has no effect on the measurement of the collective Lamb shift, since it only damps small features in the combined cavity - reference foil spectrum.

Regarding the Lamb-Mössbauer factor, the tin dioxide reference foil is assumed to have a Lamb-Mössbauer factor of 0.63 and the tin dioxide films of 0.59. Both values originate from nuclear inelastic scattering measurements. The measurement of the reference foil was conducted at P01 by courtesy of Ilya Sergeev. The inelastic measurement on a tin dioxide film was conducted at beamline 30-ID at the APS, where a 3 nm film was embedded in between two magnesium oxide films. The phonon density of states of the reference foil and the tin dioxide film are shown in appendix B.

While the Lamb-Mössbauer factor in thin films can be strongly influenced by the surrounding layers and its thickness, as described in the previous chapter, the variation of the Lamb-Mössbauer factor in the here discussed tin dioxide films can be assumed to be small. The atoms in tin dioxide are covalently bounded. Therefore, the atoms are much stronger bound in contrast to atoms in metallic tin, and thus are more reluctant to diffuse into the surrounding material. Additionally, the adjacent boron carbide was already found to show no noticeable diffusion in the case of metallic tin films. Therefore one can expect that the dynamical behavior of tin dioxide films should not be affected much by the interface to boron carbide and by the layer thickness. A deviation from this assumption would be seen in the nuclear decay, since all other parameters, such as thickness and incident angles, are fixed with a precision of a few percent.

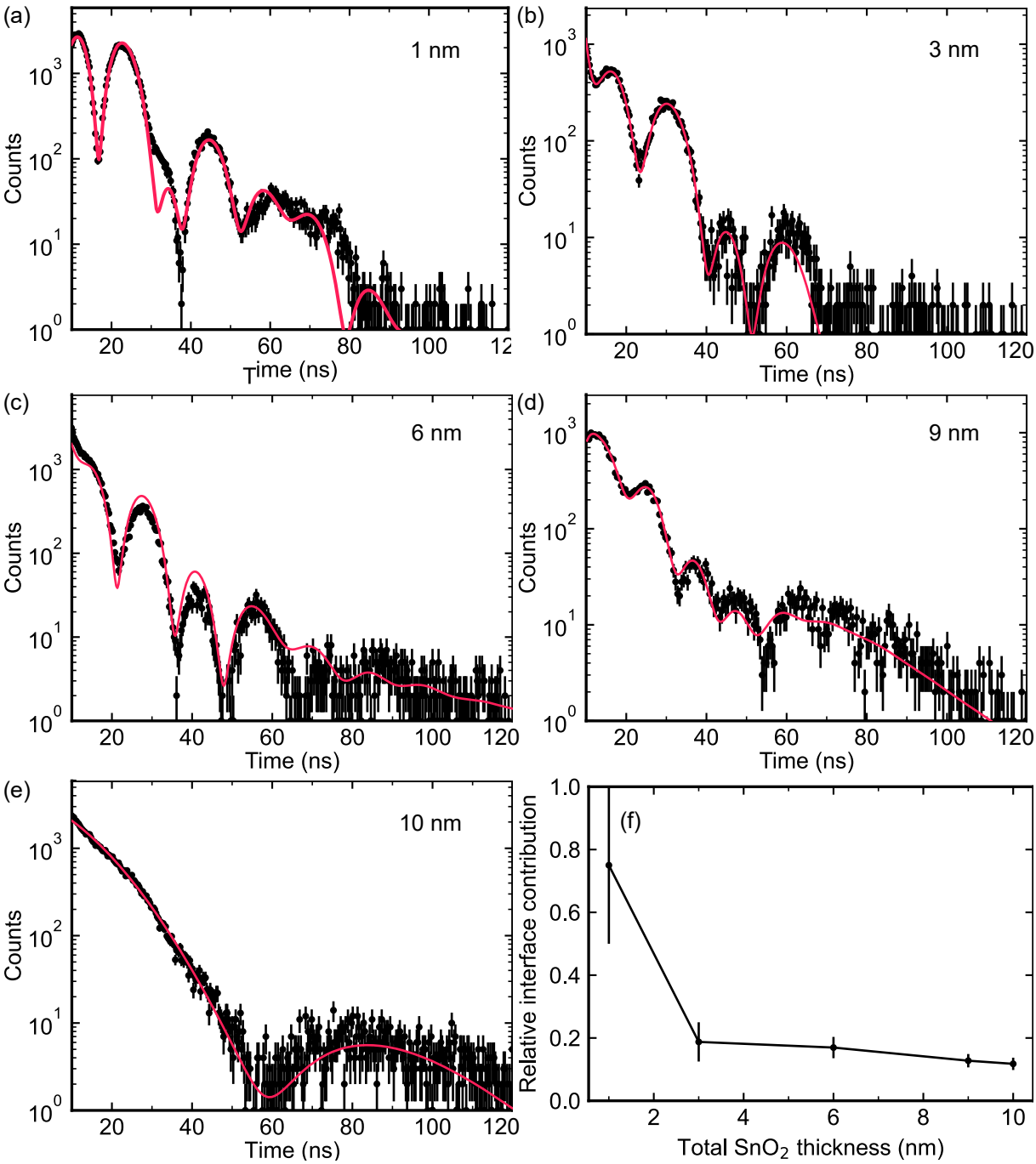

Figure 6.4.: Temporal nuclear decay of the thin film cavities with a SnO_2 layer thickness of (a) 1 nm, (b) 3 nm, (c) 6 nm and (d) 9 nm, as well as the cavity without a guiding layer (e). The fit (red) was done by the software CONUSS. (f) Interface contribution to the hyperfine structure as a function of the tin dioxide layer thickness, derived from the nuclear decay fit.

With the energy spectrum of the reference absorber known, the collective effects on the energy spectrum of the cavities can be investigated. There are two options to measure the energy spectrum of the sample. On the one hand, with the hyperfine parameter obtained via the temporal nuclear decay, the energy spectrum can be calculated. On the other hand, the energy spectrum can be measured by an interferometric setup with a Mössbauer drive as described in section 3.5.1. Here, both options are employed. The temporal decay is used to get information about the tin dioxide layer, which can be used to model the results obtained from the energy-resolved measurements. The combination of both options then leads to a precise measurement of the collective Lamb shift.

In Fig. 6.4, the temporal nuclear decay of all cavities is shown together with a fit obtained by the software CONUSS. Expected is a temporal decay which has a quadrupole beating in combination with dynamical beats due to the superradiant decay. All shown decays, however, have a more complicated beat pattern. It indicates, that not only tin dioxide is present. The fit via the software CONUSS was obtained by assuming an interface layer to the lower boron carbide layer. The complete results of the fits are listed in the appendix A.1.1. The interface layer consists of a combination of tin monooxide and β-Sn and is about 0.5 nm to 1 nm thick. The contribution of the interface to the hyperfine structure as a function of the tin dioxide layer thickness is shown in Fig. 6.4(f) as derived from the nuclear decay fit. The interface layer can be formed during the first steps of the reactive sputtering deposition process, where the first few atomic tin layers might not be fully oxidized. This can be avoided by using a different guiding layer material, which will be discussed later. Combining the cavities with the reference absorber on the Mössbauer drive, a two dimensional measurement is acquired with one axis being the time delay after X-ray pulse excitation and one axis being the Doppler detuned energy of the reference foil on the Mössbauer drive. The two dimensional measurements for all cavities are shown in Fig. 6.5. In the two dimensional plot, a combination of the beat pattern of the temporal nuclear decay of the reference foil, the energy spectrum of the cavity and the interference between them both are visible. The intensity maximum around 40 ns is a good example of this combination. While the intensity maximum originates from the beat pattern of the nuclear decay of the reference foil, see Fig. 6.3, the high frequency pattern as a function of the detuning energy is the interference pattern of the combined temporal response of the cavity-reference foil setup.

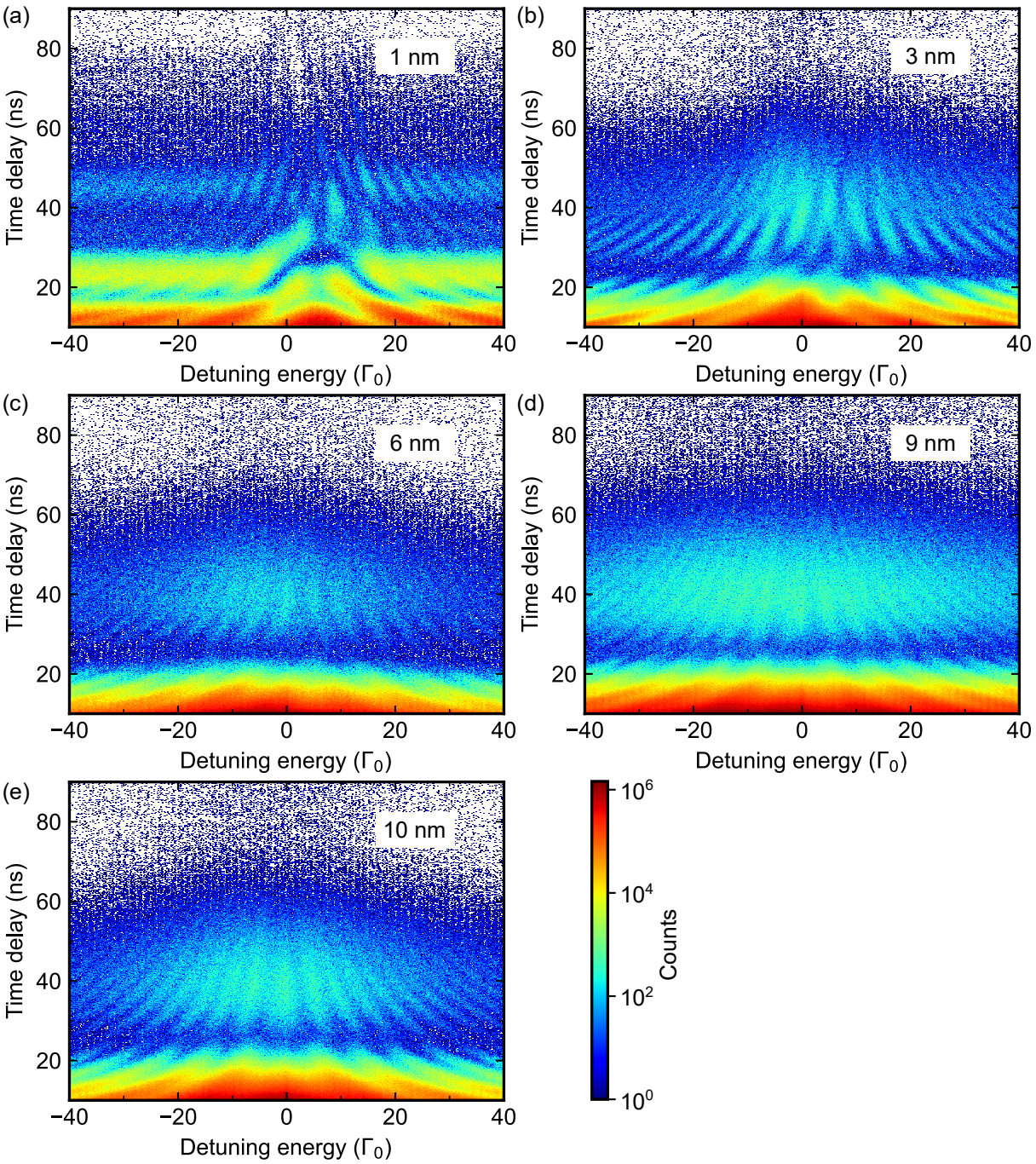

Figure 6.5.: Scattered intensity measured in the setup shown in Fig. 3.8 as a function of the detuning energy of the reference absorber and the time delay after X-ray pulse excitation for the cavities containing a SnO_2 layer with a thickness of (a) 1 nm, (b) 3 nm, (c) 6 nm and (d) 9 nm, as well as for the cavity without a guiding layer (e). The number of measured photons is given in logarithmic scaled colors, see color bar.

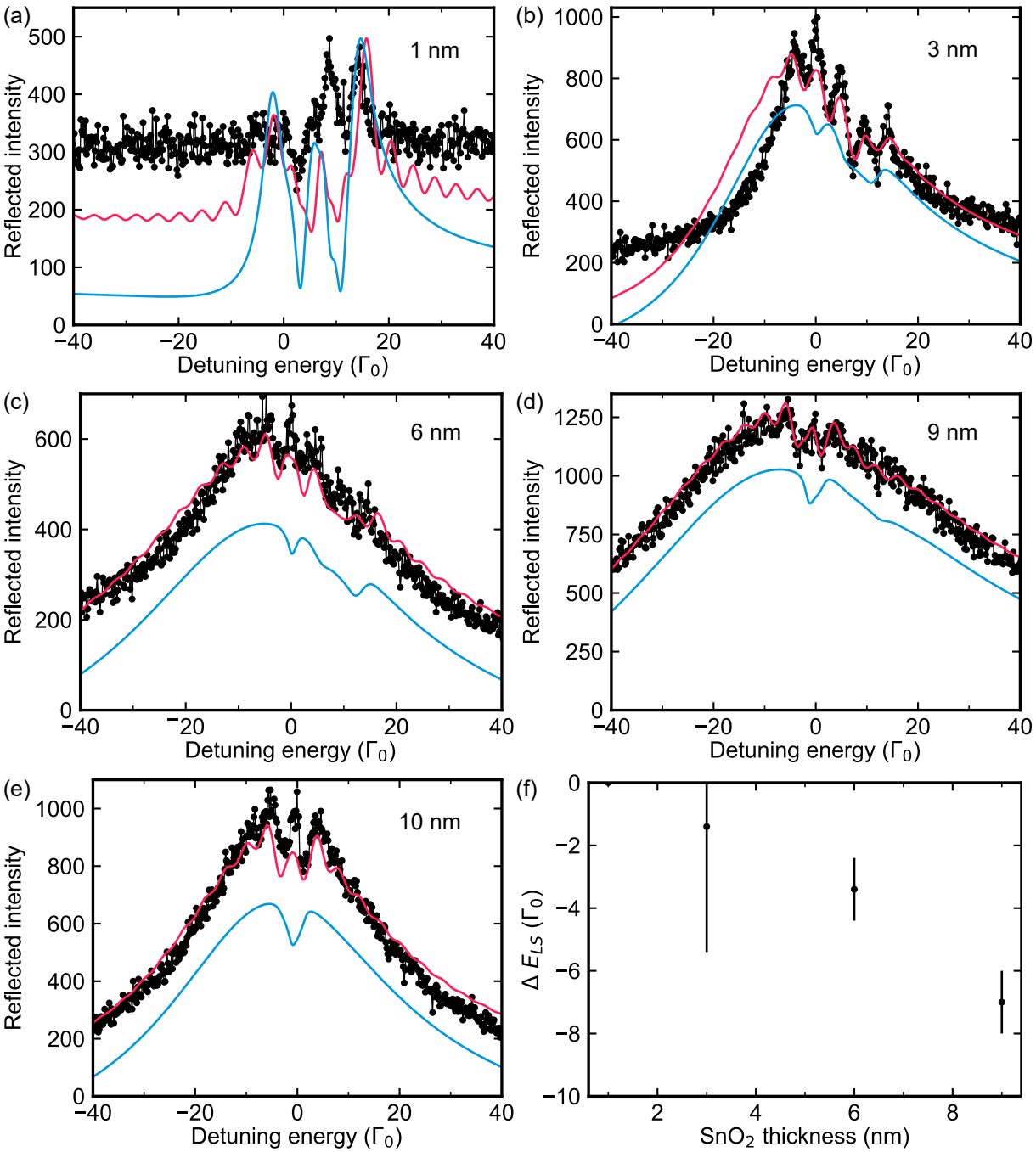

Figure 6.6.: Energy spectra generated by summing all delayed events in the time window from 40 ns to 170 ns for the cavities containing a SnO_2 layer with a thickness of (a) 1 nm, (b) 3 nm, (c) 6 nm and (d) 9 nm embedded in boron carbide, as well as for the cavity without a guiding layer (e). The simulations of the combined response of sample and reference foil (red) are based on the fitted hyperfine parameters of the nuclear decays. The simulated energy spectra of the sample alone (blue) are offset. (f) Derived collective Lamb shift as a function of the tin dioxide layer thickness.

Apart from the high frequency pattern, the energy spectrum at 40 ns closely follows the energy spectrum of the cavity as discussed in section 3.5.2. The spectra get broader with increasing thickness of the tin dioxide layer due to the superradiance. Accompanying the broadening is a small shift of the spectrum to negative energies, the collective Lamb shift. Both collective effects get enhanced with thicker tin dioxide layers. While the described effect is visible from 3 nm to 9 nm tin dioxide films, the cavity with 1 nm tin dioxide behaves unexpected with a strong shift to positive energies and an energy spectrum at around 40 ns with a constant background. As shown in Fig. 6.4(f), the tin dioxide layer below 1 nm consists mainly of tin monooxide and β-Sn. Therefore the energy shift is not related to collective effects but to an isomer shift. The constant background originates from the interaction path where only the reference absorber resonantly interacts with the X-ray pulse. The electronic reflection of the cavity is therefore not strongly enough suppressed.

For the cavity with tin dioxide as a guiding layer, the energy spectrum around 40 ns in Fig. 6.5(e) is broadened as well and has a small shift. However, in comparison to the cavity with guiding layer and a similar tin dioxide layer thickness of 9 nm (Fig. 6.5(d)), the collective effects seem to be decreased. It can be therefore attributed to the lack of field enhancement in the cavity due to the strong electronic absorption in the tin dioxide guiding layer.

When the measurement is integrated over time in a late time window, the derived energy spectrum resembles the energy dependent reflectivity of the cavity at the chosen incidence angle. This is only true if the electronic reflectivity is drastically suppressed in relation to the nuclear response and the spectral features of the cavity are much broader than the natural linewidth. Both assumptions are true in the waveguide minimum for an ideal cavity with a single nuclear transition. Due to the interface layer, however, the hyperfine structure is more complex. Therefore interference are expected also in a late time window.

In Fig. 6.6 the energy spectra are shown, which are generated by summing up the time events in a time window from 40 ns to 170 ns. As expected, the energy spectra are complex in the cases where the tin dioxide layer is thin, see Fig. 6.6(a) and 6.6(b). Here, the impact of the interface layer on the average hyperfine structure, which is seen by the X-ray pulse, is the highest. Interestingly, in the thinnest tin dioxide layer, the energy spectrum is substantially shifted to positive energies. This shift is also generated when

Table 6.2.: Collective Lamb shift, ΔE_{LS}, and superradiant broadening, Γ_S, in units of the natural linewidth of the ^{119}Sn resonance, $\Gamma_0 = 25.3\,\text{neV}$, for the cavities with varying SnO_2 layer thickness. The cavity with the SnO_2 forming the guiding layer is listed as the cavity with 10 nm SnO_2.

SnO_2 thickness (nm)	ΔE_{LS} (Γ_0)	Γ_S (Γ_0)
1	-	-
3	-1.4(4)	20(1)
6	-3.4(1)	44(1)
9	-7(1)	75(5)
10 (SnO_2 as guiding layer)	-2.3(1)	45(1)

the energy response is simulated using the hyperfine structure obtained from the fit of temporal nuclear decay. Therefore, the shift is identical to the isomer shift from tin atoms, which were not fully oxidized during the deposition. It therefore agrees with the findings from the temporal decay pattern.

The energy spectrum of the cavity with 3 nm tin dioxide is affected by the interface as well. Two contributions to the energy spectrum are visible. The isomer shifted interface contribution leads to a strong alteration in the region around $10\Gamma_0$ as already seen in the cavity with 1 nm tin dioxide. Neglecting this part, the second contribution arising from the central part of the layer broadens the energy spectrum significantly. A slight spectral shift to negative energies is noticeable when only the energy region around resonance is considered.

In the thicker layers, the interface contribution vanishes. The spectra are strongly broadened and increasingly shifted to negative energies. This is especially the case for the 9 nm tin dioxide layer cavity, where the spectrum is broadened far beyond the range of the experimental energy detuning. Also the collective Lamb shift is visible by the central weight shift to negative energies. To obtain the superradiant broadening and the collective Lamb shift, each energy spectrum was fitted by a Lorentzian line shape. The results are listed in Tab. 6.2. For the cavity with 3 nm tin dioxide, the region around $10\Gamma_0$ was neglected to reduce the interface contribution.

In summary, the collective Lamb shift increases in the cavities from $1.4\Gamma_0$ (=35 neV) for 3 nm tin dioxide to $7\Gamma_0$ (=177 neV) for 9 nm tin dioxide. The collective Lamb shift as a function of the tin dioxide layer thickness is shown in Fig. 6.6(f). The superradiance

increases as well from $20\Gamma_0$ (=0.5 µeV) to $75\Gamma_0$ (=1.9 µeV). The superradiance leads therefore to an increase of the linewidth from a few nano electronvolt to about 2 µeV.

A collective Lamb shift and a superradiant broadening is also measured in the cavity with tin dioxide as a guiding layer. The layer structure still leads to a small cavity effect which increases the field intensity inside the tin dioxide layer. Therefore, also an enhancement of the collective coupling between the tin nuclei occurs. However, the field intensity is not homogeneously distributed inside the tin dioxide layer, which is why different parts of the layer experience different field intensities. On the one side, this leads to a decrease of the collective coupling strength, since the nuclei are not indistinguishable anymore. On the other side, the electromagnetically induced transparency dip emerges as previously mentioned. This feature, which should arise around zero energy detuning, is slightly visible in the cavity with 9 nm tin dioxide, see Fig. 6.6(d), and is more pronounced in the 10 nm tin dioxide layer without guiding layer, see Fig. 6.6(e). Complete transparency can theoretically be reached [Len20], however, there are not enough tin nuclei in the here presented cavities, also because only every third atom in tin dioxide is tin.

In conclusion, the tin dioxide cavities show an enhancement of the collective effects with increasing tin dioxide layer thickness. A collective Lamb shift of 177 neV and a superradiance of nearly 2 µeV was measured for a cavity containing 9 nm tin dioxide. While the hyperfine structure of the thicker tin dioxide films was nearly unperturbed as desired, the hyperfine structure of the thinner tin dioxide films were strongly distorted by the interface region rendering the measurement of collective effects impossible. Since the hyperfine structure at the interface is strongly dependent on the material combination, as seen in the previous chapter, the results sparked an investigation about an optimization of the hyperfine structure of embedded thin tin dioxide layers. The best embedding found is magnesium oxide.

6.2.1. Tin dioxide in magnesium

The temporal nuclear decay of a 4 nm tin dioxide layer in between two 8 nm magnesium oxide layers is shown in Fig. 6.7. Already visually, the nuclear decay strongly differs from the decay measured for the 3 nm tin dioxide embedded in boron carbide shown in Fig. 6.4(b). Instead of multiple overlapping beats, the nuclear decay of the tin dioxide layer in magnesium oxide exhibits only one beat. The fit by the software CONUSS reveals a

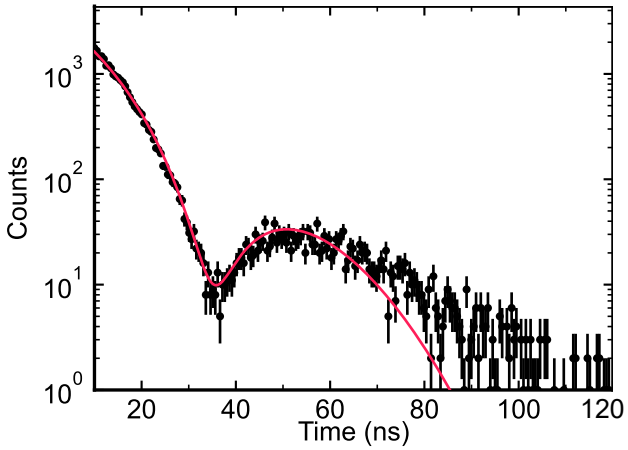

Figure 6.7.: Temporal nuclear decay of 4 nm tin dioxide sandwiched between two magnesium oxide layers each with a thickness of 8 nm.

quadrupole splitting of 0.67(1) mm/s (53(1) neV) which is Gaussian-like distributed with a full width at half maximum of 0.85(1) mm/s (68(1) neV). The obtained quadrupole splitting is therefore close to the quadrupole splitting of bulk tin dioxide, 0.57 mm/s, see Tab. 2.1. Thus, in the interface between tin dioxide and magnesium oxide appears to have no influence on the hyperfine structure. The reason is likely the contact of tin dioxide with an already fully oxidized adjacent material (magnesium oxide).

The combination with magnesium oxide therefore provides a way to fabricate also thin tin dioxide films with a nearly unsplit hyperfine structure. Hence, the tin dioxide films can be prepared in such a way that the hyperfine structure resembles a prototypical two-level quantum state system.

6.3. Tin dioxide layers for nuclear quantum optics

To evaluate tin dioxide layers for applications in nuclear quantum optics experiments, an estimation of achievable effect strengths will be given. Two effects are looked at in more detail: The collective Lamb shift obtained for tin dioxide in comparison to iron and the electromagnetically induced transparency in tin dioxide cavities.

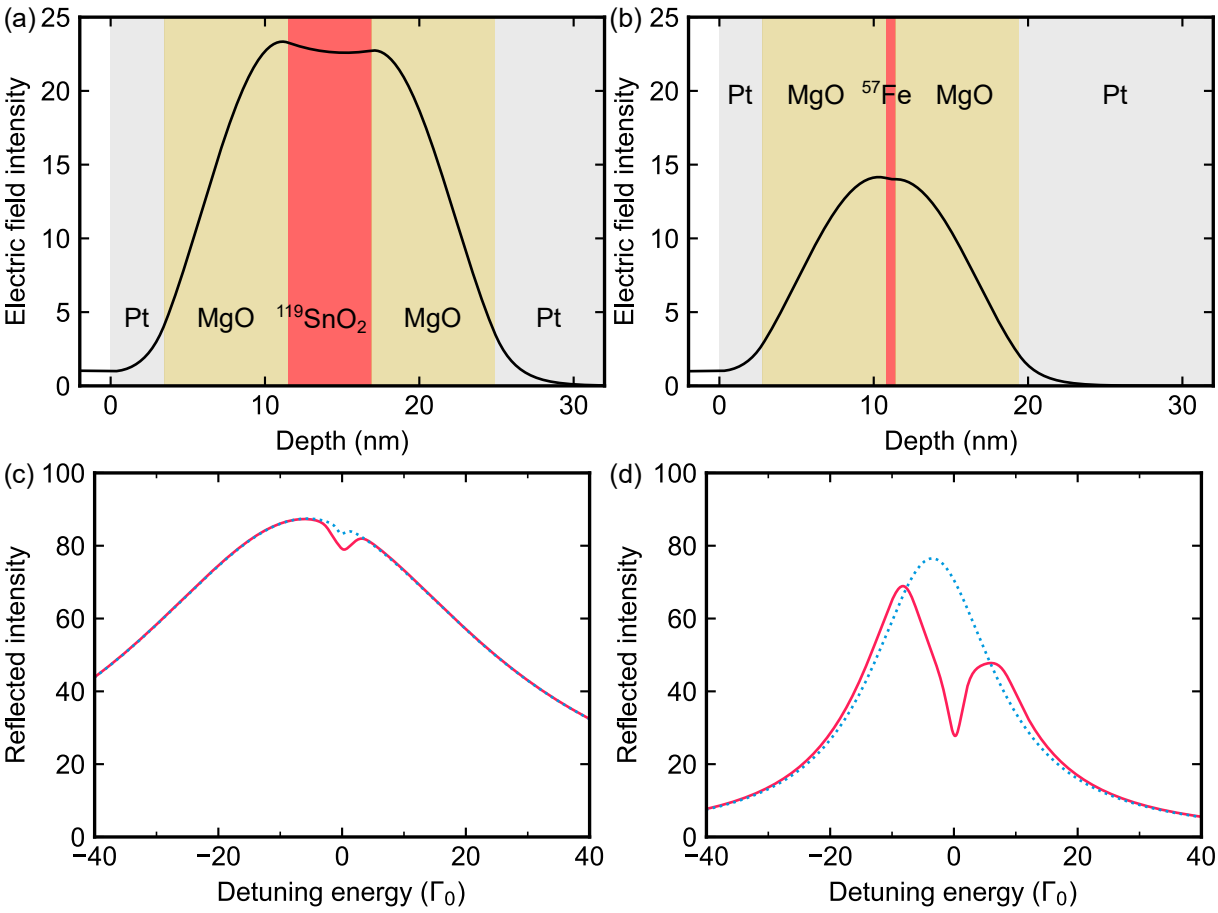

Figure 6.8.: Simulated electric field intensity at the first waveguide mode of a thin film cavity containing tin dioxide (a) and iron (b) where both resonant isotopes have the same areal density. The respective energy spectrum for both cavities resonantly driven at the first waveguide mode is shown for tin dioxide (c) and iron (d). The solid line (red) assumes the hyperfine parameters taken from experiments (see section 6.2 and reference [Röh10]). and the dotted line (blue) assumes no hyperfine interactions.

Comparison of the collective Lamb shift in tin dioxide and iron

For a fair comparison between cavities of different isotopes, the areal number density of the resonant nuclei should be the same. The mass densities of α-Fe and tin dioxide are similar, $7.87\,\mathrm{g/cm^3}$ to $6.95\,\mathrm{g/cm^3}$, however, the iron atom is much lighter than the tin atom. Therefore, there are more iron atoms in a unit weight than tin atoms.

With the areal number density given by the number density times the layer thickness,

it is,

$$\rho_{n,\mathrm{Fe}} d_{\mathrm{Fe}} \stackrel{!}{=} \rho_{n,\mathrm{SnO_2}} d_{\mathrm{SnO_2}} \frac{1}{3} \tag{6.13}$$

$$\frac{\rho_{\mathrm{Fe}}}{M_{\mathrm{Fe}}} N_A d_{\mathrm{Fe}} \stackrel{!}{=} \frac{\rho_{\mathrm{SnO_2}}}{M_{\mathrm{SnO_2}}} N_A d_{\mathrm{SnO_2}} \frac{1}{3}, \tag{6.14}$$

where $\rho_{n,\mathrm{Fe}}$ (ρ_{Fe}) and $\rho_{n,\mathrm{SnO_2}}$ ($\rho_{\mathrm{SnO_2}}$) are the number (mass) density of both materials, M_{Fe} and $M_{\mathrm{SnO_2}}$ the molar mass of both materials, d_{Fe} and $d_{\mathrm{SnO_2}}$ the layer thicknesses of both materials and N_A the Avogadro constant. The factor 1/3 on the tin dioxide side accounts for the fact, that only every third atom is a tin atom in the tin dioxide layer. Thus for an iron layer thickness of 0.6 nm, a thickness chosen by Röhlsberger *et al.* [Röh10] for the detection of the collective Lamb shift, a 5.4 nm thick tin dioxide layer is required to provide the same areal number density.

For the comparison, the material of the guiding layer of the cavity is chosen to be magnesium oxide, since it was found out that this results in a clean hyperfine structure of tin dioxide. The magnesium oxide guiding layer is set to be 16 nm thick in total with the resonant layer being placed in the center. As mirror layers, a 15 nm platinum layer is assumed to be below the guiding layer and above is a platinum layer with a chosen thickness which ensures maximal coupling of the X-rays into the cavity. The assumed X-ray energy in the calculation is set to the respective resonance energy of the chosen isotope.

The calculated electric field intensities inside the first waveguide minimum of the cavity are shown in Figs. 6.8(a) and 6.8(b). While the distortion of the electric field due to the thick tin dioxide layer is visible, the field intensity at the position of the resonant layer is about 1.5 times higher in the tin dioxide cavity than in the iron cavity. The reason is the higher X-ray energy and concomitant lower X-ray absorption. Due to less electronic absorption, the thin film cavity works more effectively at the higher X-ray energy even if the cavity is disturbed by the thick resonant layer.

With the cavity structure simulated, the energy spectrum can be calculated in the first waveguide minimum. The hyperfine parameters of the resonant layer are taken from the experiments. For iron, a quadrupole splitting of 33.8 neV ($= 7.2\Gamma_0$) which is distributed by a Gaussian function with a FWHM of 37.6 neV ($= 8\Gamma_0$) [Röh10] is assumed. The tin dioxide layer has a quadrupole splitting of 53 neV ($= 2.1\Gamma_0$), distributed with a FWHM

of 68 neV ($= 2.7\Gamma_0$). The energy spectra for the cavities are shown in Figs. 6.8(c) and 6.8(d). The strong quadrupole splitting in the iron layer leads to a strongly disturbed energy spectrum, while the spectrum in the tin dioxide case is cleaner. For the iron cavity, a resonance linewidth of $24\,\Gamma_0$ and a collective Lamb shift of -3.5 Γ_0 is obtained, while for nuclear resonance of the tin cavity has a linewidth of $70\,\Gamma_0$ and an energy shift of -5.4 Γ_0. Thus, the superradiant broadening is increased by nearly a factor of nearly three, while the collective Lamb shift is increased by a factor of 1.5. The increase of the collective Lamb shift is by the same factor as found for the field enhancement in the cavities. Thus, the increase of the collective effect strength in tin dioxide layers mainly originates from the decrease of electronic absorption at the higher resonance energy. Moreover, the requirement of an increased tin dioxide layer thickness to equal the areal number densities of tin dioxide and iron has no impact on the collective effect strengths presumably because the field distribution in the tin dioxide layer is nearly constant, as shown in Fig. 6.8(a). Under the discussed conditions, tin dioxide layers provide a prototypical two-level quantum system which is ideal for the investigation of quantum optics effect such as the collective Lamb shift.

Electromagnetically induced transparency

The constant field distribution within the tin dioxide layer is an important requirement to measure collective effects. Deviations from an ideal homogeneous field distribution result in a dip feature at exact resonance as previously seen in the thick tin dioxide layer. This effect can be enhanced by using two resonant layers in the cavity combined with an excitation of a higher order waveguide mode rendering the cavity completely transparent at resonance [Röh12]. This effect is called electromagnetically induced transparency (EIT).

The standing wave field of a higher order waveguide mode exhibits regions where the standing wave field is nearly zero (nodes) and regions where the field is strongly enhanced (antinodes). By placing a resonant layer at a node position of the standing wave field and a second layer at an antinode position, the two layers experience completely different photonic densities. While the layer at the antinode position couples strongly to the radiation leading to a superradiant decay with the linewidth Γ_S, the layer at the node position is only weakly excited and thus decays with the natural linewidth Γ_0. Since $\Gamma_S \gg \Gamma_0$, the resonance of the layer at the node position can be considered as metastable

rendering the cavity an effective three-level quantum system: The ground state $|1\rangle$, the excited metastable state $|2\rangle$ and the excited superradiantly broadened state $|3\rangle$. Moreover, the excited states are coupled by the exchange of virtual photons. The same mechanism led to the emergence of the collective Lamb shift, however in that case, the virtual photons couple atoms within the same layer. Here, the two separate layers interact with each other through the cavity. Thus, if the cavity is excited by an X-ray pulse, the system will decay via state $|3\rangle$, since state $|2\rangle$ can be considered metastable. However, the coupling between both excited states leads to quantum interferences between possible decay paths and can lead to a deconstructive interference at exact resonance, the EIT effect [Röh12].

The coupling between the excites states can be described by a control field driving the transition between states $|2\rangle$ and $|3\rangle$ with Rabi frequency Ω_C. Within the formalism of the transfer matrix and the ultrathin film approximation, the Rabi frequency is given by, [Röh12]

$$|\Omega_C| = f_0 \rho_n d |q_1 p_2| \,, \tag{6.15}$$

where $d = \sqrt{d_1 d_2}$ with d_1 and d_2 being the thickness of the two resonant layer. The nuclear parameters f_0 are as defined by Eq. 6.8 and the field amplitudes q_1 at the first resonant layer and p_2 at the second resonant layer are as previously defined, see Eq. 6.12.

For the appearance of the EIT feature, the Rabi frequency must be high enough to overcome decoherence effects like the spontaneous decay of state $|2\rangle$ or $|3\rangle$, i.e. $|\Omega_C|^2 > \Gamma_0 \Gamma_S$ [Röh12]. According to Eq. 6.15, a high Rabi frequency is achieved by a high areal number density $\rho_n d$ and a strong field enhancement.

An example for tin dioxide is calculated in Fig. 6.9. The cavity structure consists of a 32 nm thick magnesium oxide as a guiding layer in between two platinum layers and is resonantly excited at the third waveguide mode. Two tin dioxide layer, which are each 5 nm thick, are positioned at the node and antinode position of the standing wavefield. The field distribution inside the cavity is shown in Fig. 6.9(a). Since the maxima of the standing wave field are sharper in the third waveguide mode than in the first waveguide mode, exemplary shown in Fig. 6.8(a), the field varies considerable inside the tin dioxide layer. The energy spectrum of the cavity excited at the third waveguide mode is shown in Fig. 6.9(b) with a hyperfine structure absent of any splittings (blue) and with the hyperfine parameters as obtained from tin dioxide films embedded in magnesium oxide (red). While a dip is clearly visible at resonance, transparency is not reached indicating

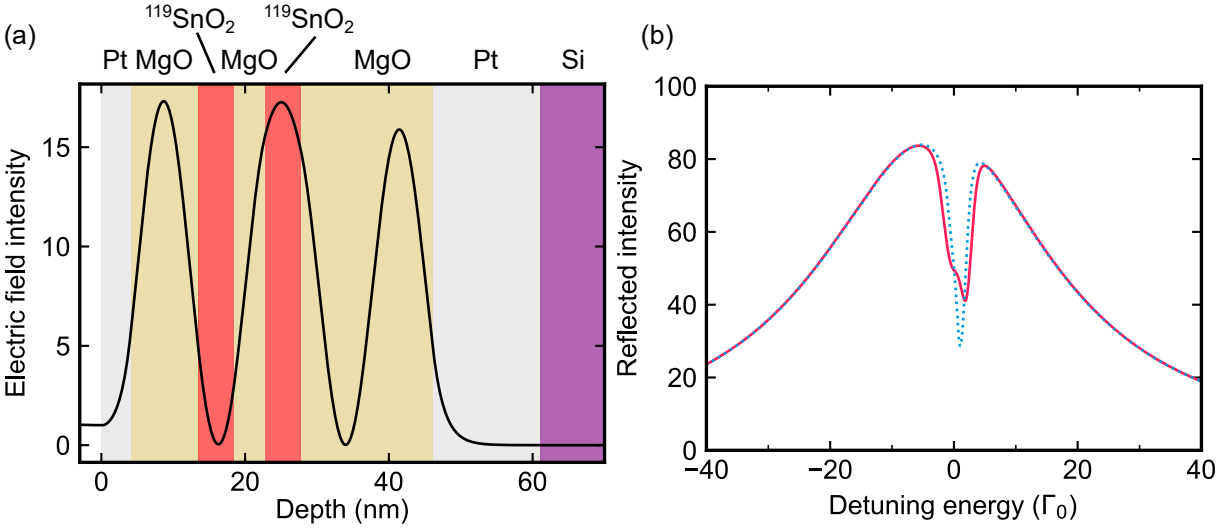

Figure 6.9.: (a) Electric field intensity inside a cavity consisting of: 15 nm Pt/ 18.3 nm MgO/ 5 nm $^{119}SnO_2$/ 4.3 nm MgO/ 5 nm $^{119}SnO_2$/ 9.4 nm MgO/4.1 nm Pt. The cavity is excited at the third waveguide mode. (b) Energy dependent reflectivity of the cavity excited at the third waveguide mode assuming no hyperfine splitting (blue) and with the experimentally obtained hyperfine parameters for tin dioxide layers (red).

that the Rabi frequency, thus the coupling between the two layers, is too weak. With Eq. 6.15, a Rabi frequency of this caviy system of about $6\,\Gamma_0$ is obtained, while the superradiant decay width Γ_S using Eq. 6.8 is about $40\,\Gamma_0$, thus $\Omega_C^2 \approx \Gamma_S\Gamma_0$. The Rabi frequency is therefore not strong enough to overcome decoherence effects arising from the spontaneous decay of the system.

The reason for the weak coupling is a low areal density. The 5 nm of tin dioxide corresponds to the same areal density of a 0.6 nm iron film. However, even with iron, an appreciable EIT effect is only visible for iron layer thicknesses above 2 nm [Röh12]. An increase of the tin dioxide layer thickness, however, leads to a strong distortion of the standing wave field, especially in the higher order waveguide modes, and thus to a decrease of the field enhancement. Thus, the observation of complete transparency at resonance appears to be not possible with tin dioxide layers.

The comparison of the collective Lamb shift in tin dioxide and iron cavities and the estimation of the EIT effect strength show the strong but also the weak points of tin dioxide layers in nuclear quantum optics experiments. The nearly unsplit hyperfine structure allows a clear detection of spectral features without any magnetic contribution due to a

magnetic hyperfine field. Moreover, an increase in the field enhancement inside the cavity becomes possible due to a lower electronic absorption. Especially applications using multilayer structures, where a deep penetration into the layer structure is desired, the low absorption is beneficial [Hab16]. The effect strengths, however, are limited due to the low number density of resonant tin nuclei in tin dioxide. Relatively thick tin dioxide layers are therefore required which can perturb the standing wave field of the cavity, especially at higher order waveguide modes. With an embedded metallic tin layer, which has an increased Lamb-Mössbauer factor and no split hyperfine structure, the number density could be increased by a factor of three. Such an embedded tin layer, however, is still not found, even though the engineering of the thermodynamic properties presented in the previous chapter paves the way to find such an embedded tin layer.

7. Conclusion

The structural, vibrational and nuclear properties of thin tin and tin dioxide films were studied with the goal to understand photon-nuclei interactions at the nuclear resonance of ^{119}Sn.

It was shown that smooth tin films can be prepared when the substrate is cooled down to below $-100\,°C$ during deposition. The tin films have a roughness of below 1 nm and are arranged in the β-Sn crystal phase. The tin crystallites in the film are of a comparable size as the film thickness. Nuclear resonance scattering experiments reveal that a thick tin film of about 20 nm behaves as expected for a β-Sn film and is sensitive to an external magnetic field of at least 250 mT and magnetic field changes of 20 mT. When the tin film thickness is decreased to 7 nm, the hyperfine structure of the tin film is distorted, which was attributed to an interface layer to the adjacent tantalum layer with a thickness of about 1 nm.

The interface is the key to engineer the thermodynamic properties of tin films. The phonon density of states of the tin films embedded in different materials with a varying thickness is revealed. A correlation between the thermodynamic behavior of the adjacent material and of the first 1.5 nm of the tin layer was found. In the most cases, this leads to a thermodynamically harder tin layer. For example, the Lamb-Mössbauer factor of tin inside permalloy is increased from a bulk value of 0.04 to 0.33. The origin of the hardening effect is attributed to interlayer diffusion. The diffusion is especially enhanced when tin forms intermetallic compounds with the adjacent material. In an amorphous environment, however, nearly no diffusion is possible and the thermodynamic behavior of the tin film resembles the expected β-tin behavior. In conclusion, the thermodynamic properties of ultra thin tin films, $\leq$2 nm, can be engineered by the surrounding material. Since the vibrational behavior, and especially the Lamb-Mössbauer factor of the tin plays an important role for nuclear resonance scattering, it allows to tune the interaction strength between the tin layer and the X-ray pulse.

Since the increased hardness of embedded metallic tin films led to a perturbed tin hyperfine structure, stannic oxide (SnO_2) films were employed for nuclear quantum optics. Nuclear inelastic scattering confirmed that the Lamb Mössbauer factor of tin dioxide is even in thin films (3 nm) of similar strength as in bulk, with 0.59 in the thin film in comparison to 0.63 in bulk. The thickness dependent collective Lamb shift and superradiant broadening were measured with a shift of 35 neV and a broadening of 0.5 µeV in the 3 nm tin dioxide cavity to a shift of 177 neV and a broadening of 1.9 µeV in the 9 nm tin dioxide cavity. The hyperfine structure of the tin dioxide exhibits distortions due to the interface with boron carbide. Thus, the obtained energy spectra of the cavity are perturbed in the case of thin tin dioxide layers. However, for thick tin dioxide cavities, the energy spectra are without any distortion exhibiting a clean hyperfine structure. Further going experiments showed that by preparing the tin dioxide layer in between magnesium oxide, which is a suitable material for nuclear quantum optics, the hyperfine structure is clean even for thin tin dioxide films. Thus, the hyperfine structure is a nearly prototypical two-level quantum state system. This is highly desired for nuclear quantum optics.

The results show that the thermodynamic properties and hyperfine structures of tin and tin dioxide thin films can be controlled and engineered. For example, this renders the detection of spin currents inside nanostructures by thin tin films possible as laid out in section 4.3. By employing ultrathin tin films, the propagation of the spin currents can also be probed in a spatially resolved manner. Moreover, even though the engineering of the thermodynamic behavior did not lead to an embedded tin film system usable for nuclear quantum optics, the high degree of tunability of thermodynamic parameters can be used to tune the thermal conductivity for thermoelectrical applications or the design of possible phonon-photon cavities for the investigation of phonon-photon interactions.

For nuclear quantum optics, the properties of stannic oxide films are beneficial in experiments were an unsplit hyperfine structure, low electronic absorption and strong field enhancements inside a thin film cavity are required as shown in section 6.3. Limits on the effect strength are imposed due to the relatively low number density of the resonant nuclei in comparison to iron. Thus, tin dioxide layers are complimentary to iron films: In experiments, where ultrathin films are needed, iron layers are the better choice, whereas in experiments with thicker films or where the thickness is not as relevant, tin dioxide layers provide more benefits. For example in nuclear optical lattices, the combination of low electronic absorption and a clean hyperfine structure could allow the observation

of fully formed bandgaps [Hab16]. In conclusion, the obtained results show the strength and limits of tin dioxide films in nuclear quantum optics experiments and thus lay the foundation for extending nuclear quantum optics to the 23.88 keV resonance energy of ^{119}Sn.

Appendix A.

Sample characterization results

A.1. Fit results for the thin film cavities

A.1.1. Reflectivity fit results

In the following, the results of the fit of the reflectivity measurements shown in Fig. 6.2 are given. For the fitting procedure, both boron carbide layers are assumed to have equal thicknesses, which means that the tin dioxide layer is placed exactly in the center of the cavity. In the electronic reflectivity, deviations from the center positions cannot be measured, since the reflectivity looks the same for all cases. However, deviations are visible in the nuclear reflectivity. The measured nuclear reflectivities show that the tin dioxide layers is in the center of the cavity.

In order to fit the reflectivity measurements, an additional layer between platinum and silicon needs to be included with a lower density than platinum. From the presented measurements, the origin cannot be derived. Possible effects are diffusion of platinum into silicon or a porous growth of the first platinum layers. The porous growth can be triggered by organic residuals from the cleaning procedure with acetone and isopropanol or by a thin water film, which is always present on top of the silicon substrate. Diffusion of platinum on a silicon substrate is possible at elevated temperature ($\approx 200\,^{\circ}\mathrm{C}$), [Shi00], which might be reached due to the radio frequency sputtering of boron carbide for an extended time (since the sputtering rate of boron carbide is low). The silicon substrates used in this work have a native oxide layer on top, about 1 nm to 5 nm, which should prevent any diffusion. However, due to the low thickness of the oxide layer, diffusion cannot be excluded. This platinum layer of lower density, however, does not affect the

Table A.1.: Fit parameters of the reflectivity shown in Fig. 6.2(a) for the cavity with nominal 1 nm SnO_2.

Layer material	Thickness (nm)	Density (g/cm^3)	Roughness (nm)
Pt	3.3	21.4	0.8
B_4C	7.8	2.5	0.2
SnO_2	0.8	5.3	0.1
B_4C	7.8	2.4	0.4
Pt	14.1	20.2	0.7
PtSi	5.1	12.4	0.2

Table A.2.: Fit parameters of the reflectivity shown in Fig. 6.2(b) for the cavity with nominal 3 nm SnO_2.

Layer material	Thickness (nm)	Density (g/cm^3)	Roughness (nm)
Pt	3.5	21.2	0.6
B_4C	8.6	2.1	0.8
SnO_2	3.2	5.9	0.8
B_4C	8.6	2.5	0.2
Pt	14.1	21.2	0.7
PtSi	4.9	11.6	0.0

measurement of the collective Lamb shift. The collective Lamb shift is measured in the first waveguide mode of the cavity, meaning at an incidence angle of about 0.1°. At these low angles, the radiation is completely reflected by the 14 nm platinum layer, which means that the radiation does not reach the platinum layer of lower density. Therefore, it cannot affect the measurement.

A.1.2. Fit results of nuclear decays

In the Tabs. A.6, A.7, A.8 and A.9 the results from fitting the temporal decay patterns, which are shown in Fig. 6.4, are listed. For the fit, an interface layer was needed to be included. It is assumed to have a tin monoxide like and a β-Sn like site. The reason is the measured isomer shift in the energy spectrum of the cavity with a nominal 1 nm thick tin oxide layer, which is close to the isomer shifts given in literature for SnO and β-Sn, see Tab. 2.1.

Table A.3.: Fit parameters of the reflectivity shown in Fig. 6.2(c) for the cavity with nominal 6 nm SnO_2.

Layer material	Thickness (nm)	Density (g/cm^3)	Roughness (nm)
Pt	3.6	21.4	0.6
B_4C	7.4	2.5	1.0
SnO_2	5.9	7.0	0.3
B_4C	7.4	2.5	0.0
Pt	14.2	20.8	0.6
PtSi	4.8	11.2	0.0

Table A.4.: Fit parameters of the reflectivity shown in Fig. 6.2(d) for the cavity with nominal 9 nm SnO_2.

Layer material	Thickness (nm)	Density (g/cm^3)	Roughness (nm)
Pt	3.5	20.7	0.5
B_4C	7.9	2.5	0.1
SnO_2	9.4	6.9	1.3
B_4C	7.9	2.5	1.0
Pt	14.1	20.0	0.6
PtSi	4.7	10.0	0.0

Table A.5.: Fit parameters of the reflectivity shown in Fig. 6.2(e) for the cavity without a guiding layer and nominal 10 nm SnO_2.

Layer material	Thickness (nm)	Density (g/cm^3)	Roughness (nm)
Pt	4.1	21.4	0.5
SnO_2	10.2	6.8	0.4
Pt	13.3	21.4	0.6
PtSi	4.5	11.2	0.1

Table A.6.: Fit parameters of the temporal decay pattern shown in Fig. 6.4(a) for the cavity containing 1 nm SnO_2. Parameters marked with an asterisk symbol (*) are kept fixed. For energy conversion: 1 mm/s ≙ 79.6 neV.

Parameter	**Fit result**
Incidence angle	1.784 mrad
Thickness SnO_2 layer	0.2(1) nm
Quadrupole splitting	0.62(1) mm/s
FWHM isomer shift	0.63(1) mm/s
Thickness interface layer	0.6(2) nm
Weight SnO-like site	84.9(1)%
Isomer shift	2.80(1) mm/s
Quadrupole Splitting	2.33(1) mm/s
FWHM isomer shift	0.62(1) mm/s
Weight β-Sn-like site	15.1(1)%
Isomer shift*	2.56 mm/s
Quadrupole Splitting	0.70(2) mm/s
FWHM isomer shift	0.24(1) mm/s

Table A.7.: Fit parameters of the temporal decay pattern shown in Fig. 6.4(b) for the cavity containing 3 nm SnO_2. Parameters marked with an asterisk symbol (*) are kept fixed. For energy conversion: 1 mm/s ≙ 79.6 neV.

Parameter	**Fit result**
Incidence angle	1.767 mrad
Thickness SnO_2 layer	2.6(2) nm
Quadrupole splitting	0.64(1) mm/s
FWHM isomer shift	0.33(1) mm/s
Thickness interface layer	0.6(2) nm
Weight SnO-like site	28.4(5)%
Isomer shift	2.73(1) mm/s
Quadrupole Splitting	1.77(1) mm/s
FWHM isomer shift	0.58(1) mm/s
Weight β-Sn-like site	71.6(5)%
Isomer shift*	2.56 mm/s
Quadrupole Splitting*	0.28 mm/s
FWHM isomer shift	2.09(1) mm/s

Table A.8.: Fit parameters of the temporal decay pattern shown in Fig. 6.4(c) for the cavity containing 6 nm SnO_2. Parameters marked with an asterisk symbol (*) are kept fixed. For energy conversion: 1 mm/s ≙ 79.6 neV.

Parameter	**Fit result**
Incidence angle	1.957 mrad
Thickness SnO_2 layer	4.9(2) nm
Quadrupole splitting	0.68(1) mm/s
FWHM isomer shift	0.01(1) mm/s
Thickness interface layer	1.0(2) nm
Weight SnO-like site	42.2(5)%
Isomer shift	2.95(1) mm/s
Quadrupole Splitting	2.19(1) mm/s
FWHM isomer shift	0.71(1) mm/s
Weight β-Sn-like site	57.8(5)%
Isomer shift*	2.56 mm/s
Quadrupole Splitting*	0.28 mm/s
FWHM isomer shift	2.34(1) mm/s

Table A.9.: Fit parameters of the temporal decay pattern shown in Fig. 6.4(d) for the cavity containing 9 nm SnO_2. Parameters marked with an asterisk symbol (*) are kept fixed. For energy conversion: 1 mm/s ≙ 79.6 neV.

Parameter	**Fit result**
Incidence angle	1.954 mrad
Thickness SnO_2 layer	8.2(2) nm
Quadrupole splitting	0.47(1) mm/s
FWHM isomer shift	0.30(1) mm/s
Thickness interface layer	1.2(2) nm
Weight SnO-like site	13.0(5)%
Isomer shift	3.10(1) mm/s
Quadrupole Splitting	1.95(1) mm/s
FWHM isomer shift	0.72(1) mm/s
Weight β-Sn-like site	87.0(5)%
Isomer shift*	2.56 mm/s
Quadrupole Splitting*	0.28 mm/s
FWHM isomer shift	4.67(1) mm/s

Table A.10.: Fit parameters of the temporal decay pattern shown in Fig. 6.4(e) for the cavity without a guiding layer containing 10 nm SnO_2. Parameters marked with an asterisk symbol (*) are kept fixed. For energy conversion: 1 mm/s ≙ 79.6 neV.

Parameter	**Fit result**
Incidence angle	1.954 mrad
Thickness SnO_2 layer	9.0(2) nm
Quadrupole splitting	0.38(1) mm/s
FWHM isomer shift	0.234(1) mm/s
Thickness interface layer	1.2(2) nm
Isomer shift*	0 mm/s
Quadrupole Splitting	1.27(1) mm/s
FWHM isomer shift	0.33(1) mm/s

Appendix B.

Nuclear inelastic scattering on tin dioxide

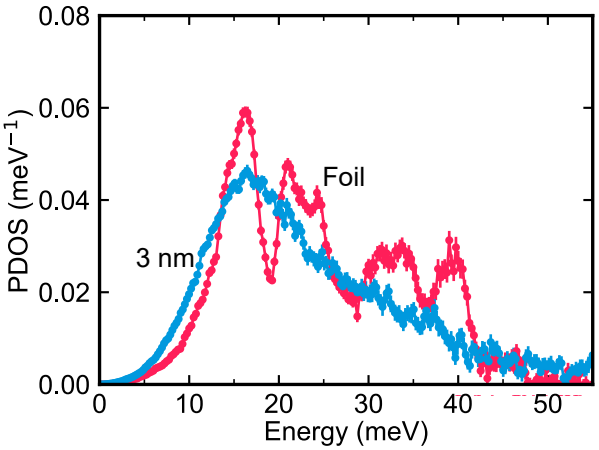

Figure B.1.: Phonon density of states of a tin dioxide foil, consisting of pressed powder, (red) and a 3 nm tin dioxide film embedded in magnesium oxide (blue).

Nuclear inelastic scattering experiments on a tin dioxide foil and a tin dioxide thin film was performed at P01 (foil) and at APS (thin film). The data for the tin dioxide foil is provided by courtesy of Ilya Sergeev. Both experiments were conducted at room temperature. The tin dioxide film is embedded in a thin film cavity structure consisting of 15 nm platinum, 5 nm magnesium oxide, 3.2 nm tin dioxide, 5 nm magnesium oxide and 3.2 nm platinum, prepared in this order on a sapphire substrate. All layers are prepared by sputter deposition and the tin dioxide layer is prepared as described in section 3.2. The tin dioxide consists of isotopically enriched ^{119}Sn material. The inelastic measurement of

the thin film was conducted at the incidence angle with the highest inelastic signal, which is at the angle of the waveguide mode of the cavity structure.

The resulting phonon density of states for the foil and the thin film is shown in Fig. B.1. An analysis of the phonon density of states in combination with the nuclear inelastic spectra provides a Lamb-Mössbauer factor of 0.630(3) for the tin dioxide foil and 0.590(3) for the 3 nm tin dioxide film.

Appendix C.

Publications

C.1. Conference contributions

This is a list of conference content the author of this work has contributed to. The presenting author is underlined.

Contributed Talk S. Velten, L. Bocklage, K. Schlage, J. Gollwitzer, A. Siemens, I. Sergeev, O. Leopold, H.C. Wille, R. Reddy, and R. Röhlsberger, "Hyperfine interactions in ultra-thin β-Sn layers probed via nuclear resonance scattering ", Hyperfine Conference, Goa, India (2019)

Poster Presentation S. Velten, L. Bocklage, D. Lentrodt, K.P. Heeg, J. Gollwitzer, K. Schlage, I. Sergeev, H.C. Wille, J. Evers, and R. Röhlsberger, "Hyperfine interactions in ^{119}Sn films probed via nuclear resonance scattering", International Conference on the Applications of the Mössbauer Effect, Dalian, China (2019)

Poster Presentation S. Velten, L. Bocklage, D. Lentrodt, K.P. Heeg, J. Gollwitzer, K. Schlage, I. Sergeev, H.C. Wille, J. Evers, and R. Röhlsberger, "Hyperfine interactions in ^{119}Sn films probed via nuclear resonance scattering" Photon Science User Meeting, Hamburg (2020)

Poster Presentation S. Velten, L. Bocklage, D. Lentrodt, K.P. Heeg, J. Gollwitzer, K. Schlage, I. Sergeev, H.C. Wille, J. Evers, and R. Röhlsberger, "Phonon confinement in ultrathin Sn layers", DESY NanoMat Day, Hamburg (2020)

C.2. Papers in related projects

Publications in peer-reviewed journals in related projects:

- A.-L. Calendron, J. Meier, E. Kueny, S. Velten, L. Bocklage, R. Röhlsberger, and F. X. Kärtner, "Bulk, cascaded pulse compression scheme and its application to spin emitter characterization",
  Applied Optics **60**, 912-917 (2021)
  DOI: 10.1364/AO.412177

Bibliography

[Aba19] G. Abadias, J. J. Colin, D. Tingaud, P. Djemia, L. Belliard, and C. Tromas. "Elastic properties of α-and β-tantalum thin films".
Thin Solid Films **688**, 137403 (2019).
DOI: 10.1016/j.tsf.2019.06.053.

[Ada06] J. J. Adams, D. Agosta, R. G. Leisure, and H. Ledbetter. "Elastic constants of monocrystal iron from 3 to 500 K".
Journal of Applied Physics **100**, 113530 (2006).
DOI: 10.1063/1.2365714.

[All76] P. S. Allen. "Internal hyperfine fields in magnetic solids".
Contemporary Physics **17**, 387–402 (1976).
DOI: 10.1080/00107517608224050.

[Bar00] A. Barla, R. Rüffer, A. I. Chumakov, J. Metge, J. Plessel, and M. M. Abd-Elmeguid. "Direct determination of the phonon density of states in β- Sn".
Physical Review B **61**, R14881 (2000).
DOI: 10.1103/PhysRevB.61.R14881.

[Bis12] K. Biswas, J. He, I. D. Blum, C.-I. Wu, T. P. Hogan, D. N. Seidman, V. P. Dravid, and M. G. Kanatzidis. "High-performance bulk thermoelectrics with all-scale hierarchical architectures".
Nature **489**, 414–418 (2012).
DOI: 10.1038/nature11439.

[Blo53] N. Bloembergen and T. J. Rowland. "On the nuclear magnetic resonance in metals and alloys".
Acta Metallurgica **1**, 731–746 (1953).
DOI: 10.1016/0001-6160(53)90033-9.

[Boc15] L. Bocklage, C. Swoboda, K. Schlage, H.-C. Wille, L. Dzemiantsova, S. Bajt, G. Meier, and R. Röhlsberger. "Spin precession mapping at ferromagnetic resonance via nuclear resonant scattering of synchrotron radiation".
Physical Review Letters **114**, 147601 (2015).
DOI: 10.1103/PhysRevLett.114.147601.

[Boc66] J.-P. Bocquet, Y. Y. Chu, O. C. Kistner, M. L. Perlman, and G. T. Emery. "Chemical Effect on Outer-Shell Internal Conversion in Sn^{119}; Interpretation of the Mössbauer Isomer Shift in Tin".
Phys. Rev. Lett. **17**, 809–813 (15 1966).
DOI: 10.1103/PhysRevLett.17.809.

[Boc68] J.-P. Bocquet, Y. Y. Chu, G. T. Emery, and M. L. Perlman. "Internal-conversion studies with ^{119m}Sn and ^{117m}Sn." (1968).
DOI: 10.1103/PhysRev.167.1117.

[Boz16] D. Bozyigit, N. Yazdani, M. Yarema, O. Yarema, W. M. M. Lin, S. Volk, K. Vuttivorakulchai, M. Luisier, F. Juranyi, and V. Wood. "Soft surfaces of nanomaterials enable strong phonon interactions".
Nature **531**, 618–622 (2016).
DOI: 10.1038/nature16977.

[Bra02] A. Brataas, Y. Tserkovnyak, G. E. W. Bauer, and B. I. Halperin. "Spin battery operated by ferromagnetic resonance".
Physical Review B **66**, 060404 (2002).
DOI: 10.1103/PhysRevB.66.060404.

[Buc52] W. Buckel and R. Hilsch. "Supraleitung und Widerstand von Zinn mit Gitterstörungen".
Zeitschrift für Physik **131**, 420–442 (1952).
DOI: 10.1007/BF01329552.

[Cha13] M. Chamas, M.-T. Sougrati, C. Reibel, and P.-E. Lippens. "Quantitative analysis of the initial restructuring step of nanostructured FeSn2-based anodes for Li-ion batteries".
Chemistry of Materials **25**, 2410–2420 (2013).
DOI: 10.1021/cm400253a.

[Chu97] A. I. Chumakov, R. Rüffer, A.Q.R. Baron, H. Grünsteudel, H.F. Grünsteudel, and V.G. Kohn. "Anisotropic inelastic nuclear absorption".
Physical Review B **56**, 10758 (1997).
DOI: 10.1103/PhysRevB.56.10758.

[Chu99] A. I. Chumakov and W. Sturhahn. "Experimental aspects of inelastic nuclear resonance scattering".
Hyperfine interactions **123**, 781–808 (1999).
DOI: 10.1023/A:1017052730094.

[CON] CONUSS. *Version 2.2.0 by W. Sturhahn.* http://www.nrixs.com.

[Cue01] B. R. Cuenya, W. Keune, W. Sturhahn, T.S. Toellner, and M.Y. Hu. "Structure and vibrational dynamics of interfacial Sn layers in Sn/Si multilayers".
Physical Review B **64**, 235321 (2001).
DOI: 10.1103/PhysRevB.64.235321.

[CXR] CXRO. *Center for X-ray optics.* https://henke.lbl.gov/optical_constants/asf.html.

[Del15] O. Delaire, I. I. Al-Qasir, A. F. May, C. W. Li, B. C. Sales, J. L. Niedziela, J. Ma, M. Matsuda, D. L. Abernathy, and T. Berlijn. "Heavy-impurity resonance, hybridization, and phonon spectral functions in $Fe_{1-x}M_xSi$ (M= Ir, Os)".
Physical Review B **91**, 094307 (2015).
DOI: 10.1103/PhysRevB.91.094307.

[Dep10] D. Depla, S. Mahieu, and J. E. Greene. "Chapter 5 - Sputter Deposition Processes".
Handbook of Deposition Technologies for Films and Coatings (Third Edition). Edited by Peter M. Martin. Third Edition. Boston: William Andrew Publishing, 2010, pages 253–296.
DOI: https://doi.org/10.1016/B978-0-8155-2031-3.00005-3.

[Eli73] Z. Eliezer, B. Z. Weiss, M. Ron, and S. Nadiv. "Physical properties of Fe–Ni–Sn Invar alloys-Mössbauer effect study".
Journal of Applied Physics **44**, 419–423 (1973).
DOI: 10.1063/1.1661898.

[Fåk97] B. Fåk and B. Dorner. "Phonon line shapes and excitation energies". *Physica B: Condensed Matter* **234**, 1107–1108 (1997). DOI: 10.1016/S0921-4526(97)00121-X.

[Fre65] A. J. Freeman and R. E. Watson. "Magnetism - Vol. IIA". Edited by G. T. Rado and H. Suhl. Academic Press, New York, 1965. Chapter Hyperfine interactions in magnetic materials.

[Ful10] B. Fultz. "Vibrational thermodynamics of materials". *Progress in Materials Science* **55**, 247–352 (2010). DOI: 10.1016/j.pmatsci.2009.05.002.

[Gor94] E. A. Gorlich, R. Kmiec, K. Latka, A. Szytula, and A. Zygmunt. "Magnetic properties and ^{119}Sn hyperfine interactions investigated in RCoSn (R= Tb, Dy, Ho, Er) compounds". *Journal of Physics: Condensed Matter* **6**, 11127 (1994). DOI: 10.1088/0953-8984/6/50/020.

[Gro78] J. M. Grow, D. G. Howard, R. H. Nussbaum, and M. Takeo. "Frequency moments of cubic metals and substitutional impurities: A critical review of impurity-host force-constant changes from Mössbauer data". *Physical Review B* **17**, 15 (1978). DOI: 10.1103/PhysRevB.17.15.

[Gro82] M. Gross and S. Haroche. "Superradiance: An essay on the theory of collective spontaneous emission". *Physics Reports* **93**, 301–396 (1982). DOI: 10.1016/0370-1573(82)90102-8.

[Hab16] J. Haber, K. S. Schulze, K. Schlage, R. Loetzsch, L. Bocklage, T. Gurieva, H. Bernhardt, H.-C. Wille, R. Rüffer, I. Uschmann, G. G. Paulus, and R. Röhlsberger. "Collective strong coupling of X-rays and nuclei in a nuclear optical lattice". *Nature Photonics* **10**, 445–449 (2016). DOI: 10.1038/NPHOTON.2016.77.

[Hab17] J. Haber, X. Kong, C. Strohm, S. Willing, J. Gollwitzer, L. Bocklage, R. Rüffer, A. Pálffy, and R. Röhlsberger. "Rabi oscillations of x-ray radiation between two nuclear ensembles".
Nature Photonics **11**, 720–725 (2017).
DOI: 10.1038/s41566-017-0013-3.

[Häg75] L. Häggström, T. Ericsson, R. Wäppling, and K. Chandra. "Studies of the magnetic structure of FeSn using the Mössbauer effect".
Physica Scripta **11**, 47 (1975).
DOI: 10.1088/0031-8949/11/1/008.

[Han89] J. P. Hannon and G. T. Trammell. "Coherent excitations of nuclei in crystals by synchrotron radiation pulses".
Physica B: Condensed Matter **159**, 161–167 (1989).
DOI: 10.1016/0921-4526(89)90034-3.

[Hee13] K. P. Heeg and J. Evers. "X-ray quantum optics with Mössbauer nuclei embedded in thin-film cavities".
Physical Review A **88**, 043828 (2013).
DOI: 10.1103/PhysRevA.88.043828.

[Hee15] K. P. Heeg, J. Haber, D. Schumacher, L. Bocklage, H.-C. Wille, K. S. Schulze, R. Loetzsch, I. Uschmann, G. G. Paulus, R. Rüffer, R. Röhlsberger, and J. Evers. "Tunable subluminal propagation of narrow-band X-ray pulses".
Physical Review Letters **114**, 203601 (2015).
DOI: 10.1103/PhysRevLett.114.203601.

[Hou17] K. Houben, S. Couet, M. Trekels, E. Menéndez, T. Peissker, J. W. Seo, M. Y. Hu, J. Y. Zhao, E. E. Alp, S. Roelants, B. Partoens, M. V. Milošević, F. M. Peeters, D. Bessas, S. A. Brown, A. Vantomme, K. Temst, and M. J. Van Bael. "Lattice dynamics in Sn nanoislands and cluster-assembled films".
Physical Review B **95**, 155413 (2017).
DOI: 10.1103/PhysRevB.95.155413.

[Hou20] K. Houben, J. K. Jochum, S. Couet, E. Menéndez, T. Picot, M. Y. Hu, J. Y. Zhao, E. E. Alp, A. Vantomme, K. Temst, and M. J. Van Bael. "The influence of phonon softening on the superconducting critical temperature of

Sn nanostructures".
Scientific Reports **10**, 1–9 (2020).
DOI: 10.1038/s41598-020-62617-4.

[Hua16] T.-T. Huang, S.-W. Lin, C.-M. Chen, P. Y. Chen, and Y.-W. Yen. "Phase equilibria of the Fe-Ni-Sn ternary system at 270°C".
Journal of Electronic Materials **45**, 6208–6213 (2016).
DOI: 10.1007/s11664-016-4787-8.

[Huf70] G. P. Huffman and G. R. Dunmyre. "Anomalous temperature dependence of the hyperfine field at ^{119}Sn nuclei in Co and Co–Ni alloys".
Journal of Applied Physics **41**, 1323–1324 (1970).
DOI: 10.1063/1.1658923.

[ICS] ICSD. *Inorganic crystal structure database*. https://icsd.fiz-karlsruhe.de.

[Isi96] J. Isidorsson and C. G. Granqvist. "Electrochromism of Li-intercalated Sn oxide films made by sputtering".
Solar Energy Materials and Solar Cells **44**, 375–381 (1996).
DOI: 10.1016/S0927-0248(95)00178-6.

[Isi98] J. Isidorsson, C. G. Granqvist, K. von Rottkay, and M. Rubin. "Ellipsometry on sputter-deposited tin oxide films: Optical constants versus stoichiometry, hydrogen content, and amount of electrochemically intercalated lithium".
Applied Optics **37**, 7334–7341 (1998).
DOI: 10.1364/AO.37.007334.

[Keu18] W. Keune, S. Hong, M. Y. Hu, J. Zhao, T. S. Toellner, E. E. Alp, W. Sturhahn, T. S. Rahman, and B. R. Cuenya. "Influence of interfaces on the phonon density of states of nanoscale metallic multilayers: Phonon confinement and localization".
Physical Review B **98**, 024308 (2018).
DOI: 10.1103/PhysRevB.98.024308.

[Krü07] B. Krüger, A. Drews, M. Bolte, U. Merkt, D. Pfannkuche, and G. Meier. "Harmonic oscillator model for current-and field-driven magnetic vortices".

Physical Review B **76**, 224426 (2007).
DOI: 10.1103/PhysRevB.76.224426.

[Kuk15] R. Kukreja, S. Bonetti, Z. Chen, D. Backes, Y. Acremann, J. A. Katine, A. D. Kent, H. A. Dürr, H. Ohldag, and J. Stöhr. "X-ray detection of transient magnetic moments induced by a spin current in Cu".
Physical Review Letters **115**, 096601 (2015).
DOI: 10.1103/PhysRevLett.115.096601.

[Kum96] K. C. H. Kumar, P. Wollants, and L. Delaey. "Thermodynamic evaluation of Fe-Sn phase diagram".
Calphad **20**, 139–149 (1996).
DOI: 10.1016/S0364-5916(96)00021-1.

[Kus19] E. Kusano. "Structure-zone modeling of sputter-deposited thin films: A brief review".
Applied Science and Convergence Technology **28**, 179–185 (2019).
DOI: 10.5757/ASCT.2019.28.6.179.

[Lak13] G. B. Lak, E. Kuzmann, M. El-Sharif, C. U. Chisholm, S. Stichleutner, Z. Homonnay, and L. Sziráki. "Galvanostatic charge–discharge tests, ^{57}Fe and ^{119}Sn Mössbauer and XRD measurements on novel Sn-Ni-Fe electrodeposits".
Hyperfine Interactions **218**, 145–150 (2013).
DOI: 10.1007/s10751-012-0693-5.

[Lan78] J. I. Langford and A. J. C. Wilson. "Scherrer after sixty years: A survey and some new results in the determination of crystallite size".
Journal of Applied Crystallography **11**, 102–113 (1978).
DOI: 10.1107/S0021889878012844.

[Len20] D. Lentrodt, K. P. Heeg, C. H. Keitel, and J. Evers. "Ab initio quantum models for thin-film x-ray cavity QED".
Physical Review Research **2**, 023396 (2020).
DOI: 10.1103/PhysRevResearch.2.023396.

[Lid06] D. R. Lide, editor. *CRC Handbook of Chemistry and Physics, 87th Edition.* 87th edition. CRC Press/Taylor & Francis, 2006.

[Lip60] H. J. Lipkin. "Some simple features of the Mössbauer effect".
Annals of Physics **9**, 332–339 (1960).
DOI: 10.1016/0003-4916(60)90035-X.

[Lip95] H. J. Lipkin. "Mössbauer sum rules for use with synchrotron sources".
Physical Review B **52**, 10073 (1995).
DOI: 10.1103/PhysRevB.52.10073.

[Liu03] H. S. Liu, C. L. Liu, K. Ishida, and Z. P. Jin. "Thermodynamic modeling of the Au-In-Sn system".
Journal of Electronic Materials **32**, 1290–1296 (2003).
DOI: 10.1007/s11664-003-0025-2.

[Liu20] M. Liu, C. Liu, U. P. Kumar, and M. Chen. "Exploring configurations and properties of boron carbide by first principle".
Materials Research Express **7**, 015904 (2020).
DOI: 10.1088/2053-1591/ab6118.

[LJ39] W. E. Lamb Jr. "Capture of neutrons by atoms in a crystal".
Physical Review **55**, 190 (1939).
DOI: 10.1103/PhysRev.55.190.

[Luc08] M. S. Lucas, M. Kresch, R. Stevens, and B. Fultz. "Phonon partial densities of states and entropies of Fe and Cr in bcc Fe-Cr from inelastic neutron scattering".
Physical Review B **77**, 184303 (2008).
DOI: 10.1103/PhysRevB.77.184303.

[Luc13] M. S. Lucas, L. Mauger, J. A. Munoz, I. Halevy, J. Horwath, S. L. Semiatin, S. O. Leontsev, M. B. Stone, D. L. Abernathy, Y. Xiao, P. Chow, and B. Fultz. "Phonon densities of states of face-centered-cubic Ni-Fe alloys".
Journal of Applied Physics **113**, 17A308 (2013).
DOI: 10.1063/1.4794354.

[Mal13] M. Maldovan. "Sound and heat revolutions in phononics".
Nature **503**, 209–217 (2013).
DOI: 10.1038/nature12608.

[Man14] P. K. Manna and S. M. Yusuf. "Two interface effects: Exchange bias and magnetic proximity".
Physics Reports **535**, 61–99 (2014).
DOI: 10.1016/j.physrep.2013.10.002.

[Man68] P. D. Mannheim. "Influence of force-constant changes on the lattice dynamics of cubic crystals with point defects".
Physical Review **165**, 1011 (1968).
DOI: 10.1103/PhysRev.165.1011.

[Man71] P. D. Mannheim and S. S. Cohen. "Force-constant changes and the crystal impurity problem".
Physical Review B **4**, 3748 (1971).
DOI: 10.1103/PhysRevB.4.3748.

[Man72] P. D. Mannheim. "Localized modes and cell-model limit in the crystal impurity problem".
Physical Review B **5**, 745 (1972).
DOI: 10.1103/PhysRevB.5.745.

[Mar17] C. Marker, S.-L. Shang, X. L. Liu, G. Lindwall, and Z.-K. Liu. "First-principles calculations and thermodynamic modeling of the Sn-Ta system".
Calphad **57**, 46–54 (2017).
DOI: 10.1016/j.calphad.2017.03.001.

[Mat62] E. Matthias, W. Schneider, and R. M. Steffen. "Nuclear level splitting caused by a combined electric quadrupole and magnetic dipole interaction".
Physical Review **125**, 261 (1962).
DOI: 10.1103/PhysRev.125.261.

[MED] MEDC. *Mössbauer Effect Data Center*. https://medc.dicp.ac.cn/Resources-isotopes/Resource-Sn.php.

[Mil98] R. Mildenberger, A. Venskutonis, F. Aubertin, J. Breme, and G. Schwitzgebel. "Electrochemically deposited Ni-Sn alloys: A ^{119}Sn Mössbauer study".
Hyperfine Interactions **112**, 151–154 (1998).
DOI: 10.1023/A:1011065400749.

[Mom11] K. Momma and F. Izumi. "VESTA 3 for three-dimensional visualization of crystal, volumetric and morphology data".
Journal of Applied Crystallography **44**, 1272–1276 (2011).
DOI: 10.1107/S0021889811038970.

[Mos10] O. Mosendz, V. Vlaminck, J. E. Pearson, F. Y. Fradin, G. E. W. Bauer, S. D. Bader, and A. Hoffmann. "Detection and quantification of inverse spin Hall effect from spin pumping in permalloy/normal metal bilayers".
Physical Review B **82**, 214403 (2010).
DOI: 10.1103/PhysRevB.82.214403.

[Mös58] R. L. Mössbauer. "Kernresonanzfluoreszenz von Gammastrahlung in Ir^{191}".
Zeitschrift für Physik **151**, 124–143 (1958).
DOI: 10.1007/BF01344210.

[Na10] S.-H. Na and C.-H. Park. "First-principles study of structural phase transition of Sn".
Journal of the Korean Physical Society **56**, 494–497 (2010).
DOI: 10.3938/jkps.56.494.

[Nai06] S. Naille, P. E. Lippens, F. Morato, and J. Olivier-Fourcade. "^{119}Sn Mössbauer study of nickel–tin anodes for rechargeable lithium-ion batteries".
Hyperfine Interactions **167**, 785–790 (2006).
DOI: 10.1007/s10751-006-9357-7.

[Nak15] S. Nakamura and A. Fuwa. "Spin order in $FeCr_2O_4$ observed by Mössbauer spectroscopy".
Physics Procedia **75**, 747–754 (2015).
DOI: 10.1016/j.phpro.2015.12.097.

[Nas85] P. Nash and A. Nash. "The Ni- Sn (nickel-tin) system".
Bulletin of Alloy Phase Diagrams **6**, 350–359 (1985).
DOI: 10.1007/BF02880521.

[NDS] NDS. *Nuclear Data Service*. https://www-nds.iaea.org/.

[O'B03] J. W. O'Brien, R. A. Dunlap, and J. R. Dahn. "A Mössbauer effect and X-ray diffraction investigation of Ti–Sn intermetallic compounds:: II. Nanostructured phases prepared by ball milling with Al_2O_3 and TiN".
Journal of Alloys and Compounds **353**, 65–73 (2003).
DOI: 10.1016/S0925-8388(02)01305-1.

[Oka10] H. Okamoto. "Sn-Ti (tin-titanium)".
Journal of Phase Equilibria and Diffusion **31**, 202–203 (2010).
DOI: 10.1007/s11669-010-9663-2.

[Osa87] F. A. N. Osadebe and A. E. Arua. "The Mossbauer effect and electron configuration for tin metal".
Journal of Physics C: Solid State Physics **20**, 1359 (1987).
DOI: 10.1088/0022-3719/20/9/025.

[Par12] P. P. Parshin, M. G. Zemlyanov, G. K. Panova, A. A. Shikov, Y. A. Kumzerov, A. A. Naberezhnov, I. Sergueev, W. Crichton, A. I. Chumakov, and R. Rüffer. "Atomic dynamics of tin nanoparticles embedded into porous glass".
Journal of Experimental and Theoretical Physics **114**, 440–450 (2012).
DOI: 10.1134/S1063776112010141.

[Par54] L. G. Parratt. "Surface studies of solids by total reflection of X-rays".
Physical Review **95**, 359 (1954).
DOI: 10.1103/PhysRev.95.359.

[PHO] PHOENIX. *Version 3.0.0 by W. Sturhahn.* http://www.nrixs.com.

[PJ08] E. Partyka-Jankowska, B. Sepiol, M. Sladecek, D. Kmiec, J. Korecki, T. Slezak, M. Zajac, S. Stankov, R. Rüffer, and G. Vogl. "Nuclear resonant scattering studies of electric field gradient in Fe monolayer on W(1 1 0)".
Surface Science **602**, 1453–1457 (2008).
DOI: 10.1016/j.susc.2008.02.007.

[Poa81] J. M. Poate. "Diffusion and reactions in gold films".
Gold Bulletin **14**, 2–11 (1981).
DOI: 10.1007/BF03216552.

[Por65] A. M. Portis and R. H. Lindquist. "Magnetism - Vol. IIA". Edited by G. T. Rado and H. Suhl. Academic Press, New York, 1965. Chapter Nuclear resonances in ferromagnetic materials, pages 363 –376.

[Rö04] R. Röhlsberger. *Nuclear condensed matter physics with synchrotron radiation.* Springer Tracts in Modern Physics, Vol. 208. Springer-Verlag Berlin Heidelberg, 2004.
DOI: 10.1007/b86125.

[Röh02] R. Röhlsberger, H. Thomas, K. Schlage, E. Burkel, O. Leupold, and R. Rüffer. "Imaging the magnetic spin structure of exchange-coupled thin films".
Physical Review Letters **89**, 237201 (2002).
DOI: 10.1103/PhysRevLett.89.237201.

[Röh10] R. Röhlsberger, K. Schlage, B. Sahoo, S. Couet, and R. Rüffer. "Collective Lamb shift in single-photon superradiance".
Science **328**, 1248–1251 (2010).
DOI: 10.1126/science.1187770.

[Röh12] R. Röhlsberger, H.-C. Wille, K. Schlage, and B. Sahoo. "Electromagnetically induced transparency with resonant nuclei in a cavity".
Nature **482**, 199–203 (2012).
DOI: 10.1038/nature10741.

[Röh20] R. Röhlsberger, J. Evers, and S. Shwartz. *Quantum and nonlinear optics with hard x-rays.* Edited by E. Jaeschke, S. Khan, J. R. Schneider, and J. B. Hastings. Springer, 2020, pages 1399–1431.

[Röh99] R. Röhlsberger, W. Sturhahn, T. S. Toellner, K. W. Quast, P. Hession, M. Hu, J. Sutter, and E. E. Alp. "Phonon damping in thin films of Fe".
Journal of Applied Physics **86**, 584–587 (1999).
DOI: 10.1063/1.370770.

[Rud04] S. P. Rudin, M. D. Jones, and R. C. Albers. "Thermal stabilization of the hcp phase in titanium".
Physical Review B **69**, 094117 (2004).
DOI: 10.1103/PhysRevB.69.094117.

[Sah11] B. Sahoo, K. Schlage, J. Major, U. Von Hörsten, W. Keune, H. Wende, and R. Röhlsberger. "Preparation and characterization of ultrathin stainless steel films".
AIP Conference Proceedings. **1347**. 1. American Institute of Physics. 2011, pages 57–60.
DOI: 10.1063/1.3601785.

[Sch81] H. R. Schober and P. H. Dederichs. *Phonon states of elements. Electron states and fermi surfaces of alloys/Phononenzustände von Elementen. Elektronenzustände und Fermiflächen von Legierungen*. Edited by K. H. Hellwege and J. L. Olsen. Landolt Börnstein, New Series, III/13a. Springer, 1981.

[Set00] M. Seto, Y. Kobayashi, S. Kitao, R. Haruki, T. Mitsui, Y. Yoda, S. Nasu, and S. Kikuta. "Local vibrational densities of states of dilute Fe atoms in Al and Cu metals".
Physical Review B **61**, 11420 (2000).
DOI: 10.1103/PhysRevB.61.11420.

[Sha64] V. G. Shapiro and V. S. Shpinel. "Anisotropy of the Mossbauer effect in single crystal of β-Sn and cassiterite (SnO_2)".
Soviet Physics JETP-USSR **19**, 1321–1323 (1964).

[Shi00] J. Shi, D. Kojima, and M. Hashimoto. "The interaction between platinum films and silicon substrates: Effects of substrate bias during sputtering deposition".
Journal of Applied Physics **88**, 1679–1683 (2000).
DOI: 10.1063/1.373871.

[Sin60] K. S. Singwi and A. Sjölander. "Resonance absorption of nuclear gamma rays and the dynamics of atomic motions".
Physical Review **120**, 1093 (1960).
DOI: 10.1103/PhysRev.120.1093.

[Sin84] P. Singh and M. Ohring. "Tracer study of diffusion and electromigration in thin tin films".
Journal of Applied Physics **56**, 899–907 (1984).
DOI: 10.1063/1.334065.

[Smi09] D.-M. Smilgies. "Scherrer grain-size analysis adapted to grazing-incidence scattering with area detectors".
Journal of Applied Crystallography **42**, 1030–1034 (2009).
DOI: 10.1107/S0021889809040126.

[Smi99] G. V. Smirnov. "General properties of nuclear resonant scattering".
Hyperfine Interactions **123**, 31–77 (1999).
DOI: 10.1023/A:1017007520099.

[Soa73] J. C. Soares, K. Krien, A. G. Bibiloni, K. Freitag, and R. Vianden. "Determination of the quadrupole splitting of the first excited state of ^{119}Sn in β-tin by the e–γ TDPAC technique".
Physics Letters A **45**, 465–466 (1973).
DOI: 10.1016/0375-9601(73)90710-X.

[Sta07] S. Stankov, R. Röhlsberger, T. Ślęzak, M. Sladecek, B. Sepiol, G. Vogl, A. I. Chumakov, R. Rüffer, N. Spiridis, J. Łażewski, K. Parliński, and J. Korecki. "Phonons in iron: From the bulk to an epitaxial monolayer".
Physical Review Letters **99**, 185501 (2007).
DOI: 10.1103/PhysRevLett.99.185501.

[Stu99a] W. Sturhahn and A. Chumakov. "Lamb–Mössbauer factor and second-order Doppler shift from inelastic nuclear resonant absorption".
Hyperfine Interactions **123**, 809–824 (1999).
DOI: 10.1023/A:1017052730094.

[Stu99b] W. Sturhahn and V. G. Kohn. "Theoretical aspects of incoherent nuclear resonant scattering".
Hyperfine Interactions **123**, 367–399 (1999).
DOI: 10.1023/A:1017071806895.

[Sut96] A. P. Sutton and R. W. Balluffi. *Interfaces in crystalline materials*. Clarendon Press, Oxford, 1996.

[Sva97] A. Svane, N. E. Christensen, C. O. Rodriguez, and M. Methfessel. "Calculations of hyperfine parameters in tin compounds".
Physical Review B **55**, 12572 (1997).
DOI: 10.1103/PhysRevB.55.12572.

[Swa84] L. J. Swartzendruber. “The Ag- Fe (silver-iron) system”.
Bulletin of Alloy Phase Diagrams **5**, 560–564 (1984).
DOI: 10.1007/BF02868316.

[Szi10] L. Sziráki, E. Kuzmann, M. El-Sharif, C. U. Chisholm, S. Stichleutner, G. B. Lak, K. Süvegh, E. Tatár, Z. Homonnay, and A. Vértes. “Electrodeposition of novel Sn–Ni–Fe ternary alloys with amorphous structure”.
Applied Surface Science **256**, 7713–7716 (2010).
DOI: 10.1016/j.apsusc.2010.06.026.

[Szi12] L. Sziráki, E. Kuzmann, G. B. Lak, M. El-Sharif, C. U. Chisholm, S. Stichleutner, K. Havancsák, K. Zih-Perényi, Z. Homonnay, and A. Vértes. “Study of electrodeposition of amorphous Sn–Ni–Fe ternary alloys from a gluconate based electrolyte”.
Surface and Coatings Technology **211**, 184–187 (2012).
DOI: 10.1016/j.surfcoat.2011.09.024.

[The54] J. Thewlis and A. R. Davey. “Thermal expansion of grey tin”.
Nature **174**, 1011–1011 (1954).
DOI: 10.1038/1741011a0.

[Tho74] J. A. Thornton. “Influence of apparatus geometry and deposition conditions on the structure and topography of thick sputtered coatings”.
Journal of Vacuum Science and Technology **11**, 666–670 (1974).
DOI: 10.1116/1.1312732.

[Tro16] I. Troyan, A. Gavriliuk, Rudolf Rüffer, A. I. Chumakov, A. Mironovich, I. Lyubutin, D. Perekalin, A. P. Drozdov, and M. I. Eremets. “Observation of superconductivity in hydrogen sulfide from nuclear resonant scattering”.
Science **351**, 1303–1306 (2016).
DOI: 10.1126/science.aac8176.

[VH53] L. Van Hove. “The occurrence of singularities in the elastic frequency distribution of a crystal”.
Physical Review **89**, 1189 (1953).
DOI: 10.1103/PhysRev.89.1189.

[Wer64] G. K. Wertheim. *Mössbauer effect: Principles and applications*. Academic Press, New York and London, 1964.

[Woł81] M. Wołcyrz, R. Kubiak, and S. Maciejewski. "X-ray investigation of thermal expansion and atomic thermal vibrations of tin, indium, and their alloys". *Physica Status Solidi (B)* **107**, 245–253 (1981).
DOI: https://doi.org/10.1002/pssb.2221070125.

[Yin06] L. F. Yin, D. H. Wei, N. Lei, L. H. Zhou, C. S. Tian, G. S. Dong, X. F. Jin, L. P. Guo, Q. J. Jia, and R. Q. Wu. "Magnetocrystalline anisotropy in permalloy revisited". *Physical Review Letters* **97**, 067203 (2006).
DOI: 10.1103/PhysRevLett.97.067203.

Danksagung

An dieser Stelle möchte ich mich herzlich bedanken bei den vielen Leuten, die mich während meiner Doktorarbeit unterstützt haben. Ganz besonders möchte ich mich dabei bedanken bei ...

... Prof. Dr. Ralf Röhlsberger für eine hervorragende Betreuung meiner Doktorarbeit, die konstante und motivierende Unterstützung in jeglichen Bereichen und darüberhinaus für die Übernahme des Erstgutachtens

... Prof. Dr. Rübhausen für die Übernahme des Zweitgutachten

... Dr. Lars Bocklage für die hervorragende Betreuung, das Korrekturlesen meiner Arbeit, die unermüdliche Unterstützung bei Strahlzeiten, Probenpräparationen uvm., die Bereitschaft jederzeit für Fragen zur Verfügung zu stehen und somit ein sehr angenehmes Arbeitsklima zu schaffen

... Dr. Kai Schlage für seine Hilfsbereitschaft bei Strahlzeiten und Probenpräparationen und für viele anregende und hilfreiche Diskussionen rund um meine Arbeit, sowie ein sehr angenehmes Arbeitsklima im Büro

... PD Dr. Guido Meier für zahlreiche anregende Gespräche und bei jeder Frage zur Verfügung zu stehen, sowie für die Teilnahme an der Prüfungskommission

... Dr. Hans-Christian Wille für die hervorragenden Unterstützung bei Strahlzeiten und die Teilnahme an der Prüfungskommission

... Prof. Dr. Potthoff für die Übernahme des Vorsitz der Prüfungskommission

... Andrey Siemens für die Bereitschaft bei jeglichen technischen Problemen mit Rat und Tat beiseitezustehen

... Dr. Ilya Sergeev für die Bereitstellung seiner Software *nisdos* und seiner Unterstützung bei der Auswertung der unelastischen Daten, sowie für seinen Einsatz bei Strahlzeiten bei P01

... Dem gesamten Team von P01, insbesondere Dr. Olaf Leupold, Dr. Réne Steinbrügge und Frank-Uwe Dill für die Unterstützung bei Strahlzeiten und vielen interessanten Diskussionen

... Michael Hu and Esen E. Alp for their support and for performing the experiments at 30-ID at the APS during the Corona pandemic where only remote beamtime was possible

... Dr. R. Reddy and his students in Indore, India for performing CEMS measurements

... Dr. Dieter Lott für die Unterstützung am RöDi

... PD Dr. Jörg Evers, Dr. Kilian P. Heeg und Dominik Lentrodt für die Hilfe bei der Strahlzeit, die Bereitstellung ihres 2D Messsystems und des Softwarepakets *pynuss*, sowie für viele interessante Diskussionen über Kernquantenoptik

... Dr. Svenja Willing und Dr. Jakob Gollwitzer für die Unterstützung bei Strahlzeiten und Probenpräparation und ein sehr angenehmes Arbeitsklima

... Dr. Elena König für die Unterstützung bei Lithographie und AFM Messungen

... Bei allen aktiven und ehemaligen Mitgliedern der Gruppe FS-MCP für ein motivierendes und konstruktives Arbeitsklimas in der Gruppe, darunter Dr. Tatiana Gurieva, Dr. Mehdi Ramin Moayed, Dr. Cornelius Strohm, Dr. Anjali Panchwanee, Ankita Negi, Leon Merten Lohse und Dr. Christian F. Adolff

... Meiner Familie, dabei besonders meinen Eltern und meinem Bruder für den Rückhalt und Unterstützung während meines Studiums

... Dr. Donatella Loru for her support and for being a constant source of motivation throughout my work

Eidesstattliche Versicherung

Hiermit versichere ich an Eides statt, die vorliegende Dissertationsschrift selbst verfasst und keine anderen als die angegebenen Hilfsmittel und Quellen benutzt zu haben.

Hamburg, den 04.10.2021

Sven Velten